Author:
Budyn, Nicolas S

Title:
Imaging and defect characterisation using multi-view ultrasonic data in nondestructive evaluation

Imaging and defect characterisation using multi-view ultrasonic data in nondestructive evaluation

Nicolas Budyn

Department of Mechanical Engineering,
University of Bristol

A dissertation submitted to the University of Bristol in accordance with the requirements of the degree of Engineering Doctorate in the Faculty of Engineering.

August 2020

Word count: 27 681

Abstract

Ultrasonic arrays are used in nondestructive testing for a wide range of inspections. The Full Matrix Capture (FMC) acquisition technique allows the capture of all the information possibly measurable by the probe. The Total Focusing Method (TFM) forms images by post-processing the FMC data, superseding conventional phased array techniques. By exploiting the wave mode conversions and the internal wave reflections in the specimen, multiple ultrasonic images may be formed, an approach termed multi-view imaging. Multi-view imaging increases the chance of obtaining a high response from a hypothetical defect in the specimen by considering multiple insonification paths.

This thesis investigates several areas relevant to multi-view imaging and defect characterisation. The defect response varies greatly with several variables including its shape, location, orientation, and the inspection set-up. As a consequence, the defect may have a strong response in a view, but be invisible in another one. A fast ultrasonic model which predicts the defect response in any view is introduced to help design sensitive inspections. The model is also used to build a database of reference scatterers against which the unknown defect is compared to characterise it. This technique makes it possible to determine the approximate shape, size and orientation of flaws which are too small to be well resolved on a TFM image.

The structural noise ultimately limits the detectability in ultrasonic images by creating a speckle pattern obscuring the defect. The peak amplitude of the speckle is a quantity relevant to the calculation of probabilities of detection and false alarm, but has been little studied in the literature. This thesis pursues its analysis.

Delay-and-sum is a widespread imaging approach. The presence of wall reflections may significantly degrade the image by adding artefacts. Replacing the summation by the median, a novel approach, is shown to efficiently suppress these artefacts.

Author's declaration

I declare that the work in this dissertation was carried out in accordance with the requirements of the University's *Regulations and Code of Practice for Research Degree Programmes* and that it has not been submitted for any other academic award. Except where indicated by specific reference in the text, the work is the candidate's own work. Work done in collaboration with, or with the assistance of, others, is indicated as such. Any views expressed in the dissertation are those of the author.

SIGNED: ..... DATE: .....

Acknowledgements

I wish to express my gratitude to the funders of this research project: the UK Research Centre in Nondestructive Evaluation (RCNDE), its own sponsors the Engineering and Physical Sciences Research Council (EPSRC) and ultimately the UK taxpayer, and BAE Systems.

I thank my academic supervisors Prof Paul Wilcox and Prof Anthony Croxford for their support throughout this research project. It was a privilege to work under their guidance.

I thank my industrial supervisors Dr Tom Barber and Mr Andrew Nixon for their support and the interesting discussions we had regarding the practice of nondestructive testing in the real world.

I thank Prof Bruce Drinkwater, Dr Peter Huthwaite and Dr Casper Wassink for having accepted to be the examiners of this thesis, and for their helpful comments and suggestions during the viva.

I thank Dr Jie Zhang, Dr Rhodri Bevan, Dr Artem Kashubin and Dr Alexander Velichko for our fruitful exchanges, and for sharing with me very useful ultrasonic data and code.

I would like to pay my special regards to Mr Frédéric Massias, whose excellent physics courses in lycée Saint-Louis pushed me towards nondestructive testing, and to Mr Nechtan Le Lostec, from whom I learned so much during my master's degree.

I am grateful to the past and present members of the Ultrasonics and Nondestructive Testing Group for contributing to create such a pleasant and stimulating workplace.

Finally, I thank my family and friends for their encouragement.

À mes parents

Contents

Chapter 1

Introduction

This thesis is concerned with the use of multi-view ultrasonic data for advanced imaging and defect characterisation. This introductory chapter describes the context and the industrial motivation of this work.

1.1 Context

Nondestructive evaluation (NDE), or nondestructive testing (NDT), is a field concerned with the evaluation of the integrity of an engineering component without damaging it. NDT is used at the time of manufacture and during service to detect, characterise and monitor defects. Ultrasonic testing (UT) is a class of NDT techniques based on the use of ultrasonic waves, i.e. high-frequency elastic waves. A basic UT technique is the pulse-echo technique [Kra90]: the transducer insonifies the inspected object with a pulsed ultrasonic wave (transmission), and receives the reflected/scattered signal (reception). The received signal is displayed as a time-amplitude graph called a timetrace or an A-scan. The quantities of interest are the amplitudes of the echoes and their times of flight, which correspond to the geometric features of the object and possible defects. The main drawback is the difficulty to interpret reliably the timetrace, a task which requires extensive training. Forming an ultrasonic image eases the interpretation. A simple technique is to stack timetraces obtained by scanning the inspected object along a line on its surface in an image with time-distance axes, which is called a B-scan. Due to the finite width of the beam, a scatterer is insonified at multiple consecutive transducer positions, which leads to a low lateral resolution. A much higher resolution can

be achieved using synthetic aperture techniques, which originate from the radar community in the 1950s and emerged in ultrasonic testing in the 1970s [Doc86; Jen06]. The canonical technique, the Synthetic Aperture Focusing Technique (SAFT), emulates to a certain extent a large-aperture transducer from a single moving small-aperture transducer, or a collection of fixed small-aperture transducers. Under this approach, the individual timetraces are delayed with appropriate focal laws and combined so that the ultrasonic beam is synthetically focused on any given point. The focusing is done as a post-processing step rather than physically in the object. The computational cost was a significant issue at the time these techniques were initially developed, but this is no longer the case with modern equipment.

A second important development in ultrasonic testing is the emergence of ultrasonic arrays [Dri06; Oly17]. An ultrasonic array is a transducer that contains several individual transducers (elements) which independently transmit and receive. A first application is the electronic B-scan, which emulates a manual scan over the length of the array by pulsing each element sequentially. But the main advantage compared to a monolithic transducer is the ability to electronically control the ultrasonic beam by pulsing the elements with appropriate delay laws, known as beamforming, which is the core of phased-array ultrasonic testing (PAUT). For example, an image can be produced by sweeping electronically the beam over a range of angles, a technique called sector- or S-scan and notably used for the inspection of welds; it was initially developed in the medical field to advantageously replace a mechanical scan where the operator had to manually vary the probe orientation to change the beam direction [Som68]. PAUT has been around since the early 2000s and is now a mature and widely-used technology with applications in multiple industries including power generation, defence, rail transport, aerospace, oil and gas. ISO [ISO19], ASTM [AST14], and ASME [ASM19] codes and standards establish specifications and procedures for PAUT inspections.

In the last two decades, the increase of computational power and memory has paved the way to novel ultrasonic array imaging techniques, based on new acquisition techniques such as the Full Matrix Capture (FMC), which consists in recording the timetraces corresponding to each pair of probe elements. The size of a FMC dataset is typically one to two orders of magnitude larger than in a conventional S-scan, as significantly more information is acquired. The FMC is the enabler for a host of advanced imaging techniques. One of them, the Total Focus Method (TFM) [Hol05], which is a synthetic aperture algorithm which focuses on every

point of the image with the whole ultrasonic array, stands out as the most mature and is being adopted by industries as demonstrated by the ongoing development of ISO standards [ISO20b; ISO20a]. By exploiting multiple ultrasonic ray paths in the inspected object, multiple TFM images may be formed [Zha10b]. This approach, termed multi-view TFM, opens new avenues for characterising defects, and is the main subject of this dissertation.

1.2 Industrial motivation

In various engineering fields, and notably within BAE Systems which has sponsored this work, ultrasonic testing and radiographic testing are the two current NDT methods used for determining weld integrity at manufacture. Radiographic testing leads to photographic images, which tend to be easier to interpret than ultrasonic results. However, the radiation hazard creates practical issues. For health and safety reasons, using a radiation source is highly regulated. This has implications for personnel qualifications, and the storage and transportation of the radioactive source. During a radiographic inspection, an exclusion area is set where no personnel is allowed, which prevents other tasks being run in parallel in the vicinity of the inspection, and reduces overall productivity. Ultrasonic inspections do not suffer from such safety issues, and are therefore used to replace radiography testing whenever possible, leading to a reduction of production costs. However, current ultrasonic techniques can fail to meet the desired level of performance for highly scattering and attenuative materials, which drives the development and possible adoption of more advanced techniques.

A specific challenge is the characterisation of defects with ultrasound. If a defect is detected, the primary objective is to assess its severity, depending notably on its size and whether it is volumetric or planar. If it is deemed severe, the component is repaired or replaced. The acceptance criteria are defined conservatively to account for the uncertainties of the defect classification and sizing technique. As a consequence, components with only benign defects are sometimes unnecessarily repaired, which increases the production costs. This could be avoided with more precise, accurate, and reliable defect characterisation techniques, which motivates this work.

The multi-view Total Focusing Method imaging algorithm provides a possible avenue for better defect characterisation in ultrasonic testing, which is explored in this thesis. Under

this approach, multiple images are formed from different ultrasonic ray paths [Zha10b]. The orientation of the defect relative to these rays greatly influences the strength of the response, which makes different views more or less suited for specific defects. For example, the views constructed from one reflection against the back wall, known as half-skip views, have been demonstrated to be well suited for surface breaking cracks [Fel14]. Fusing the views into a single image eases the interpretation [Sy18a; Sy18b]. Defects can be accurately sized from the image, provided that their size is larger than the image resolution (point spread function) [Fel18]. However, characterising smaller defects remains difficult. This thesis proposes a new technique towards this goal by exploiting differences in defect response between multiple views.

1.3 Thesis outline

Chapter 2 provides an introduction to synthetic aperture imaging techniques, and in particular multi-view TFM. To quantify the effect of the defect shape, size and orientation on multi-view TFM images, a semi-analytical forward model is developed in chapter 3. The modelled defect amplitudes provide the base for a novel characterisation technique, described in chapter 4. The structural noise, caused by the interaction of the ultrasonic wave with the material microstructure, manifests in ultrasonic images as speckle with a level which may be comparable or higher than the defect response. As a first step towards accounting for the structural noise in the characterisation model, the statistics of the speckle are discussed in chapter 5. Finally, a novel variant of delay-and-sum imaging to filter some artefacts is introduced in chapter 6.

Chapter 2

Synthetic aperture imaging in ultrasonic testing

The objective of an imaging algorithm is to form an instructive representation of the interior of the inspected object using the ultrasonic data received by the array. The most common approach is synthetic aperture imaging, which exploits the linearity and time-invariance of the system: the signals received by the ultrasonic array are combined with appropriate phase shifts to synthetically focus the wave field at an image point [Dri06]. These techniques are common to fields governed by the wave equation, such as medical ultrasound [Jen07], seismology [Ble00], radar [Che09], and sonar [Hay09]. This chapter provides an introduction to synthetic aperture imaging techniques in ultrasonic testing, and mentions alternative imaging approaches.

Parts of this chapter have been published in references [Bud18; Bud19].

2.1 Ultrasonic system

Under a system analysis approach, the acquisition device, the ultrasonic array and the inspected object may be seen as a system which takes as input the electronic pulse driving the transducers and produces as output the measured ultrasonic signals. Assuming the array and the inspected object are stationary, this system is time-invariant. Neglecting any non-linearity in the acquisition electronics and in the interaction of the elastic wave with the inspected object, the system is classically modelled as linear time-invariant (LTI) [Sch16; Wil13]. Under such assumption and using an N-element array, linear system theory dictates there exists a $N \times N$

time-varying matrix $\boldsymbol{K}(t)$ so that [Che98]

$$\boldsymbol{o}(t) = \int_0^t \boldsymbol{K}(t-\tau)\boldsymbol{u}(\tau)\, d\tau, \tag{2.1}$$

where $\boldsymbol{o}(t)$ is the $N \times 1$ vector of signals measured by the system (output), and $\boldsymbol{u}(t)$ is the $N \times 1$ vector of signals driving the transducers (input). An equivalent formulation in the frequency domain is obtained using the Fourier transform of this last equation:

$$\boldsymbol{o}(\omega) = \boldsymbol{K}(\omega)\boldsymbol{u}(\omega). \tag{2.2}$$

$\boldsymbol{K}(t)$ or its frequency-domain pendant $\boldsymbol{K}(\omega)$ are called the transfer matrix of the system. Its entries are the impulse response for a given pair of transmitter and receiver: $K_{ji}(t)$ is the signal received by the j-th element when the i-th element is driven by an impulse (Dirac delta function), whilst no other element transmits. Due to the electromechanical reciprocity of ultrasonic systems [Aul79; Sch15], the transfer matrix is symmetric

$$\boldsymbol{K}^T = \boldsymbol{K} \tag{2.3}$$

The transfer matrix contains all the information possibly measurable by the system under the LTI assumption. Any physical ultrasonic acquisition can therefore be seen as probing the transfer matrix with a given input. Furthermore, knowing the transfer matrix allows the output to be synthetically reconstructed from any arbitrary input using eqs. (2.1) and (2.2), which may be with modern computers faster than a physical acquisition, and opens the way to more advanced imaging techniques. The experimental determination of the transfer matrix is covered in the following section.

2.2 Full Matrix Capture

The Full Matrix Capture (FMC) is an ultrasonic array acquisition technique which consists of pulsing sequentially each element, and recording with all elements (including the transmitter) during each transmission event [Hol05; Wil13]. The result for a N-element array is an $N \times N$ matrix $\boldsymbol{F}(t)$, where each entry $F_{ij}(t)$ is the time signal associated with the i-th transmitter and the j-th receiver. This matrix is generally referred to in the literature as the FMC matrix or FMC data, but is also known as the multistatic response matrix [Amm13] and the full array response matrix [Bor02].

The FMC matrix relates closely to the transfer matrix. Denoting the electronic signal delivered by the pulser as $v(t)$ and $v(\omega)$, assumed to be the same for all array elements, an FMC acquisition corresponds to the following $N \times N$ input matrix, where the i-th column is the input vector corresponding to the i-th transmission sequence:

$$\boldsymbol{U}_{\mathrm{FMC}}(\omega) = \begin{bmatrix} v(\omega) & 0 & \cdots & 0 \\ 0 & v(\omega) & \cdots & 0 \\ \vdots & \vdots & \ddots & \vdots \\ 0 & 0 & \cdots & v(\omega) \end{bmatrix} = \boldsymbol{I}_n v(\omega), \tag{2.4}$$

with $\boldsymbol{I}_n$ denoting the $N \times N$ identity matrix. By definition of the FMC matrix and using eq. (2.2), the result of this acquisition is the $N \times N$ matrix

$$\boldsymbol{F}^T(\omega) \coloneqq \boldsymbol{O}_{\mathrm{FMC}}(\omega) = \boldsymbol{K}(\omega)\boldsymbol{U}_{\mathrm{FMC}}(\omega) = \boldsymbol{K}(\omega)v(\omega). \tag{2.5}$$

Recalling that a frequency-domain multiplication corresponds to a time-domain convolution, the time-domain FMC matrix is therefore the transfer matrix convolved with the electronic pulse v. So the FMC matrix approximates the transfer matrix with a loss of information determined by the pulser. The FMC matrix contains all possibly measurable information under the LTI assumption with a given pulse. If the pulse is short enough to have a flat spectrum over the bandwidth of the ultrasonic system, it is well approximated by the Dirac delta function ($v(\omega) = 1$), so the FMC matrix is the transpose of the transfer matrix. Recalling the transfer matrix is symmetric, the FMC matrix is also symmetric and equal to the transfer matrix:

$$\boldsymbol{F}(t) = \boldsymbol{K}(t), \tag{2.6}$$

$$\boldsymbol{F}(\omega) = \boldsymbol{K}(\omega). \tag{2.7}$$

Under this assumption, used from now on in this thesis, the distinction between the transfer and FMC matrices is purely semantic. Due to the symmetry, recording the diagonal and the lower (or upper) part of the matrix, i.e. F_{ij} for $i \geq j$, is sufficient to reconstruct the full matrix. This acquisition technique is known as the Half Matrix Capture (HMC) [Wil13]. The advantages are a lowered amount of data to record and transfer from the acquisition device to the processing unit.

Several incoherent sources perturb the measurement of the FMC matrix, such as thermal acoustic noise and noise in the electronics. Modelled as additive, this noise can be suppressed

by averaging multiple FMC acquisitions [Wil13]. An alternative and mathematically elegant solution is Hadamard coding [Amm13]. A Hadamard matrix is a square matrix $\boldsymbol{A}$ of size $N \times N$ whose entries are either -1 or $+1$ and so that the product of its transpose by itself is N-times the identity matrix:

$$\boldsymbol{A}\boldsymbol{A}^T = \boldsymbol{A}^T\boldsymbol{A} = N\boldsymbol{I}_n. \tag{2.8}$$

An example of Hadamard matrix for $N = 4$ is

$$\boldsymbol{A} = \begin{bmatrix} 1 & 1 & 1 & 1 \\ 1 & -1 & 1 & -1 \\ 1 & 1 & -1 & -1 \\ 1 & -1 & -1 & 1 \end{bmatrix} \tag{2.9}$$

The Hadamard technique consists in performing the acquisition with the input matrix

$$\boldsymbol{U}_{\text{Had}}(\omega) = \boldsymbol{A}v(\omega). \tag{2.10}$$

Denoting the corresponding output as $\boldsymbol{O}_{\text{Had}}(\omega)$, it follows that

$$\frac{1}{N}\boldsymbol{O}_{\text{Had}}(\omega)\boldsymbol{A}^T = \frac{1}{N}\boldsymbol{K}\boldsymbol{A}_{\text{Had}}\boldsymbol{A}^T v(\omega) = \boldsymbol{K}\boldsymbol{I}_n v(t) = \boldsymbol{O}_{\text{FMC}}(\omega), \tag{2.11}$$

so the FMC matrix can be recovered with a matrix multiplication. The advantage of Hadamard coding is a $\sqrt{N}$-fold increase of the signal to incoherent noise amplitude ratio, which can be demonstrated by including the additive noise term in eq. (2.11) [Amm13] . A similar noise reduction could be achieved by averaging N separate FMC acquisitions, but the Hadamard technique requires only a single acquisition. However, these noise reduction techniques do not affect the coherent noise caused by the interaction of the elastic wave with the material microstructure, which ultimately limits the detectability in an ultrasonic inspection [Wil11].

2.3 Acoustics, elastodynamics and wave equation

The wave equation is the cornerstone of ultrasonic imaging techniques. This section recalls the fundamentals of acoustics and elastodynamics leading to it.

Consider first the case of a fluid at rest and of uniform density, pressure and temperature. The difference between the local pressure and the pressure at rest is the acoustic pressure

denoted $p(\boldsymbol{r}, t)$. By applying Newton's second law on an infinitesimal fluid volume, the pressure field satisfies at first order the well-known wave equation [Mor68, §6.2]

$$\nabla^2 p = \frac{1}{c^2}\frac{\partial^2 p}{\partial t^2}, \tag{2.12}$$

where c is the acoustic wave velocity. The solution for a point source in an infinite medium in 3D is a spherical wave of amplitude proportional to in $1/r$, r being the distance travelled from the source. In 2D, the wave has a changing form and shape in the near field, and becomes cylindrical in the far field with an amplitude decaying in $1/\sqrt{r}$.

The propagation of elastic waves in solids is more complex as solids sustain not only longitudinal but also shear stresses. In the simplest case, the solid is assumed to be at rest, homogeneous with density ρ, linear elastic, and isotropic with Lamé parameters λ and μ. By applying Newton's second law on an infinitesimal volume and using Hooke's law, it follows that the displacement equation of motion is [Ach73]

$$\mu\nabla^2\boldsymbol{u} + (\lambda+\mu)\nabla\nabla\cdot\boldsymbol{u} = \rho\frac{\partial^2\boldsymbol{u}}{\partial t^2}. \tag{2.13}$$

Using Helmholtz's theorem, the displacement field $\boldsymbol{u}(\boldsymbol{r}, t)$ is decomposed into an irrotational component characterised by a scalar potential φ, and a divergence-free component characterised by a vector potential $\boldsymbol{\psi}$

$$\boldsymbol{u} = \nabla\varphi + \nabla\times\boldsymbol{\psi}, \tag{2.14}$$

with

$$\nabla\cdot\boldsymbol{\psi} = 0. \tag{2.15}$$

Substituting eq. (2.14) in eq. (2.13), and after reordering, it comes

$$\nabla\left[(\lambda+2\mu)\nabla^2\varphi - \rho\frac{\partial^2\varphi^2}{\partial t^2},\right] + \nabla\times\left[\mu\nabla^2\boldsymbol{\psi} - \rho\frac{\partial^2\boldsymbol{\psi}}{\partial t^2}\right] = 0. \tag{2.16}$$

For this equation to be valid at all time and everywhere, both terms in square brackets must be null, that is

$$\nabla^2\varphi = \frac{\lambda+2\mu}{\rho}\frac{\partial^2\varphi^2}{\partial t^2} \tag{2.17}$$

$$\nabla^2\boldsymbol{\psi} = \frac{\mu}{\rho}\frac{\partial^2\boldsymbol{\psi}}{\partial t^2}. \tag{2.18}$$

So the displacement potentials satisfy the wave equation, respectively scalar and vectorial. This demonstrates the displacement field may be decoupled into a longitudinal wave of velocity

$c_L = \sqrt{\rho/(\lambda+2\mu)}$, corresponding to the potential φ, and a transverse wave of velocity $c_T = \sqrt{\rho/\mu}$, corresponding to the potential $\boldsymbol{\psi}$. So the longitudinal and transverse waves can be seen as uncoupled acoustic waves, at least regarding their propagation, which simplifies the analysis. They remain however fully coupled at boundaries.

In a Cartesian coordinate system $(\boldsymbol{e}_x, \boldsymbol{e}_y, \boldsymbol{e}_z)$, if the displacement and stress fields are slowly varying in one dimension compared to the two others axes, the problem may be approximated as two-dimensional. This is the case considered in this thesis, where a linear array aligned along $\boldsymbol{e}_x$ is used, with the element dimension along $\boldsymbol{e}_y$ typically 5 times larger than along $\boldsymbol{e}_x$. Neglecting variation along the y-axis (i.e. $\partial/\partial y = 0$), the displacement field reduces to $\boldsymbol{u}(x,z)$ and the Helmholtz decomposition eq. (2.14) using the potentials $\varphi(x,z)$ and $\boldsymbol{\psi}(x,z)$ reduces to

$$\boldsymbol{u}(x,z) = \begin{bmatrix} \frac{\partial \varphi}{\partial x} \\ 0 \\ \frac{\partial \varphi}{\partial z} \end{bmatrix} + \begin{bmatrix} -\frac{\partial \psi_y}{\partial z} \\ \frac{\partial \psi_x}{\partial z} - \frac{\partial \psi_z}{\partial x} \\ \frac{\partial \psi_y}{\partial x} \end{bmatrix} \tag{2.19}$$

$$= \begin{bmatrix} \frac{\partial \varphi}{\partial x} \\ 0 \\ \frac{\partial \varphi}{\partial z} \end{bmatrix} + \begin{bmatrix} -\frac{\partial \psi_y}{\partial z} \\ 0 \\ \frac{\partial \psi_y}{\partial x} \end{bmatrix} + \begin{bmatrix} 0 \\ \frac{\partial \psi_x}{\partial z} - \frac{\partial \psi_z}{\partial x} \\ 0 \end{bmatrix} \tag{2.20}$$

$$= \boldsymbol{u}^{\mathrm{L}}(x,z) + \boldsymbol{u}^{\mathrm{SV}}(x,z) + u^{\mathrm{SH}}(x,z)\boldsymbol{e}_y. \tag{2.21}$$

The first term is the in-plane longitudinal wave, the second term is the in-plane shear wave, so-called vertically polarised (SV, Shear Vertical), the third term is the antiplane shear wave, so-called horizontally polarised (SH, Shear Horizontal). SV waves are more frequently used in conventional ultrasonic testing than SH waves [Kra90]. SV waves are typically generated by mode conversion of a longitudinal wave at an interface. The physics of the interaction of SH waves with an interface perpendicular to the x-z plane is different, as an incident SH wave generates a reflected SH wave and a refracted SH wave, provided the material supports it, and no other bulk wave [Sch16]. Modelling the L and SV waves is a decoupled problem from the SH wave. For immersion inspections as considered in the thesis, SH waves are ignored as water does not support shear waves. From now on in this document, the words *shear* and *transverse* refer to the SV wave.

2.4 A short selection of imaging approaches

Ultrasonic imaging is an active area of research which has led to a multitude of approaches. The main approach considered in this thesis, synthetic aperture imaging, which includes techniques such as Total Focusing Method (TFM) and Plane Wave Imaging (PWI), is developed in detail in the following sections. It is adopted here as it is conceptually simple and leads to a good trade-off between imaging performance and noise robustness. This section presents succinctly a selection of alternative, or complementary, approaches to synthetic aperture imaging.

The decomposition of the time reversal operator (DORT) is an analysis and imaging technique based on the Singular Value Decomposition (SVD) of the transfer matrix [Pra94; Min06]. DORT arised from the study of time reversal mirrors, which focus the ultrasonic beam in complex materials by reemitting the time-reversed signals recorded by the array [Fin92]. If the inspected object consists of M ($M \leq N$, the number of probe elements) ideally resolved and omnidirectional point scatterers, then under the single scattering approximation, each scatterer is associated with a singular value, which relates to its apparent reflectivity, and two singular vectors, which relate implicitly to the focal laws needed to focus on it [Pra94; Dev00]. The SVD of the transfer matrix coincides in this case with the sum of the impulse response matrix of each scatterer. For finite-size scatterers, the scatterer response is split into multiple singular values and vectors, which leads to new avenues to characterise defects, but makes the SVD harder to interpret [Min06]. A DORT image is formed by backpropagating the singular vectors [Ker03]. DORT has lead to new research avenues in imaging complex material [Kup02], and filtering structural noise and surface waves [Lop16].

The multiple signal classification (MUSIC), or time-reversal MUSIC (TR-MUSIC), is an imaging algorithm based on DORT [Dev00; Che01; Dev05]. It exploits under the point scatterer assumption the decomposition of the transfer matrix into a signal space and in noise space to form an image. Under suitable conditions, the resolution of a MUSIC image is superior to classical beamforming imaging, therefore MUSIC can be regarded as a super resolution imaging technique. A limit is however its sensitivity to noise [Fan14].

The propagation of the ultrasonic field, and its interaction with the inspected material, is mainly linear. However, certain phenomena, such as the scattering by fatigue cracks, exhibit significant non-linearity [Sol01]. A conceptually simple method to measure the non-linearity

is to compare the image formed with physical beamforming, as described in section 2.5.2, which insonifies the material with a higher amount of energy, to an image formed synthetically with FMC/TFM, with less transmitted energy [Pot14]. This approach has been extended to multi-view imaging [Oha19].

Another imaging technique is based on the assumption that the number of flaws in a typical inspected object is small. By using a sparsity-induced penalisation, the resolution of TFM images can be improved [Car17a].

Adaptive beamforming is an alternative to delay-and-sum beamforming, where the received signals are combined with weights chosen according to the signal statistics [Syn09]. A canonical technique is Capon's beamformer [Cap69], also known as the minimum variance beamformer, where the weights are optimised to reduce the variance of the beamformed signal. This technique is sensitive to estimation errors on the spatial covariance matrix and the steering vectors, which led to the development of multiple robust adaptive beamforming techniques [Du09]. Adaptive beamforming leads to lower sidelobes and a higher resolution than delay-and-sum (ibid). Adaptive beamforming has been successfully applied to medical ultrasound [Syn07] and ultrasonic testing[Li12]. Two limits are the high computational cost, and the difficulty to estimate reliably the signal statistics [Syn09].

2.5 Total Focusing Method

2.5.1 Definition

Consider the inspection of an object using an array as shown in fig. 2.1. The element located at $\boldsymbol{x}_i$ transmits at the time $t = 0$ a wave propagating at the velocity c. The wave reaches the image point $\boldsymbol{r}$ at the time $t = r_i/c$. If there is a point scatterer located at $\boldsymbol{r}$, the wave is scattered in all directions, and reaches finally the j-th element at the time $(r_i + r_j)/c$. The record of this echo corresponds to the value $F_{ij}((r_i + r_j)/c)$ in the FMC matrix. As the same applies for any i and j, the echo appears multiple times in the dataset. The Total Focusing Method forms an image by summing these echoes over all pairs of elements [Hol05]. The TFM image amplitude at the point $\boldsymbol{r}$ is defined as

$$I^{\mathrm{TFM}}(\boldsymbol{r}) \coloneqq \left| \sum_{i=1}^{N} \sum_{j=1}^{N} a_{ij}(\boldsymbol{r}) \tilde{F}_{ij} \left(t = \frac{r_i + r_j}{c} \right) \right|. \tag{2.22}$$

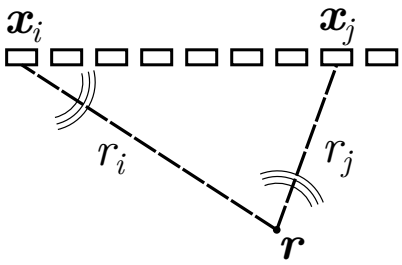

Figure 2.1 – Inspection configuration in Total Focusing Method. The i-th probe element transmits a cylindrical wave, scattered by the target $\boldsymbol{r}$, and finally received by the j-th probe element.

$\tilde{F}_{ij}(t)$ denotes the complex-valued analytic signal corresponding to $F_{ij}(t)$, obtained with the Hilbert transform. Using the analytic signal replaces in the final image the wave fronts by their envelope, which makes the interpretation easier. $a_{ij}(\boldsymbol{r})$ is an optional term for spatial filtering: it may account for the element directivity (apodisation) [Li13], or can be used to filter artefacts by removing unwanted ray paths [Iak14]. In the presence of a point scatterer at point $\boldsymbol{r}$, the terms of the summation in eq. (2.22) are in phase, so constructive interference occurs and the resulting pixel amplitude is high. For a more realistic defect, it suffices that the summands are only approximately in phase, which occurs when the phase shift introduced by the scattering of the defect between the different ray paths is small, a situation often observed. In the absence of a defect, destructive interference occurs and the resulting pixel amplitude is low.

2.5.2 Beamforming

TFM relates closely to beamforming as routinely done in phased array ultrasonic testing, where the probe elements are pulsed together with adequate delay laws to focus the ultrasonic wavefield. A phased array system creates a wave converging at the point $\boldsymbol{r}$ by pulsing for all i the element i at the time $t = -r_i/c$ (fig. 2.1) [Aza00]. Modelling the electronic pulse for the i-th element by the Dirac function $u_i(t) = \delta(t + r_i/c)$, the signal received by the j-th element is per eq. (2.1)

$$o_j(t) = \int_0^t \sum_{i=1}^{N} K_{ji}(t-\tau)u_i(\tau)\,d\tau = \sum_{i=1}^{N} K_{ji}(t + r_i/c) \tag{2.23}$$

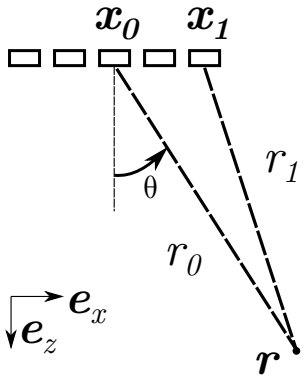

Figure 2.2 – Beamforming far from the array.

The N received signals can be furthermore focused in reception by time-shifting the j-th signal by $-r_j/c$ for all j, and by summing them together:

$$o^{\mathrm{BF}}(t) = \sum_{j=1}^{N} o_j(t + r_j/c) = \sum_{j=1}^{N}\sum_{i=1}^{N} K_{ji}(t + (r_i + r_j)/c) = \sum_{i=1}^{N}\sum_{j=1}^{N} F_{ij}(t + (r_i + r_j)/c), \quad (2.24)$$

recalling that the FMC matrix is the experimental realisation of the transfer matrix (eq. (2.7)). At $t = 0$, which is the time point corresponding to both the transmit and receive focusing, the amplitude of the A-scan is

$$o^{\mathrm{BF}}(0) = \sum_{i=1}^{N}\sum_{j=1}^{N} F_{ij}\left(\frac{r_i + r_j}{c}\right), \quad (2.25)$$

which is essentially $I^{\mathrm{TFM}}(\boldsymbol{r})$, ignoring the Hilbert transform, the apodisation and the absolute value. A TFM image may be formed using a phased array system by repeating the same process for every target point. This beamforming approaches requires one acquisition per point. The advantage of acquiring the FMC matrix first, and then calculating TFM as a post-processing step, is that only N acquisitions are necessary, regardless of the number of image points. In such case, the focusing is done synthetically rather than physically, however the result is strictly the same under the LTI assumption.

2.5.3 Beamforming far from the array

Consider the inspection geometry in fig. 2.2. By the law of cosine, the distance from element 1 to the image point $\boldsymbol{r}$ is

$$r_1 = \sqrt{r_0^2 + (x_1 - x_0)^2 - 2r_0(x_1 - x_0)\cos(\pi/2 - \theta)} \tag{2.26}$$

$$= \sqrt{r_0^2 + (x_1 - x_0)^2 - 2r_0(x_1 - x_0)\sin\theta}. \tag{2.27}$$

Far from the array, $(x_1 - x_0)/r_0 \ll 1$, so in the first order of this quantity:

$$r_1 \approx r_0 - (x_1 - x_0)\sin\theta. \tag{2.28}$$

So the difference of delay laws to focus on $\boldsymbol{r}$ between element 0 and element 1 is

$$\Delta\mathcal{T} = \frac{r_1 - r_0}{c} = \frac{(x_1 - x_0)\sin\theta}{c}, \tag{2.29}$$

which, anticipating from section 2.6, corresponds to the emission of a plane wave. Far from the array, beam focusing and beam steering are therefore equivalent. In a TFM image, this translates into a loss of image resolution as the distance from the array increases.

2.5.4 SAFT

Synthetic aperture techniques originate from the radar community [Jen06]. A successful and notorious adaptation of synthetic aperture to ultrasonic imaging is the Synthetic Aperture Focusing Technique (SAFT) [Doc86], described here for completeness. In ultrasonic testing, SAFT generally refers to the *monostatic* SAFT, that is where only one transducer transmits and receives [Wil13]. This scenario typically occurs with a monolithic transducer moved over the surface of the inspected object, but can also be emulated with an array by retaining only the diagonal of the FMC, i.e. the pulse-echo timetraces. The image is formed similarly as in eq. (2.22), except that only the pulse-echo signals are used:

$$I^{\mathrm{SAFT}}(\boldsymbol{r}) := \left| \sum_{i=1}^{N} F_{ij}\left(t = \frac{2r_i}{c}\right) \right|. \tag{2.30}$$

TFM therefore extends the monostatic SAFT by using the whole array, i.e. a multistatic configuration.

2.5.5 Time- and frequency-domain implementation

TFM as per eq. (2.22) was introduced in its time-domain implementation, an approach termed Delay-And-Sum (DAS). As each pixel calculation is independent of the others, the computation time of TFM is vastly reduced using parallelisation [Rou14].

In the geometry defined in fig. 2.1, a frequency-domain variant of TFM based on Stolt mapping is known as $\omega - k$ (omega-k) migration or wavenumber algorithm [Hun08; Lan86]. It is based on the time- and space-Fourier transform of the FMC dataset, and has a lower asymptotic computational complexity than the time-domain implementation.

The wavenumber algorithm and TFM are based on similar assumptions, so their results are comparable [Gil06]. An analytic comparison shows that the frequency-domain variants and TFM differ only by different spatial and frequency weighting [Vel10b; Wil13]. Well chosen weights obtained by correctly modelling the forward and inverse problems lead to an improvement of imaging performance compared to the standard TFM, which is based on a heuristic [Ste07; Hun08].

2.5.6 Comparison with other imaging algorithms

TFM was demonstrated to be more robust to a high level of coherent noise than the super-resolution algorithm MUSIC, and the nonlinear denoising algorithms Spatial Compounding Imaging (SCI) and Phase-Coherence Imaging (PCI) [Fan14]. For a lower level of noise, MUSIC and SCI lead however to a higher resolution.

In synthetic aperture imaging, the Signal to Coherent noise Ratio (SNR) is a decreasing function of the area of the Point Spread Function (PSF), i.e. the image of a point source in the absence of noise [Wil11]. TFM produces a tightly focused PSF, smaller than conventional PAUT techniques (plane, focused and sector B-scan), which leads to an improved SNR and a higher resolution [Hol05]. This leads some authors to qualify TFM as the gold standard of beamforming algorithms [Ban13], which drives its ongoing adoption by industries [ISO20b; ISO20a] This performance comes at a cost of a larger amount of data to acquire (FMC) and a higher computational cost compared to phased array ultrasonic testing. Two synthetic aperture techniques greatly reduce the transmission time, the amount of data to acquire and the computational burden whilst retaining a high imaging performance compared to the

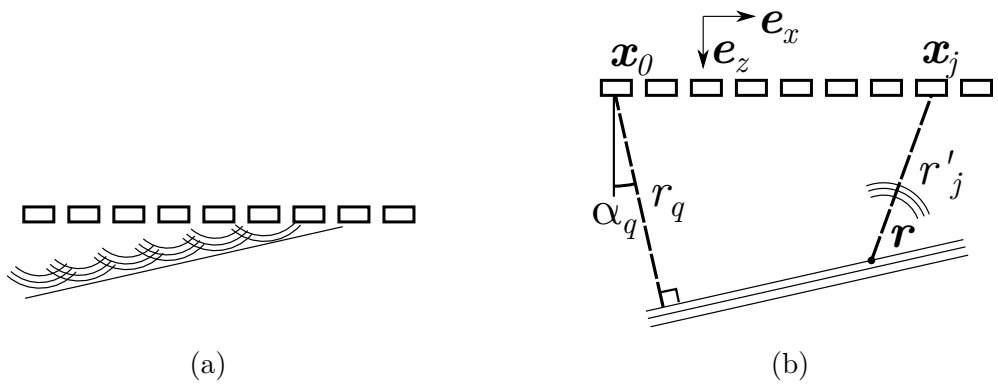

(a) (b)

Figure 2.3 – Inspection configuration in Plane Wave Imaging. (a) The cylindrical waves emitted with appropriate delays merge into a planar wave. (b) The probe transmits a plane wave, scattered by the target $\boldsymbol{r}$, and finally received by the j-th probe element.

FMC: Virtual Source Aperture (VSA) and Plane Wave Imaging (PWI). The acquisition in both cases is done by pulsing the elements with specific delay laws, instead of performing an FMC. The total number of acquisitions is typically lower than for an FMC, which leads to faster inspections. In VSA, the transmitted wave is as if it was emitted from a point source behind the array, hence the name virtual source [Sut12; Ban13]. In PWI, a plane wave is transmitted, as described in greater detail in the next section. The performance of VSA and PWI is close to TFM, despite the lower amount of data collected, which makes it possible to reduce the acquisition time. However, the performance of VSA and PWI is governed by more acquisition parameters than TFM, which is a practical disadvantage. Also, the FMC dataset has the benefit of containing all the possible information accessible to the array, as discussed in section 2.2, which makes it possible to reuse with no loss the data in ways that were not considered at the acquisition time, contrary to the PWI and VSA data.

2.6 Plane Wave Imaging

A phased array can transmit a quasi plane wave into the inspected object by using appropriate delay laws, a process named beam steering [Aza00]. Suppose that a virtual plane wave at the angle α_q goes through the array without being perturbed, as shown in fig. 2.3. By pulsing all elements at the time the virtual plane wave crosses them, the wave fronts emitted by every probe element merge into a quasi plane wave. Without loss of generality, suppose the plane

wave emerges from the reference point $\boldsymbol{x}_0$ at the time $t = 0$. Note that the wave goes through the probe element $\boldsymbol{x}_j$ at the time $(x_j - x_0)\sin\alpha_q/c$, which gives the delay law to apply for beam steering. The wave then reaches the image point $\boldsymbol{r} = \begin{bmatrix} x & z \end{bmatrix}^T$ at the time $t_q = r_q/c$, with

$$r_q = (x - x_0)\sin\alpha_q + (z - z_0)\cos\alpha_q. \tag{2.31}$$

If there is a point source located at $\boldsymbol{r}$, the scattered wave reaches the receiver $\boldsymbol{x}_j$ a time r'_j/c later. Denoting $g_{qj}(t)$ the timetrace corresponding to the q-plane wave and received by the j-th element, the echo of the scatterer located at $\boldsymbol{r}$ corresponds to the value $G_{qj}((r_q + r'_j)/c)$. PWI forms an image by summing these echoes over the Q transmitted plane waves and all receivers [Mon09; Le 16]:

$$I^{\mathrm{PWI}}(\boldsymbol{r}) := \left| \sum_{q=1}^{Q} \sum_{j=1}^{N} a_{qj}(\boldsymbol{r}) \tilde{G}_{qj}\left(t = \frac{(x - x_0)\sin\alpha_q + (z - z_0)\cos\alpha_q + r'_j}{c}\right) \right| \tag{2.32}$$

The coefficients $a_{qj}(\boldsymbol{r})$ are as in eq. (2.22) optional spatial filters.

Typically, the number of transmitted plane waves is smaller than the number of elements, so the PWI acquisition takes less time than a full matrix capture, and a higher framerate is achievable. As for TFM, a frequency-domain implementation based on Stolt mapping is known [Gar13]. The side lobes of a PWI image may be reduced using a phase coherence factor [Cru17]. The PWI acquisition matrix may be derived from the FMC matrix by summing the delayed signals, which is useful to compare imaging results from the same dataset:

$$G_{qj}(t) = \sum_{i=0}^{N} F_{ij}(t - (x_i - x_0)\sin\alpha_q/c). \tag{2.33}$$

2.7 Multi-view imaging

Multi-view imaging, also known as multi-modal imaging, extends synthetic aperture algorithms to include waves which arise from mode conversions and internal reflections. Consider the inspection configuration shown in fig. 2.4a, which approximates the inspection of the fusion face of a weld, a common scenario in ultrasonic testing. The ultrasonic array is held at a distance from and inclined relative to the top surface of the specimen to ensure good generation of longitudinal and transverse waves. The region of interest, where defects may occur, is not directly below the array. Both the inspected object and the array are immersed in water.

Because of mode conversions and internal reflections in the sample, multiple ultrasonic ray paths connect a probe element to a target point in the sample. Figure 2.4 shows six paths considered in this thesis, with zero or one internal reflection against the back wall and with longitudinal (L) and transverse (T) waves: L, T, LL, LT, TL, TT. For conciseness, the L mode in water is not included in the description of the path as this is the only mode supported in water. In the transmission nomenclature (transmitter to image point), the modes are read from the probe to the image point. In the reception nomenclature (image point to receiver), the modes are read from the image point to the probe. The full ray paths, transmitter–image point–receiver, are obtained by the combination of a transmit path and a receive path from these six. Figure 2.5 illustrates three possible combinations of paths: T–T, LT–T (or T–TL), and LL–TL (or LT–LL).

Multi-view imaging has been successfully applied to SAFT [Doc86; Lor93], TFM [Zha10b], PWI [Le 16], and MUSIC [For12]. Frequency-domain approaches were also developed [Mer20; Skj11]. Similarly to standard phased array testing [AST13], half-skip paths are used in addition to direct paths in flaw sizing. In multi-view TFM, only the ends of vertical cracks and notches are visible in direct views (tip diffraction), whereas their full length are visible in half-skip and views (specular reflection), with usually a higher signal-to-noise ratio, which leads to an accurate flaw sizing [Fel14; Fid12; Sy18b]. Various investigations have demonstrated the suitability and the overall good performance of multi-view TFM for the inspection of notches, cracks, side-drilled holes and welds [Zha10b; Fid10; Lon12; Zha12; Fel14; Fid12; Cha15; Zha17].

A multi-view TFM view is characterised by the times of flight in transmission and in reception. In transmission, the time of flight of the ray between the i-th probe element and the image point $\boldsymbol{r}$ is denoted $\mathcal{T}_i(\boldsymbol{r})$. In reception, the time of flight of the ray between the image point $\boldsymbol{r}$ and the j-th probe element is denoted $\mathcal{T}'_j(\boldsymbol{r})$. The TFM image for the rays characterised by $(\mathcal{T}, \mathcal{T}')$ is defined by (cf. eq. (2.22))

$$I^{\mathcal{T},\mathcal{T}'}(\boldsymbol{r}) := \left| \sum_{i=1}^{N} \sum_{j=1}^{N} a_{ij}(\boldsymbol{r}) \tilde{F}_{ij}\left(t = \mathcal{T}_i(\boldsymbol{r}) + \mathcal{T}'_j(\boldsymbol{r})\right) \right|. \tag{2.34}$$

The rationale for this algorithm is the same as explained in section 2.5, except that different ray paths are used. Recalling from section 2.2 that the FMC matrix is symmetric, i.e. $F_{ij} = F_{ji}$,

and if furthermore the apodisation coefficients are chosen to satisfy $a_{ij} = a_{ji}$, then

$$I^{\mathcal{T},\mathcal{T}'}(\boldsymbol{r}) = \left| \sum_{i=1}^{N} \sum_{j=1}^{N} a_{ji}(\boldsymbol{r}) \tilde{F}_{ji} \left(\mathcal{T}_i(\boldsymbol{r}) + \mathcal{T}'_j(\boldsymbol{r}) \right) \right| \tag{2.35}$$

$$= \left| \sum_{i=1}^{N} \sum_{j=1}^{N} a_{ij}(\boldsymbol{r}) \tilde{F}_{ij} \left(\mathcal{T}'_i(\boldsymbol{r}) + \mathcal{T}_j(\boldsymbol{r}) \right) \right| \tag{2.36}$$

$$= I^{\mathcal{T}',\mathcal{T}}(\boldsymbol{r}). \tag{2.37}$$

The second transition is obtained by reindexing the double summation. This demonstrates the TFM images $I^{(\mathcal{T}',\mathcal{T})}$ and $I^{\mathcal{T},\mathcal{T}'}$ are identical. As an example from fig. 2.5, the views LT–T and T–TL are identical, and so are LL–TL and LT–LL. From the $p = 6$ paths shown in fig. 2.4, $p^2 = 36$ views are possible, but the number of distinct views, p', reduces to the number of multisets of length 2 from a set of $p = 6$ elements [Wei]

$$p' = \frac{(p+1)!}{2 \times (p-1)!} = \frac{7!}{2 \times 5!} = 21. \tag{2.38}$$

This thesis aims to exploit the richness of information provided by multi-view imaging to improve the characterisation of small defects. A first step is modelling multi-view TFM images, which is the object of the next chapter.

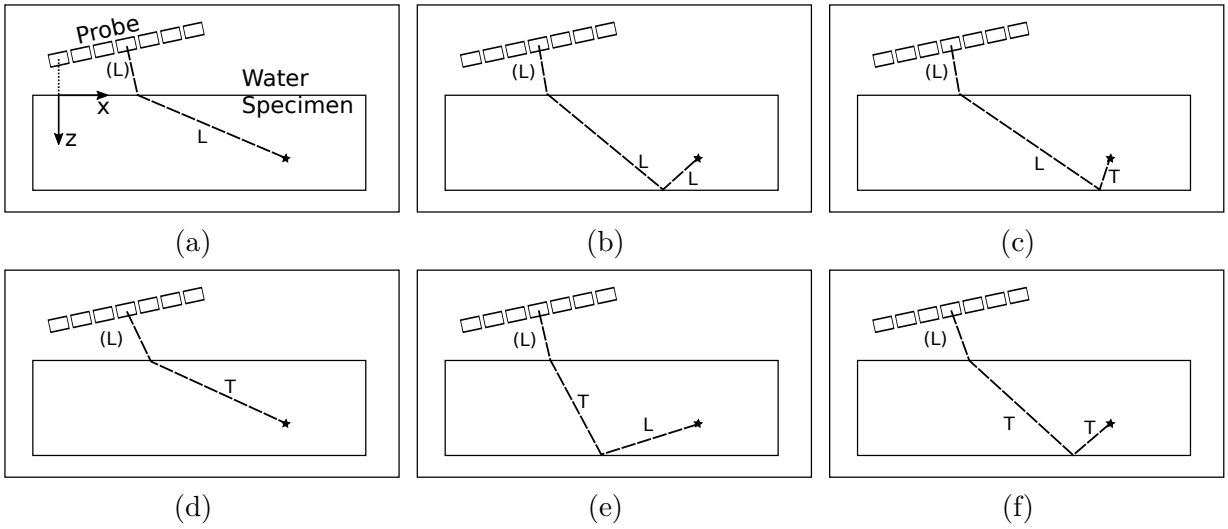

Figure 2.4 – The ray paths considered between an array element and an image point described using transmission nomenclature: (a) L, (b) LL, (c) LT, (d) T, (e) TL, (f) TT. In reception nomenclature, the modes are read from the image point instead of from the array. In both cases, the L mode in water is omitted from the path nomenclature for brevity.

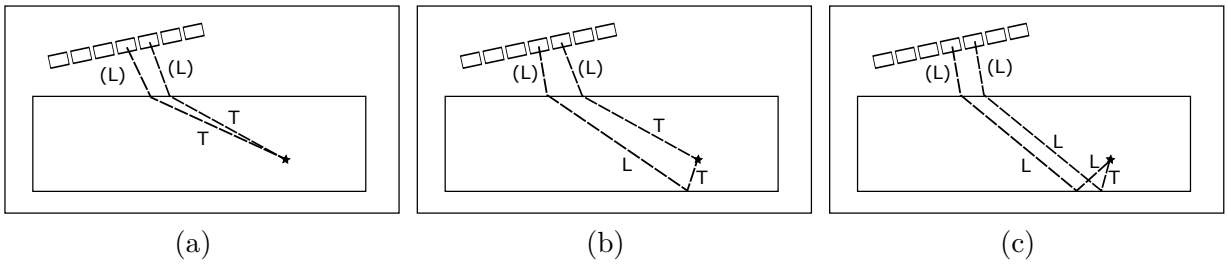

Figure 2.5 – Ray paths in direct, half-skip and full-skip views. (a) View T–T, (b) view LT–T or T–TL, (c) LL–TL or LT–LL.

Chapter 3

An ultrasonic model for multi-view immersion inspection

3.1 Introduction

The interaction of the elastic wave with the inspected object is complex due to the multiplicity of phenomena involved, such as the diffraction of the beam, its transmission and reflection at the object boundaries, mode conversion, and the scattering of the defect. Therefore, the ultrasonic response of a defect greatly varies with factors which include (i) its type, size, location and orientation, (ii) the inspection set-up (e.g. probe parameters and position relative to the specimen, specimen geometry, specimen and couplant ultrasonic velocities, specimen thickness), (iii) the ultrasonic paths used for insonifying the defect and receiving its response, i.e. the TFM view. Quantifying the ultrasonic response within and across different views is essential to determine which ones lead to the strongest signal, and consequently the highest probability of detection. This can be done experimentally with calibration blocks, or as presented in this chapter, with modelling, which is a more flexible solution. A first approach is to discretise the elastodynamic equations in time and space, with for example the elastodynamic finite integration technique [Fel95], or the finite-element method [Tho06; Hut14]. These techniques however require a rather fine discretisation, typically in the order of 10 elements per wavelength, which requires a large computational power. Even with today's resources, the computational burden is still significant for the present case where thousands of different defect locations are considered. An alternative approach is semi-analytical modelling,

which combines analytical solutions of the elastodynamics equations with numerical methods, notably numerical integration via a ray-based approach, to cope with complex scenarios where closed-form expressions of the elastic field are not known. Such models are less computationally demanding, and also decompose the ultrasonic response into the different wave modes, which eases physical interpretation. This chapter adopts the model developed by Schmerr [Sch16], after Thompson and Gray [Tho83] and Auld [Aul79].

For the detection problem, the location of the defect (if there is any) is *a priori* unknown, so any position in any view must be considered as a potential defect location. Instead of running the full semi-analytical model for any possible location, a simpler model may be derived for a higher computational efficiency. The result is a so-called sensitivity image, which maps over the imaging area the approximate theoretical defect signal. Such images have been produced for laser-induced ultrasound, assuming an omnidirectional point scatterer [Str16], for planar defects, counting the number of specular reflection to approximate the scattering function [Sy18c], and for side drilled holes and flat bottom holes, with an undisclosed model [Kwa19]. This chapter introduces a sensitivity model derived from the full semi-analytical model, assuming the defect is small and under a single-frequency approximation. The full and the simpler models are validated on three different defects, compared and discussed.

Parts of this chapter have been published in references [Bud18; Bud19]. The software implementation of the model is available at `https://github.com/ndtatbristol/arim`.

3.2 Model description

3.2.1 Overview

The objective is to model the ultrasonic response for the inspection configuration described in section 2.7. The specimen is a homogeneous isotropic metal block. The top and bottom surfaces (front and back walls) are planar. The model predicts the scatterer response for every transmitter and receiver pair during the immersion inspection of a homogeneous isotropic object. This is an adaptation of the linear time-invariant (LTI) model developed by Thompson and Gray [Tho83] and Schmerr [Sch16] to the multi-view immersion inspection. The contribution of the scatterer to the timetrace is calculated in three main steps: (1) the calculation of the incident wave amplitudes on the scatterer (transmit path), (2) the calculation of the scattering

and (3) the calculation of the wave amplitudes propagated back from the scatterer to the probe (receive path). The response of a scatterer located in the solid at point $\boldsymbol{y}$, insonified by the i-th probe element and received by the j-th element is modelled:

$$H_{ij}(\omega, \boldsymbol{y}) \coloneqq P_{ij}(\omega, \boldsymbol{y}) e^{\imath\omega\mathcal{T}_{ij}(\boldsymbol{y})} U(\omega) \tag{3.1}$$

with

$$P_{ij}(\omega, \boldsymbol{y}) \coloneqq T_i(\boldsymbol{y}) T'_j(\boldsymbol{y}) B_i(\boldsymbol{y}) B'_j(\boldsymbol{y}) D_i(\omega, \boldsymbol{y}) D'_j(\omega, \boldsymbol{y}) S_{ij}(\omega, \boldsymbol{y}) \tag{3.2}$$

where:

- $T_i(\boldsymbol{y})$ and $T'_j(\boldsymbol{y})$ encapsulate the real or complex plane wave transmission and reflection coefficients at the relevant fluid-solid interfaces encountered on respectively the transmit and receive paths [Sch16];
- $B_i(\boldsymbol{y})$ and $B'_j(\boldsymbol{y})$ describe the geometrical attenuation (beam spread) for respectively the transmit and receive paths;
- $D_i(\omega, \boldsymbol{y})$ and $D'_j(\omega, \boldsymbol{y})$ are the directivity of the probe elements associated with the transmit and receive path directions in the couplant relative to the probe;
- $S_{ij}(\omega, \boldsymbol{y})$ is the scattering amplitude;
- $\mathcal{T}_{ij}(\boldsymbol{y})$ is the time of flight of the total ray path;
- $U(\omega)$ is the ultrasonic toneburst transmitted by the transducer.

Details about these terms are given below. Except $U(\omega)$, all these quantities are view-dependent. All elements are assumed to emit the same signal $U(\omega)$, which implicitly contains the transfer function of the electronics (system function). The wave amplitudes are described by pressure in the fluid and displacement in the solid. The material attenuation in the samples considered in this paper is too low to give any significant difference, so it is ignored; it could however be accounted for if need be.

3.2.2 Scattering

Under the assumption that the incident wavefront is planar and of constant amplitude over the extent of the defect (i.e. quasi-plane wave insonification), the defect response can be

approximated by the infinite medium scattering amplitudes [Tho83][Sch16, §10.1.1]. In other words, the inspection-specific calculation of the flaw response comes down to its calculation in the canonical case of a scatterer in an unbounded medium with an incident plane wave of unit amplitude. More specifically, the scattering amplitudes are defined as the ratio of the displacement of the scattered wave at an arbitrarily-chosen reference distance divided by the displacement of the incident plane wave in an unbounded medium. For a given defect, they are functions of the frequency, the incident and scattered angles.

This simplification has three main consequences. First, the abundant literature about flaw scattering in the unbounded case can be used. In particular in this work, the scattering functions are obtained analytically for a side-drilled hole [Lop05; Mow71] and a crack (finite length, infinitesimal width) [Glu06] and finite-element analysis can be employed for arbitrary shapes of defects such as notches (finite length and width) [Vel10a]. Second, it is possible to precompute and cache the scattering amplitudes for computational efficiency. Third, it is sufficient to calculate the rays between the array elements and only one point of the defect, typically its centre. Practically, a defect is therefore modelled as a point-like scatterer with a specific frequency-dependent angular amplitude distribution which depends on its type and size because their far field scattering functions are the same.

3.2.3 Ray tracing

Calculating the ray paths between the array elements and the scatterer is an essential step because all terms in eq. (3.1) except $U(\omega)$ depend on the geometry of the rays. The rays are calculated using Fermat's minimum-time principle [Ben81, §7.1.3.1]. Because the medium is made up of homogeneous layers, and because the rays in a homogeneous medium are straight, ray tracing is done by finding using numerical optimisation the points at the intersecting surfaces which minimise the time of flight, similarly to previous work [Zha10b]. The output of the ray tracing step is the coordinates of the rays and their times of flight $\mathcal{T}_{ij}(\boldsymbol{y})$.

3.2.4 Directivity

Each element is modelled as a line-source piston (2D equivalent of a rectangular piston), which leads to the following directivity function [Sch15; Dri06]:

$$D(\omega, \boldsymbol{y}) = \operatorname{sinc} \frac{\pi a \sin\theta}{\lambda}$$

where θ is the angle between the normal of the element and the ray, a is the width of the probe element and λ is the wavelength in the couplant.

3.2.5 Beam spread

The attenuation due to the beam spreading in an infinite medium and in two dimensions is $1/\sqrt{r}$. The beam spread through a planar interface can be rigorously calculated using a high frequency approximation of the Rayleigh-Sommerfeld equation and the method of stationary phase [Sch16, §8.3.1]. The ray theory method gives equivalent results [Sch15, §2.5]. These functions are given in appendix B.

3.2.6 Ultrasonic toneburst

The ultrasonic toneburst $U(\omega)$ is the overall array response to a single reflector and encapsulates the input electrical signal and the transmit and receive dynamics of the acquisition instrument and the probe. This term is an input of the model; an experimental measurement technique to obtain it is described in [Sch07].

In this work, $U(\omega)$ is modelled as the Fourier transform of a Hann-windowed sine wave scaled by a single coefficient measured experimentally.

3.3 Sensitivity model for predicting TFM amplitudes

In this section, an approximation of the model described in section 3.2 is derived to predict quickly the TFM amplitudes anywhere in the object in an immersion inspection.

3.3.1 Single-frequency approximation

The scatterer response defined in eq. (3.1) is rewritten to separate the frequency-independent from the frequency-dependent terms:

$$H_{ij}(\omega, \boldsymbol{y}) = P_{ij}(\omega_0, \boldsymbol{y}) Q_{ij}(\omega, \boldsymbol{y}) e^{\imath\omega\mathcal{T}_{ij}(\boldsymbol{y})} U(\omega) \tag{3.3}$$

with

$$Q_{ij}(\omega, \boldsymbol{y}) \coloneqq \frac{D_i(\omega, \boldsymbol{y}) D'_j(\omega, \boldsymbol{y}) S_{ij}(\omega, \boldsymbol{y})}{D_i(\omega_0, \boldsymbol{y}) D'_j(\omega_0, \boldsymbol{y}) S_{ij}(\omega_0, \boldsymbol{y})}$$

where ω_0 is the probe centre frequency. To obtain the scatterer response, the toneburst is time-shifted, then rescaled and phase-shifted by the complex coefficient $P_{ij}(\omega_0, \boldsymbol{y})$ and finally the shape and the amplitude of the toneburst are furthermore changed by the frequency-dependent coefficient $Q_{ij}(\omega, \boldsymbol{y})$. A first-order heuristic is to consider that the change of the response amplitude is mainly caused by $P_{ij}(\omega_0, \boldsymbol{y})$ whereas the frequency-dependent variation, $Q_{ij}(\omega, \boldsymbol{y})$ causes a smaller amplitude variation in comparison. Ignoring this frequency dependence leads to the single-frequency approximation:

$$H_{ij}^{\omega_0}(\omega, \boldsymbol{y}) \coloneqq P_{ij}(\omega_0, \boldsymbol{y}) e^{\imath\omega\mathcal{T}_{ij}(\boldsymbol{y})} U(\omega). \tag{3.4}$$

Under this approximation, the scatterer response is obtained by time-shifting and multiplying the toneburst by a single complex coefficient. The fine geometric features of the scatterer, conveyed in the frequency-dependent term, are lost. However, this single-frequency model may be useful when only a first-order amplitude estimation of the scatterer response is needed and is significantly faster to run than the multi-frequency model.

3.3.2 Sensitivity images

The timetrace for the transmitter i and the receiver j is denoted $f_{ij}(t)$ in the time domain and $F_{ij}(\omega)$ in the frequency-domain. Similarly, the simulated response to a single scatterer at position $\boldsymbol{y}$ is denoted $h_{ij}(t, \boldsymbol{y})$ and $H_{ij}(\omega, \boldsymbol{y})$. The analytic signals obtained using the Hilbert transform are denoted with a tilde: for example, $\tilde{f}_{ij}(t)$, $\tilde{F}_{ij}(\omega)$.

For a given view and a N-element probe, the TFM amplitude at image point $\boldsymbol{r}$ is defined as

$$I_0(\boldsymbol{r}) \coloneqq \left| \sum_{i=1}^{N} \sum_{j=1}^{N} a_{ij}(\boldsymbol{r}) \tilde{f}_{ij}(\mathcal{T}_{ij}(\boldsymbol{r})) \right| \tag{3.5}$$

where the times of flight, $\mathcal{T}_{ij}(\boldsymbol{r})$, and the arbitrary weights, $a_{ij}(\boldsymbol{r})$, are view-dependent. The weights $a_{ij}(\boldsymbol{r})$ can be used for spatial filtering [Iak14; Li13]; in the present work, uniform weighting is used ($a_{ij}(\boldsymbol{r}) = 1$).

In the vicinity of a scatterer, the TFM amplitude $I_0(\boldsymbol{r})$ for a given view includes the scatterer response $h_{ij}(t, \boldsymbol{y})$ for this view (the desired signal) but may also include the scatterer response from other modes and wall echoes. These latter signals create artefacts in the images and interfere constructively or destructively with the desired scatterer response. However, because the times of arrival of the artefacts are in general different from those of the signals of interest, the artefacts are ignored here. Simulated artefact-free TFM images are obtained from the model by replacing the timetrace $\tilde{f}_{ij}(t)$ by the scatterer response in the imaged view:

$$I_1(\boldsymbol{r}, \boldsymbol{y}) \coloneqq \left| \sum_{i=1}^{N} \sum_{j=1}^{N} a_{ij}(\boldsymbol{r}) \tilde{h}_{ij}(\mathcal{T}_{ij}(\boldsymbol{r}), \boldsymbol{y}) \right|. \tag{3.6}$$

For example, the artefact-free T–T image only contains the T–T defect response. The actual T–T image contains other defect echoes such as the L–L response and wall echoes; they are absent of the artefact-free image. To reduce the computational burden, the approximation defined in eq. (3.4) is applied to obtain the single-frequency artefact-free image for a given view:

$$I_2(\boldsymbol{r}, \boldsymbol{y}) \coloneqq \left| \sum_{i=1}^{N} \sum_{j=1}^{N} a_{ij}(\boldsymbol{r}) \tilde{h}_{ij}^{\omega_0}(\mathcal{T}_{ij}(\boldsymbol{r}), \boldsymbol{y}) \right|. \tag{3.7}$$

Furthermore, only the amplitude at a single point of the defect image, the defect centre $\boldsymbol{y}$, is considered. For $\boldsymbol{r} = \boldsymbol{y}$, the TFM amplitude becomes:

$$\begin{aligned} I_2(\boldsymbol{r}, \boldsymbol{r}) &= \frac{1}{2\pi} \left| \sum_{i=1}^{N} \sum_{j=1}^{N} a_{ij}(\boldsymbol{r}) \int_{-\infty}^{+\infty} \tilde{H}_{ij}^{\omega_0}(\omega, \boldsymbol{r}) e^{-\iota\omega\mathcal{T}_{ij}(\boldsymbol{r})} \, d\omega \right| \\ &= \frac{1}{\pi} \left| \sum_{i=1}^{N} \sum_{j=1}^{N} a_{ij}(\boldsymbol{r}) \int_{0}^{+\infty} H_{ij}^{\omega_0}(\omega, \boldsymbol{r}) e^{-\iota\omega\mathcal{T}_{ij}(\boldsymbol{r})} \, d\omega \right| \\ &= \frac{1}{\pi} \left| \sum_{i=1}^{N} \sum_{j=1}^{N} a_{ij}(\boldsymbol{r}) \int_{0}^{+\infty} P_{ij}(\omega_0, \boldsymbol{r}) U(\omega) \, d\omega \right|. \end{aligned} \tag{3.8}$$

Noting that $\frac{1}{\pi} \int_0^{+\infty} U(\omega) \, d\omega = \tilde{u}(0)$, the sensitivity image [Str16; Bud18] is defined as:

$$E(\boldsymbol{r}) \coloneqq I_2(\boldsymbol{r}, \boldsymbol{r}) = \left| \tilde{u}(0) \sum_{i=1}^{N} \sum_{j=1}^{N} a_{ij}(\boldsymbol{r}) P_{ij}(\omega_0, \boldsymbol{r}) \right|. \tag{3.9}$$

For a given view, the sensitivity image, $E(\boldsymbol{r})$, represents an estimate (under the single-frequency assumption) of the TFM amplitude that would be measured if a defect of the prescribed type

existed with its centre at $\boldsymbol{r}$. The quality of the estimation is discussed in a later section of this paper. This quantity requires less computation than the artefact-free TFM images $I_1(\boldsymbol{r}, \boldsymbol{y})$ and $I_2(\boldsymbol{r}, \boldsymbol{y})$ because (i) no frequency integration is required and (ii) the TFM algorithm is performed at a single point, the defect centre, instead of on a grid in the vicinity of the defect. One may notice that the exact form of the toneburst $U(\omega)$ is ignored in this sensitivity model because of the single-frequency assumption; only the amplitude of its envelope at $t = 0$, $|\tilde{u}(0)|$ matters and acts in practice as a scaling coefficient.

3.3.3 Time interpolation of timetraces in TFM

Numerically, the TFM is usually calculated in its time-domain form (eqs. (3.5) to (3.7)) where the timetraces are linearly interpolated between time samples [Hol05]. However, because of this linear interpolation, the pixel amplitudes obtained with the time-domain forms are systematically lower than the ones obtained with the frequency-domain forms of TFM like eqs. (3.8) and (3.9). The magnitude of this difference depends on the sampling rate and frequency content of the signals and varies from pixel to pixel; at 25 MHz sampling rate with a nominal centre frequency of 5 MHz, it was observed to be around 2 dB. In practice, linear interpolation is generally sufficient and a heuristic correction based on the sampling rate and the ultrasonic frequency could be applied if desired; however, in order to systematically eliminate the effect of this variation from subsequent comparisons, the more accurate Lanczos interpolation [Duc79; Tur90] is used in this work:

$$k(t) = \sum_{n=\lfloor t/T \rfloor - a + 1}^{\lfloor t/T \rfloor + a} k(nT) L(t/T - n) \tag{3.10}$$

where $1/T$ is the sampling frequency, $L(x)$ is the Lanczos kernel of order b:

$$L(x) = \begin{cases} \operatorname{sinc}(\pi x) \operatorname{sinc}(\pi x / a) & \text{if } -a < x < a, \\ 0 & \text{otherwise.} \end{cases}$$

With a kernel of order $a = 3$, the error is reduced to 0.001 dB, at the cost of a 10 times slower computation of TFM images compared to linear interpolation (CPU implementation).

3.4 Multi-frequency model validation

3.4.1 Apparatus

The multi-frequency model defined previously is validated in this section against experimental data from two different aluminium blocks, and data obtained from the finite-element method (FEM) in three different cases described in table 3.1. The FEM data were kindly provided by Dr Artem Kashubin, and were generated using a two-dimensional hybrid model which couples (i) a similar analytical model for the wave propagation in the fluid and (ii) the Pogo solver [Hut14] for modelling the elastic propagation and interaction inside the solid [Kas20]. The nodes at the fluid/solid interfaces of this hybrid model act as Huygens sources for the pressure in fluid and for the vertical displacement in the solid. The material defined in the FEM simulation has the density and velocities of a copper-nickel alloy but has no material attenuation.

In the experimental datasets, each timetrace is time-shifted by the instrument acquisition delay, measured by subtracting the times of arrival of two consecutive front wall echoes in normal incidence, so that the maximum amplitude of the transmitted toneburst $\tilde{u}(t)$ is obtained at $t = 0$. The probe location is calculated from the times of arrival of the front wall echo in the pulse-echo timetraces, as described in appendix A. The longitudinal and transverse velocities in the sample material are obtained under the assumption that the correct values maximise the TFM amplitudes of the back wall echo; the block thickness being known, the longitudinal and traverse velocities are thereby obtained from the L–L and L–T views, respectively.

The timetraces (experimental, FEM, simulated) are filtered with a fourth order Butterworth bandpass filter to remove potential low-frequency offsets and high-frequency noise. The filter has negligible impact on the toneburst bandwidth.

For the ray tracing, the distance between two consecutive points of the discretised interfaces is 30 µm. Compared to a twice as coarse grid, the largest observed difference of TFM defect amplitudes for the notch dataset was 0.02 dB, which demonstrates the interfaces are fine enough to make the error negligible.

To measure the model scaling coefficient $|\tilde{u}(0)|$, the back wall reflection for the L–L path is modelled using a ray-based approach consistent to that described above for point-like scatterers. The amplitudes of the back wall are measured by taking for each experimental/FEM timetrace

the maximum of the envelope of the signal near the expected time of arrival. The ratio between the modelled and the experimental back wall amplitudes is the model scaling; this ratio is assumed to be the same for all pairs of timetraces. An ordinary least squares regression is performed for robustness to obtain the final model coefficient. The back wall reflected for the path L–L was chosen because it provides a strong signal, clearly visible in all timetraces. In a previous work [Bud18], the front wall reflection was used instead; however, the back wall appears to be less sensitive to small probe misalignments and therefore provides a more robust estimation of the model scaling. A proper investigation would require a three-dimensional model to understand the effect of the out-of-plane misalignment in the front and back wall amplitudes.

3.4.2 Results

Figures 3.1 and 3.2 show the simulated and experimental/FEM defect response images in the different views on a dB scale; in each image, 0 dB corresponds to the maximum amplitude in the magenta box. A good qualitative agreement is achieved: the tip diffraction and the specular reflection of the notch, and the various defect patterns are generally correctly simulated.

Figure 3.3 shows a quantitative absolute comparison of the maximum TFM amplitudes around the defect in experimental/FEM images $I_0(\boldsymbol{r})$ and simulated ones $I_1(\boldsymbol{r}, \boldsymbol{y})$. The measurement area is a square of side 5 mm (magenta squares in figs. 3.1 and 3.2); the pixel size is 0.25 mm. Due to computational limitations, the simulation time of the FEM data is shorter than the times of arrival of the waves in some views therefore only 12 views are available for the crack dataset. The median/standard deviation of the errors for all views are -1.7/2.4 dB (notch), 0.0/3.1 dB (SDH) and 0.1/1.5 dB (crack). For 48 views out of 54, the agreement is within ±3 dB. The defect response varies significantly between the views: a variation of 20 dB (crack), 30 dB (notch) and 36 dB (SDH) is observed between the highest and lowest TFM amplitudes. These large variations are correctly explained by the model.

In views where the defect response is low (approximately less than -20 dB relative to the brightest view), the defect may be hard to distinguish from the surrounding artefacts because of their similar or stronger amplitudes. In this situation, the assumption that the measured amplitude is close to the artefact-free one becomes questionable.

Table 3.1 – Description of the Three Validation Cases.

Dataset name	Crack	Notch	SDH
Source	FEM	Experiment	Experiment
Defect properties			
Type	crack	notch	SDH
Size	0.5 mm	3×1 mm	Ø1 mm
Orientation	110°	90° (vertical)	/
Location x (mm)	26	46	46
Location z (mm)	10	20	20
Block properties			
Material	copper nickel	aluminium	aluminium
L velocity (m/s)	5050	6384	6410
T velocity (m/s)	2534	3156	3150
L att. (Np/m)	0	0[1]	0[1]
T att. (Np/m)	0	0[1]	0[1]
Density (kg/m^3)	7800	2700[1]	2700[1]
Thickness (mm)	20	40	40
Probe properties			
Number of elements	110	64	64
Centre frequency (MHz)	5	2.5	2.5
Element pitch (mm)	0.17	0.5	0.5
Probe stand-off (mm)	17.0	29.9	29.8
Probe angle	11.0°	12.5°	12.5°
Filter passband (MHz)	2–8	1–4	1–4

[1] Not measured, approximated from literature.

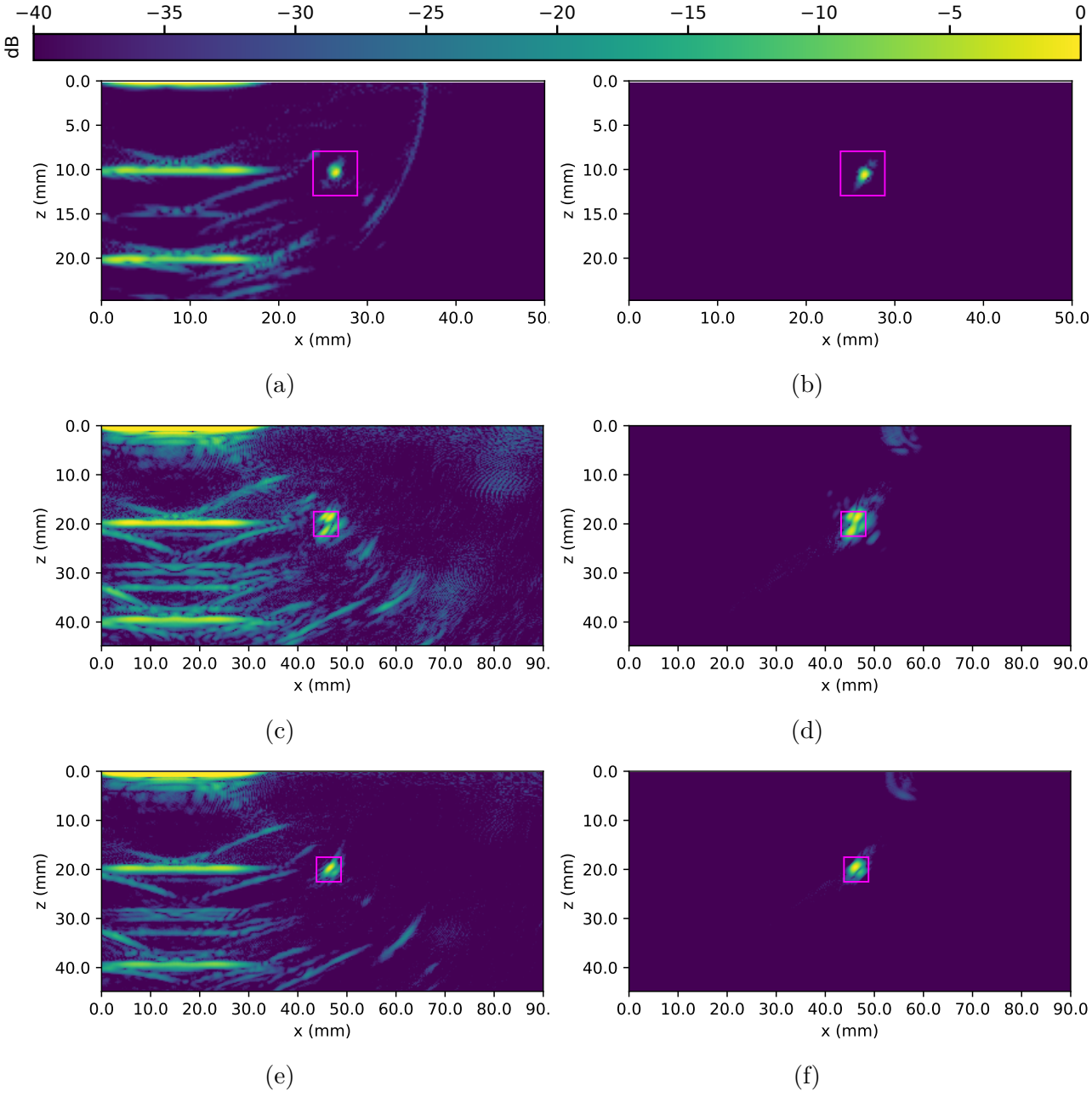

Figure 3.1 – TFM images of view T–T. Left column: experimental images $I_0(\boldsymbol{r})$. Right column: artefact-free simulated images $I_1(\boldsymbol{r}, \boldsymbol{y})$. Top row: crack. Middle row: notch. Bottom row: SDH. In each image, 0 dB corresponds to the maximum amplitude in the magenta box.

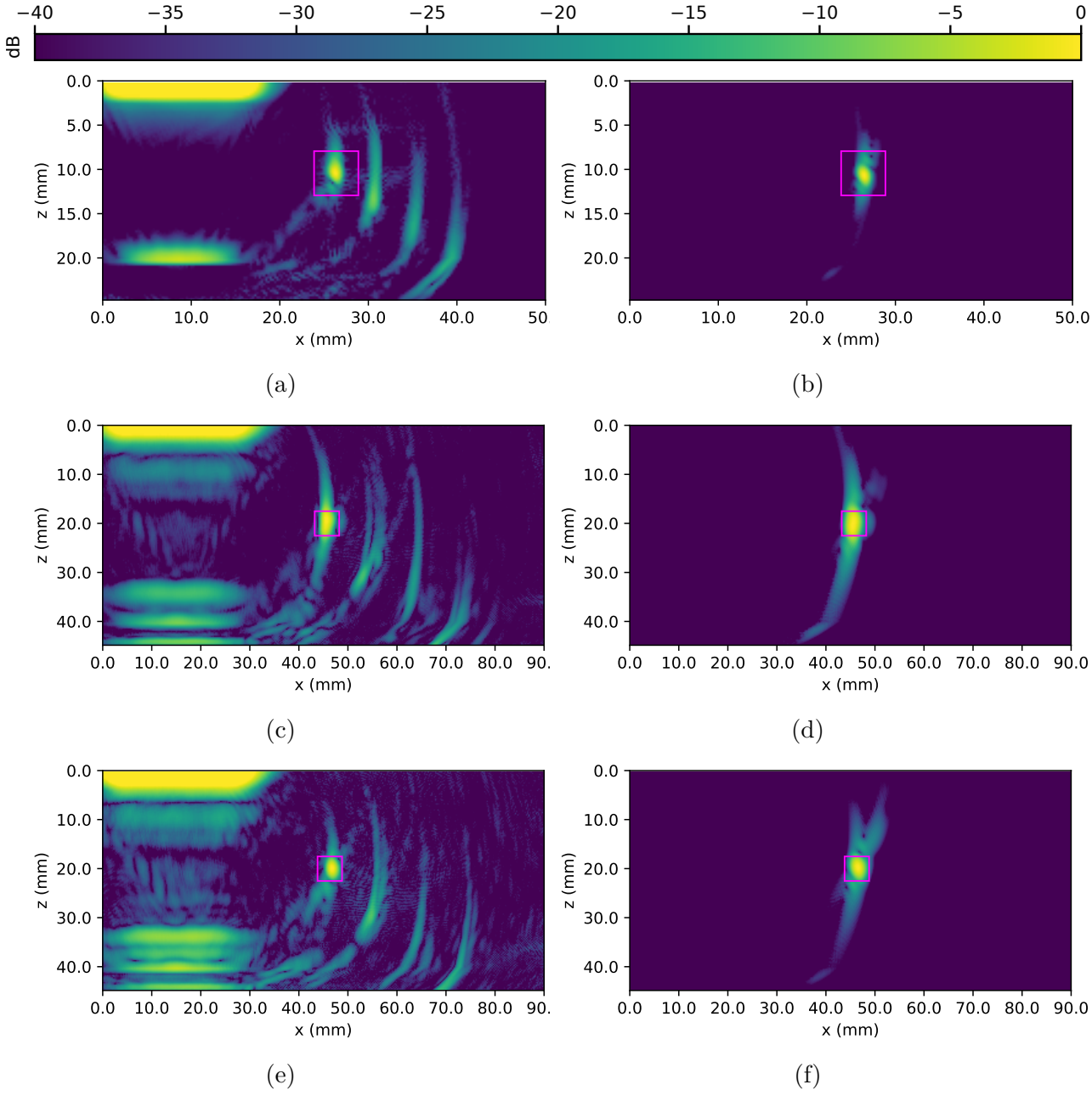

Figure 3.2 – TFM images of view LL–T. Left column: experimental images $I_0(\boldsymbol{r})$. Right column: artefact-free simulated images $I_1(\boldsymbol{r}, \boldsymbol{y})$. Top row: crack. Middle row: notch. Bottom row: SDH. In each image, 0 dB corresponds to the maximum amplitude in the magenta box.

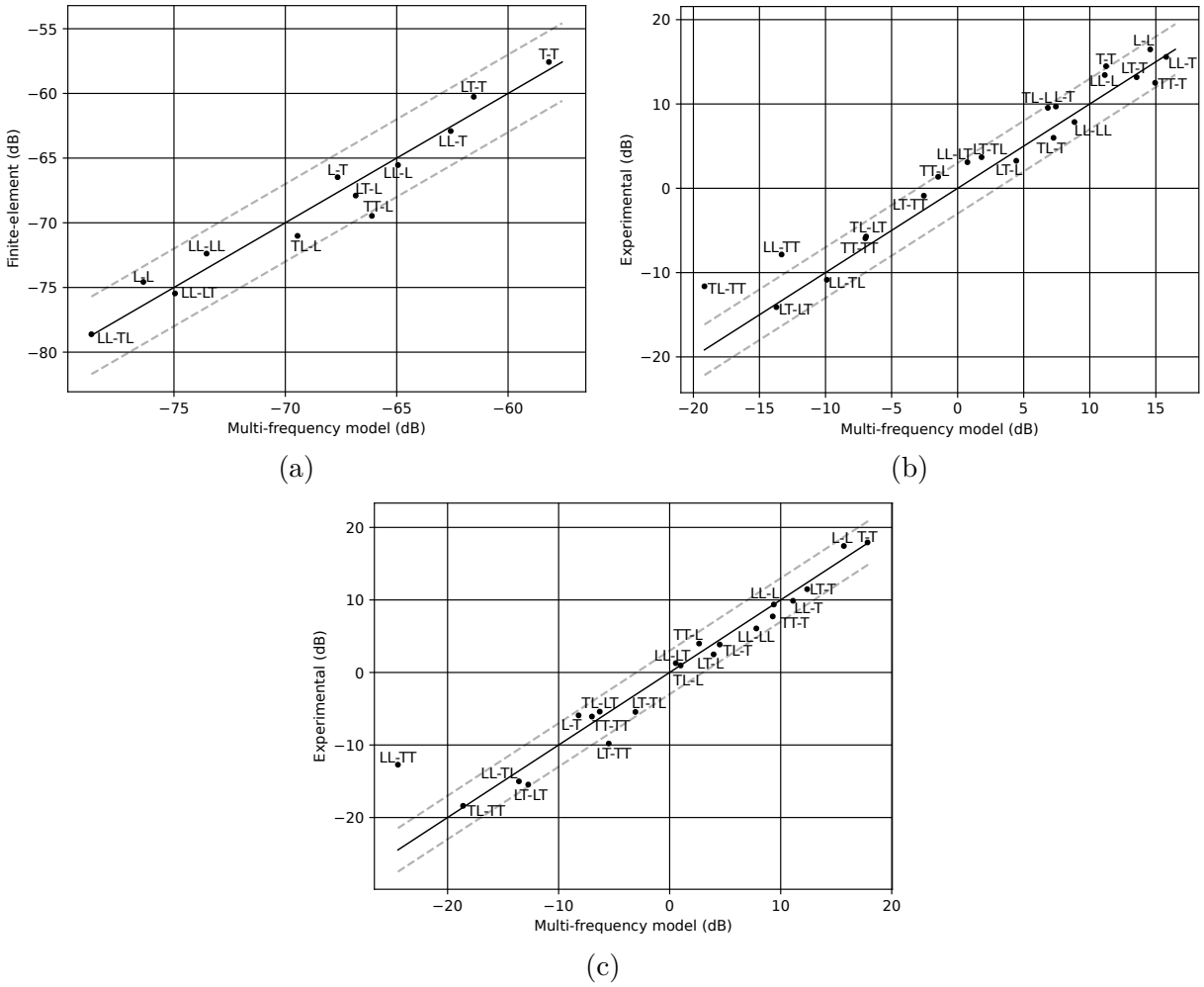

Figure 3.3 – Comparison of the peak amplitude scatterer responses in artefact-free multi-frequency images $I_1(\boldsymbol{r}, \boldsymbol{y})$ and experimental/FEM images $I_0(\boldsymbol{r})$ for (a) a crack, (b) a notch, (c) a SDH. The solid black line corresponds to a perfect agreement. The dashed lines corresponds to an agreement of ±3 dB. The 0 dB point is set arbitrarily.

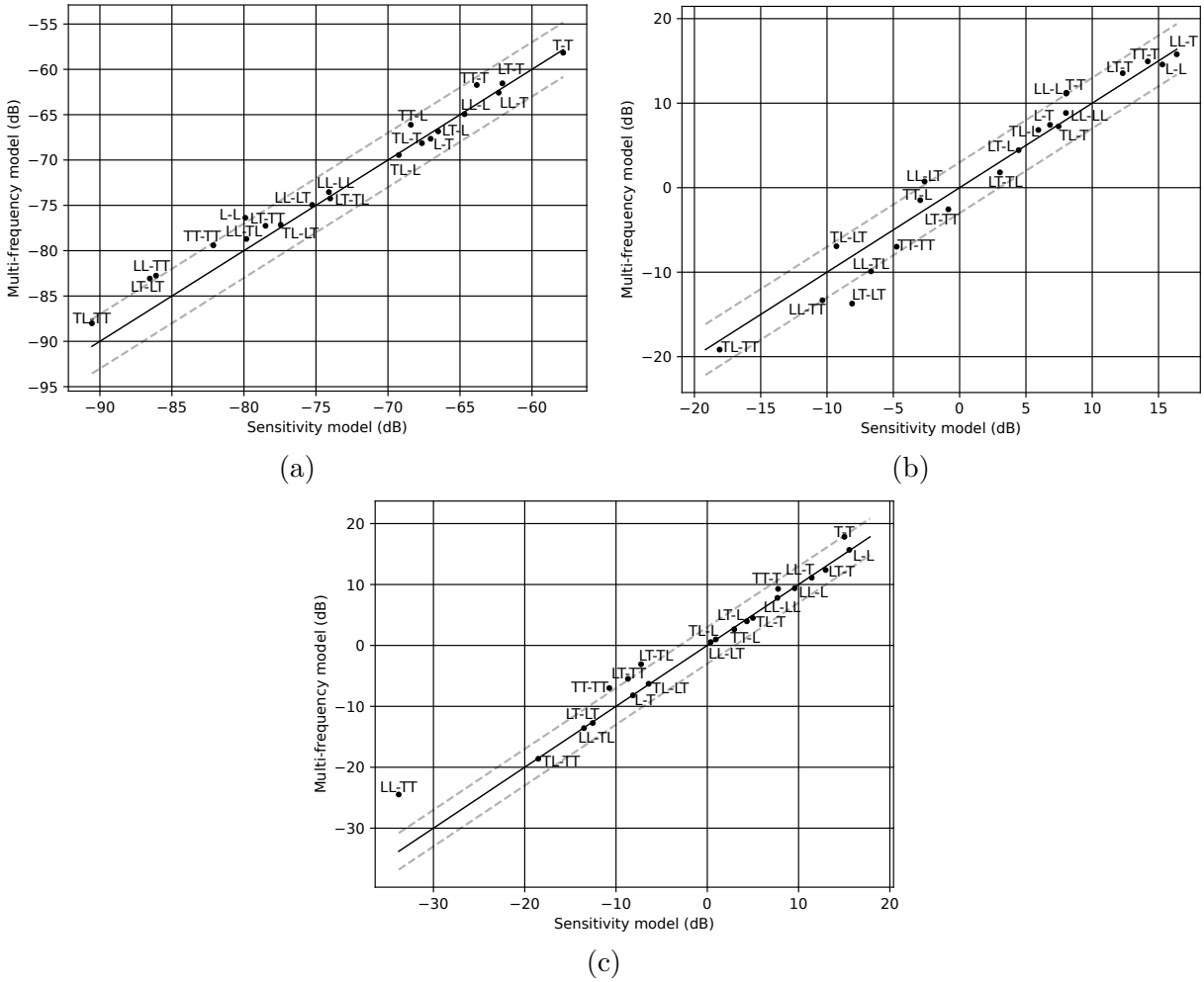

Figure 3.4 – Comparison of sensitivity image $E(\boldsymbol{r})$ and simulated multi-frequency TFM image $I_1(\boldsymbol{r}, \boldsymbol{y})$ for (a) a crack, (b) a notch, (c) a SDH. The 0 dB point is set arbitrarily.

3.5 Sensitivity model validation

The sensitivity model defined in eq. (3.9) provides an estimate of the TFM amplitude of a defect. To assess the validity of this estimation, fig. 3.4 shows the absolute comparison of the sensitivity model amplitudes $E(\boldsymbol{r})$ against the maximum artefact-free multi-frequency TFM images $I_1(\boldsymbol{r}, \boldsymbol{y})$ near the defect. The median/standard deviation of the errors for all views are 0.0/2.3 dB (notch), -0.1/2.3 dB (SDH) and -0.5/1.5 dB (crack). For 51 views out of 63, the agreement is within ±3 dB.

The sensitivity model assumes that the pixel amplitude at the defect centre is a good estimate of the peak amplitude. This assumption falls short when the amplitude at the defect centre is a trough due to a phase effect (for example in fig. 3.2f, even though the estimate

remains good in this case). The magnitude of this error between the sensitivity model and multi-frequency model depends on the view and the defect type and becomes stronger at higher frequencies. In the presented datasets, it appears particularly in the view LL-TT of the SDH. Despite this, a good agreement is achieved.

These results *a posteriori* validate the single-frequency assumption (eq. (3.4)): the peak TFM amplitudes are mainly explained by a single-frequency model; the multi-frequency dependence of the model, including the scattering, has a limited effect in comparison. However, finer effects such as the tip diffraction require a proper multi-frequency model; therefore, the images produced with the single-frequency model are not representative of the defects (images available in supporting data).

Figure 3.5 shows the predicted TFM amplitudes of a notch anywhere and for any view; the configuration is the same as the notch dataset described above except that 14,299 defect locations are considered. These sensitivity images exhibit large variations of amplitudes, both within each view and across the views. They show clearly the areas of high amplitudes and the blind valleys, which are specific to the defect type and orientation. These images could be used to assess the suitability of an inspection configuration to detect a given defect. For example, the views L–L, LL-T and TT–T seem particularly suited to inspecting a vertical notch at $x \approx 50$mm because they provide the highest TFM amplitudes and because they do not exhibit strong blind spots in this area.

The advantage of the sensitivity model is its high computational efficiency. The total runtime for these 14,299 defect locations, excluding the pre-calculation of the defect scattering distributions which is performed in a first step and cached, is 75 s for 21 views on a desktop computer (Intel Core i7-4790 3.6 GHz quad-core processor; 16 GB RAM). To obtain equivalent results to the sensitivity model for 14,299 candidate defect locations, it would take 5 days using the artefact-free multi-frequency model $I_1(\boldsymbol{r}, \boldsymbol{y})$ (30 seconds per location) and 39 years with the current finite-element analysis implementation (1 day per location). The sensitivity model is therefore 3 orders of magnitude faster than the multi-frequency analytical model. This significant speed-up is obtained because the sensitivity model provides only an *estimate* of the TFM amplitude, under the single-frequency approximation and under the assumption that the pixel amplitude at the defect centre is representative of the actual peak amplitude.

Finally, instead of computing the TFM amplitudes of a given defect type and orientation

at different positions, this fast model could also conversely be used to quickly predict the TFM amplitudes of different defect types and orientations at one position, as an input for defect characterisation techniques. Its speed, flexibility and relative accuracy being crucial benefits.

3.6 Conclusion

A two-dimensional ray-based forward model for small defects was described and compared against FEM and experimental data for the inspection of a side-drilled hole, a crack and a notch. The model is used to predict artefact-free images of the defect. The model results are normalised against the measurements of the back wall echo. The model agrees with the experimental/FEM data within typically ±3 dB. Under a single-frequency assumption and assuming the maximum TFM intensify of the defect is at located at its centre, which is most often the case for small defects, a simpler model named the sensitivity model is derived. A typical ±3 dB agreement between this simple model and the fuller one is achieved. The sensitivity model is typically 3 orders of magnitude more computationally efficient and therefore is used to compute sensitivity images in less than two minutes, which are the predicted TFM amplitudes of a given defect in any view and anywhere. These images provide quantitative results to determine the views and the areas where a given defect type provide a large response. They could therefore be used a helper to design a multi-view TFM inspection. The NDT manufacturer Olympus presented in 2019[1] similar TFM sensitivity images [Kwa19], which demonstrates a certain industrial interest for this technology.

The computational efficiency of the model makes it possible to compare a large variety of candidate scatterers against an unknown defect, which is used for defect characterisation in the next chapter.

[1]Sensitivity images for multi-view TFM inspections in the form introduced in this chapter were first presented by the author at the 44th Annual Review of Progress in Quantitative Nondestructive Evaluation in 2017

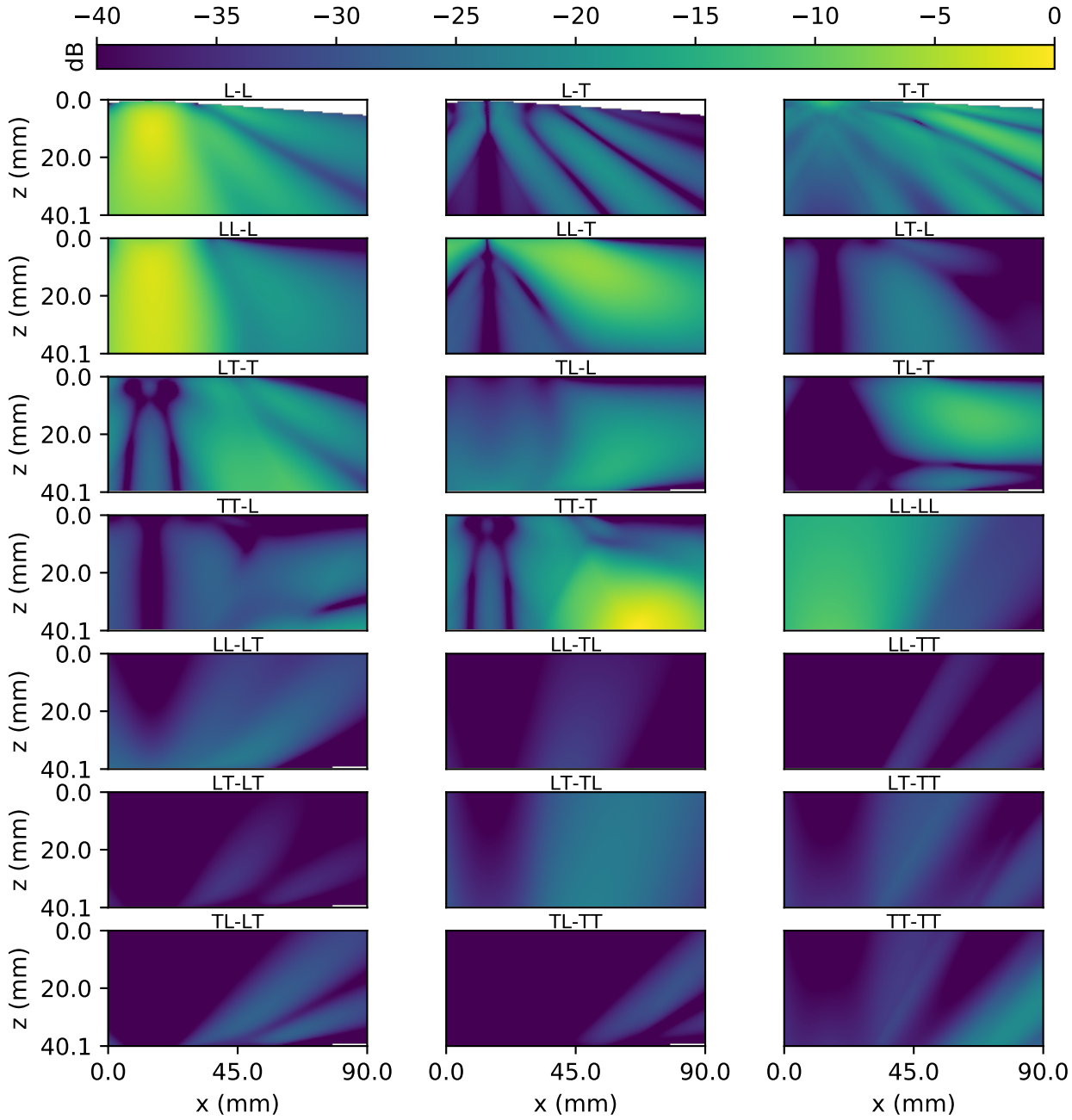

Figure 3.5 – Sensitivity images (dB) for a 3×1 mm vertical notch.

Chapter 4

Defect characterisation

4.1 Introduction

Defect characterisation is an essential step of nondestructive testing which aims to determine the shape and the size of a defect once detected. In ultrasonic testing, the adoption of array transducers led to the development of numerous techniques, as highlighted by Felice and Fan in a recent review [Fel18]. Larger defects (size higher than a few wavelengths) can typically be sized by analysing the tip diffraction and the specular reflection echoes in an A-scan or ultrasonic image. Multi-view Total Focusing Method (TFM) has been experimentally demonstrated to be especially reliable and accurate for such sizing [Sy18b, chapter 5][Fel14]. However, the characterisation of smaller defects (size lower than a few wavelengths), where these echoes are of low amplitude compared to noise, remains difficult. Previous work for characterising small defects has focused on measuring and exploiting the far-field scattered wave field, via the so-called scattering matrix. A common method is to measure the scattering matrix, or a proxy for it, and to find the idealised defect (typically, a perfect crack or an elliptical void) which has a scattering matrix that most closely matches that of the unknown defect. These techniques differ mainly by the feature used for the comparison and the class of idealised defect. Zhang et al. used the maximum amplitude of the scattering matrix to characterise crack-like defects: the angle at which it occurs give the orientation, the length is obtained by comparison against a finite-element model [Zha08]. For the same purpose, other features have also been used such as the width at half maximum of the scattering coefficients of pulse-echo traces [Vel09; Zha10b], the sum of differences of the measured and modelled normalised scattering matrices

[Tan15], correlation coefficients and structural similarity index [Bai15b], and classifiers in the principal component space [Bai15a; Vel17]. These techniques work best for defects close to the ultrasonic array, so that they can be probed over a large range of angles to extract a portion of the scattering matrix. However, the geometry of many practical applications precludes this approach. In the configuration where the defect is far away from the ultrasonic array and insonified over a narrow range of angles, Zhang et al. observed that volumetric and crack-like defects can be distinguished by comparing their image amplitudes in the multi-view Total Focusing Method (TFM) algorithm [Zha17; Zha10b]. Instead of using a continuous region in the scattering matrix for one mode combination as the defect signature, the proposed approach uses the maximum responses in multi-view TFM images; effectively these correspond to values taken from multiple smaller regions in the scattering matrices for different mode combinations. The current chapter adopts this latter approach, and proposes a quantitative framework to compare these amplitudes against reference scatterers to ultimately determine which ones are the most similar to the unknown defect. Following previous work [Mor14; Bai15a], two types of reference scatterers as considered: the ellipse as an idealised volumetric defect (void, inclusion), and straight line discontinuity as an idealised crack. The latter is henceforward referred to as crack for brevity. The inference is done using a Bayesian framework.

4.2 Characterisation model

4.2.1 Overview

The aim is to characterise an unknown defect from its response in multi-view TFM images. To do so, it is compared against reference scatterers. The peak TFM image amplitudes at or close to the defect location in all exploitable views act as a defect signature. The ultrasonic model described in chapter 3 is used to predict the TFM amplitudes of the reference scatterers. The mismatch between the measured response and the closest reference scatterer is treated stochastically with probabilistic modelling. The Bayesian framework is adopted for this process. Under this approach, both the vector of observations, denoted x, and the vector which parametrises the reference scatterer, denoted ξ, are treated as random vectors. Two probability distributions are necessary for the inference. The first one describes the plausible TFM amplitudes given that the true defect is a known reference scatterer (forward

problem); formally, it is the probability distribution of the observation vector x conditional on the parameter vector ξ. The second one describes the knowledge, or the lack of knowledge, on the parameter vector ξ prior to the observation; it is called the prior distribution. Bayes' theorem solves the inverse problem by providing the probability distribution of the parameter vector ξ given the observation x, called the *posterior* distribution. The inference is made by exploiting the posterior distribution.

The reader is referred to classic books on Bayesian analysis for further information, such as (alphabetically) Gelman [Gel13], Kruschke [Kru11], Marin and Robert [Mar07], Robert [Rob07]; this last reference notably contains a philosophical defence of this framework in chapter 11. Bayesian analysis relies heavily on conditional probability; a brief refresher on this matter is provided in this thesis in appendix D.4. Throughout this chapter, for brevity and as usually done in the Bayesian literature, the conditional density of a random variable Y given an observation $X = x$, formally $f_{Y|X=x}(y)$, is denoted $f(y \mid x)$. $f(x, y) = f_{X,Y}(x, y)$ denotes the density of the joint distribution of (X, Y). $f(x) = f_X(x)$ denotes the density of X unconditionally on all other random variables. $f(x)$ will also denote the probability mass function, $P(X = x)$, when X is a discrete random variable.

4.2.2 Defect signature

The vector of the peak TFM image amplitudes (absolute value of the complex image amplitude) close or at the defect location in each view acts as a signature of the defect. It is denoted $x = (x_k)_{k=1\ldots n}$, where n is the number of views. This vector is used to compare the unknown defect against the reference defect; in machine learning terminology, this is the feature of the model. The case of interest here is relatively small defects, so the defect image depends primarily on the point spread function. The actual shape of the defect is unresolved due to the diffraction limit, which justifies using a single amplitude per image.

4.2.3 Reference scatterers

The unknown defect is compared against reference scatterers, parametrised by the vector ξ. It is essential that these scatterers cover a wide range of shape and orientation to achieve a good characterisation. Two distinct sets are used: ellipses and cracks. In both sets, the scatterers

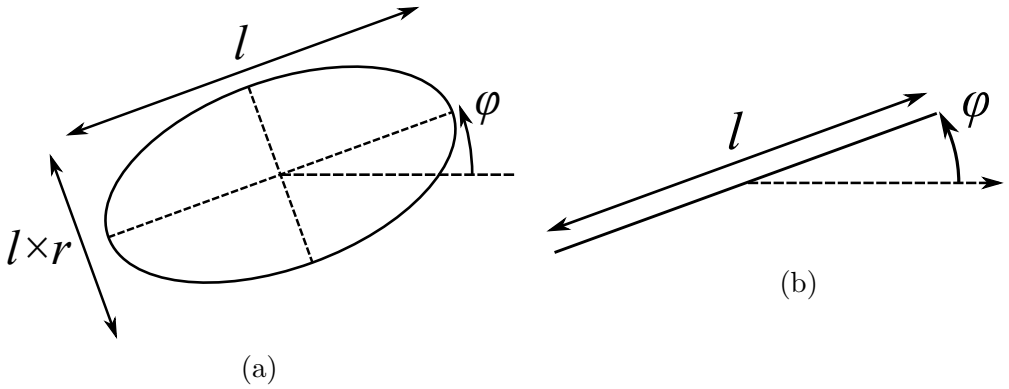

Figure 4.1 – Parametrisation of the ellipse (a) and the crack (b).

are two-dimensional (infinite length in the third dimension) and smooth. Figure 4.1a shows the parametrisation of the ellipse, $\xi = (l, r, \varphi)$: l is the major length, $r \in]0, 1]$ is the aspect ratio, which is the ratio of the minor length to the major length, and φ is the angle. Figure 4.1b shows the parametrisation of the crack, $\xi = (l, \varphi)$: l is the length, and φ the angle.

The TFM amplitudes of a reference scatterer are calculated with the sensitivity model from chapter 3; the scattering functions are obtained with a finite-element method [Vel10a] for the ellipse, and an analytical model for the crack [Glu06]. The ultrasonic model is run on a discrete set of reference defects, of evenly spaced parameters. The limits of the parameters are as follows. The angle φ ranges between 0° and 180° with a step of 2.5°, which covers the whole range of possible angles due to the line symmetry along the defect main axis. The length l ranges between 0.1λ and 2λ with a step of 0.1λ, where λ is the longitudinal wavelength in the inspected object. There is little incentive to consider larger defects as in such scenario image-based sizing can be applied [Zha10a]. For the ellipse, the aspect ratio r ranges between 0.1 (thin ellipse) and 1 (circle) with a step of 0.1; thinner ellipses were not considered as their difficult geometry degrades the quality of the finite-element mesh. The TFM amplitudes of defects which are not evaluated with the ultrasonic model are estimated using cubic spline interpolation. The interpolation error is negligible compared to the ultrasonic model error: the former is bounded by the difference of amplitudes between two model evaluations, which is on average 0.8 dB here, whereas the latter is typically around 3 dB as shown in chapter 3.

Here, it is assumed that little is known on the defect before the characterisation, so the chosen prior distribution of each of the parameters l, r and φ, denoted $f(l)$, $f(r)$, $f(\varphi)$, is a uniform distribution with the limits specified in the previous paragraph. Because these parameters are

independent, the prior on ξ is $f(\xi) = f(l)f(r)f(\varphi)$ for the ellipse and $f(\xi) = f(l)f(r)$ for the crack. The prior distribution can be changed to reflect further knowledge on the expected defects. For example, if it is known that the defects in a specific component are growing preferentially in a given orientation, $f(\varphi)$ could be changed to a normal distribution centred at this angle.

4.2.4 Likelihood

Suppose that the true defect is a known scatterer ξ. The objective is to determine what defect signatures are likely to be observed; in other words, to determine the likelihood function for the observation vector x conditionally on ξ, denoted $f(x \mid \xi)$. The ultrasonic model described in chapter 3 gives a starting point; the defect signature generated with this model is denoted $h(\xi)$ and is in dB. However, there are multiple sources of uncertainties that need to be accounted for. As for any physics model, the adopted ultrasonic model is a simplification of the reality, based on various assumptions and approximations: linear behaviour of the transducer, homogeneity and isotropy of the material, two-dimensional treatment, plane wave approximation, etc. As the reality is more complex, there is a model error. Also, the unknown defect is likely not a perfect ellipse or crack; the reference scatterers only approximate the real defect. Modelling the uncertainties deterministically is difficult if not impossible; they are therefore treated here as a single additive stochastic error term ε in dB scale (multiplicative error in linear scale), that is

$$x = h(\xi) + \varepsilon. \tag{4.1}$$

The random and the structural noise, usually modelled with an additive term in linear scale, are not covered in this model, as they are both small compared to the multiplicative noise. Figure 4.2 shows the empirical distribution of the error ε for the three datasets described in table 3.1 grouped together. All values but one are scattered around 0. The density of the main cluster is approximatively bell-shaped, and is slightly skewed towards positive errors, that is the ultrasonic model underestimates the results. There is a single outlier at 21 dB, which corresponds to the measurement of an artefact in the SDH dataset. It is not judicious to use this empirical distribution as the *true* distribution of ε as it may not generalise to other datasets (overfitting); a simpler (less accurate but more generalisable) distribution is needed. Because the density is approximatively bell-shaped, ε could be assumed to be normally

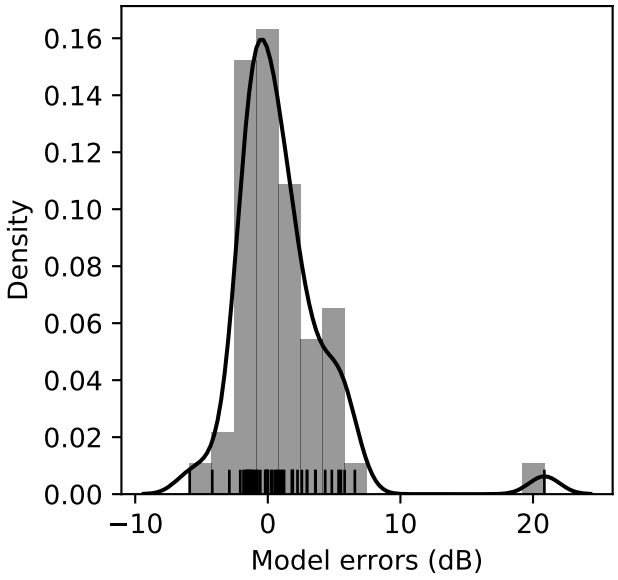

Figure 4.2 – Distribution of errors in dB between the sensitivity model and the observations for the three datasets described in table 3.1. 54 data points. Histogram, empirical density obtained with kernel density estimation, and rug plot.

distributed. However, such a model would be very sensitive to outlying values, which are likely to arise with real data. A more robust regression can be achieved by using as an alternative the Student's t-distribution [Gel13, §17.5]. The Student's t-distribution, $t(\mu, \sigma, \nu)$, parametrised by the location μ, the scale parameter $\sigma > 0$ and the shape parameter $\nu > 0$, is bell-shaped, symmetric with respect to μ, and is a generalisation of the normal distribution $\mathrm{Norm}(\mu, \sigma)$, which corresponds to $\nu = +\infty$. Figure 4.3 shows the density of this distribution. The t-distribution has a heavier tail (the smaller ν, the heavier the tail), so it better fits data with outliers. The location parameter is assumed to be $\mu = 0$, which neglects the slight systematic error in the ultrasonic model to prevent overfitting. Assuming furthermore that (i) the model accuracy is independent of the view, that is the error terms are identically distributed, and (ii) the error terms in different views are independent, then the observation vector conditional on the model parameters has for density

$$f(x \mid \xi, \sigma, \nu) = \prod_{k=1}^{n} t(x_k - h_k(\xi), \sigma, \nu) = \prod_{k=1}^{n} \frac{\Gamma\left(\frac{\nu+1}{2}\right)}{\sqrt{\nu\pi}\,\Gamma\left(\frac{\nu}{2}\right)} \left(1 + \frac{(x_k - h_k(\xi))^2}{\nu\sigma^2}\right)^{-\frac{\nu+1}{2}}, \qquad (4.2)$$

where Γ is the gamma function (extension of the factorial function), and k is the view index.

The parameters σ and ν are not of immediate interest for the characterisation (in statistical

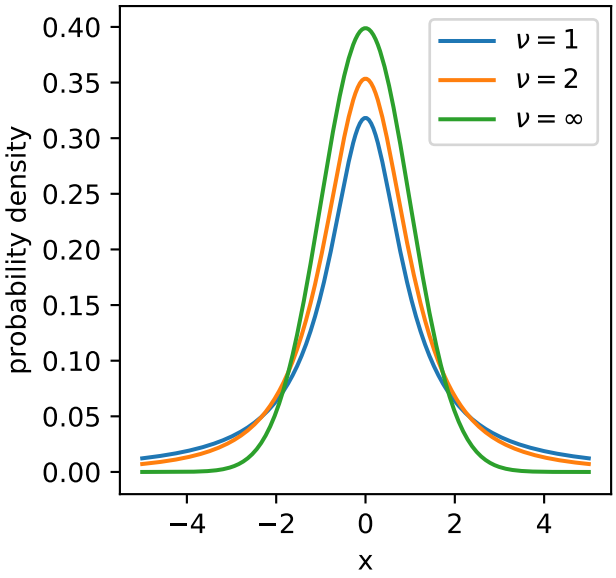

Figure 4.3 – Probability density function of the standard Student's t-distribution for different shape factor ν. The $\nu = \infty$ case coincides with the standard normal distribution. A lower ν makes the tail of the distribution heavier.

terminology, they are described as nuisance parameters) but they must be chosen carefully as they affect the result. They both quantify the confidence in the ultrasonic model. σ is the typical error in dB between the ultrasonic model and the result. A very large σ leads to a flat density $f(x \mid \xi, \sigma, \nu)$, independent of the observation; the characterisation result would be wholly controlled by the prior distribution on ξ, that is in this case that all reference scatterers are equally credible. A zero σ leads to a Dirac distribution: only a single scatterer is credible, all others are not; this point estimation would ignore the uncertainties, so it would give a suboptimal result with excessive confidence. From fig. 4.2, σ is estimated to be around 2 or 3 dB. To account for the uncertainty on this parameter, and to avoid the characterisation result depending strongly on an arbitrarily chosen value, σ is left as a stochastic variable with as prior distribution the normal distribution $f(\sigma) = \mathrm{Norm}(2\,\mathrm{dB}, 0.5\,\mathrm{dB})$. Although σ can technically be negative with such a prior, this case is ignored as it happens with a negligible probability (3×10^{-5}). The parameter ν controls the tail of the t-distribution, and hence the influence of outliers. A large ν leads to a high sensitivity to outliers; a small ν leads to a more robust but more indecisive characterisation. Gelman recommends a value of a few units [Gel13, §17.5]. As for σ, ν could be treated stochastically, at the expense of an increased computational cost. A

fixed value of $\nu = 2$ (fig. 4.3) was adopted as it appears to be sufficient to produce acceptable results.

4.2.5 Posterior distribution

The likelihood $f(x \mid \xi, \sigma, \nu)$ (eq. (4.2)), or $f(x \mid \xi, \sigma)$ as ν is fixed, relates to the forward problem, that is information on plausible observation x given a reference scatterer ξ. The quantity of interest corresponds however to the inverse problem, that is information on a plausible reference scatterer ξ given an observation x; formally, $f(\xi \mid x)$. The inversion is done with Bayes' theorem:

$$f(\xi, \sigma \mid x) = \frac{f(x \mid \xi, \sigma) f(\xi, \sigma)}{f(x)}. \tag{4.3}$$

$f(\xi, \sigma \mid x)$ is called the *posterior* distribution. The posterior distribution can be seen as the prior distribution, $f(\xi, \sigma)$, updated with the information from the observation via the forward model, $f(x \mid \xi, \sigma)$. As the parameters ξ and σ are independent, the prior distribution is $f(\xi, \sigma) = f(\xi) f(\sigma)$; $f(\xi)$ was defined in section 4.2.3, and $f(\sigma)$ in section 4.2.4. $f(x)$ is formally the marginal distribution of the observation; in practice, it acts as a normalisation constant: recalling than the integral of a probability density function is 1, in particular for $f(\xi, \sigma \mid x)$:

$$\int \int_{-\infty}^{+\infty} f(\xi, \sigma \mid x) \, d\xi \, d\sigma = 1, \tag{4.4}$$

then with eq. (4.3)

$$f(x) = \int \int_{-\infty}^{+\infty} f(x \mid \xi, \sigma) f(\xi, \sigma) \, d\xi \, d\sigma. \tag{4.5}$$

Note that the notations $\int d\xi = \iiint dl \, dr \, d\varphi$ for the ellipse and $\int d\xi = \iint dl \, d\varphi$ for the crack are used. The posterior distribution without the nuisance parameter σ is obtained by integrating it out:

$$f(\xi \mid x) = \int_{-\infty}^{+\infty} \frac{f(x \mid \xi, \sigma) f(\xi, \sigma)}{f(x)} \, d\sigma. \tag{4.6}$$

The analysis of this distribution is the core of Bayesian inference, and is the object of the next section.

4.3 Bayesian analysis and inference

This section presents selected techniques for drawing inferences on the defect parameter ξ from the posterior distribution (eq. (4.6)).

4.3.1 Point estimation

The simplest form of inference is to select the single "best" reference scatterer. Different point estimates exist, depending on the definition of "best"

A first option is to maximise the posterior density, which gives the maximum a posteriori (MAP) [Rob07, §4.1.2]

$$\xi_{\text{MAP}} = \arg\max_{\xi} f(\xi \mid x). \tag{4.7}$$

The MAP is a popular choice in machine learning due to its simplicity [Bis06]. A known limit is its dependence on the (arbitrary) parametrisation of the model [Dru07]. As a remark, if σ was fixed, and because the prior on ξ is uniform, so $f(\xi)$ is constant, then

$$\arg\max_{\xi} f(\xi \mid x) = \arg\max_{\xi} \frac{f(x \mid \xi) f(\xi)}{f(x)} = \arg\max_{\xi} f(x \mid \xi), \tag{4.8}$$

the MAP would coincide with the maximum likelihood estimate. Also, if again σ was fixed, and if the error terms were normally distributed ($\nu = +\infty$) rather than t-distributed, then

$$\arg\max_{\xi} f(\xi \mid x) = \arg\max_{\xi} f(x \mid \xi) = \arg\max_{\xi} \prod_{k=1}^{n} \frac{1}{\sqrt{2\pi\sigma^2}} \exp\left(-\frac{(x_k - h_k(\xi))^2}{2\sigma^2}\right) \tag{4.9}$$

$$= \arg\max_{\xi} \exp\left(-\frac{1}{2\sigma^2} \sum_{k=1}^{n} (x_k - h_k(\xi))^2\right) \tag{4.10}$$

$$= \arg\min_{\xi} \sum_{k=1}^{n} (x_k - h_k(\xi))^2, \tag{4.11}$$

so the MAP estimate would coincide with the least-square estimate. The characterisation model with MAP estimation can therefore be seen as a variant of a least-square regression, with increased robustness and accounting for the uncertainty on σ.

A second option is to quantity the cost of choosing $\hat{\xi}$ as a point estimate for ξ via a loss function $L(\xi, \hat{\xi})$ [Rob07, chapter 2]; for example, in 1D, the quadratic loss $L(\xi, \hat{\xi}) = (\xi - \hat{\xi})^2$. In a NDT context, the loss function could factor in the cost of underestimating the severity of a defect (possible component failure) and the cost of overestimating it (unnecessary maintenance). As ξ is stochastic, the loss $L(\xi, \hat{\xi})$ for a fixed $\hat{\xi}$ is stochastic as well. The expected posterior loss is

$$\rho(\hat{\xi}) = \mathrm{E}(L(\xi, \hat{\xi}) \mid x) = \int L(\xi, \hat{\xi}) f(\xi \mid x) d\xi, \tag{4.12}$$

that is the continuous average of the loss function weighted by the posterior density. The value which minimises $\rho(\hat{\xi})$ is called the Bayes estimate associated with the loss function L. For the

quadratic loss $L(\xi, \hat{\xi}) = (\xi - \hat{\xi})^2$, the Bayesian estimator is the posterior mean

$$\bar{\xi} = \mathrm{E}(\xi \mid x) = \int \xi f(\xi \mid x) d\xi. \tag{4.13}$$

For the absolute error loss $L(\xi, \hat{\xi}) = \left|\xi - \hat{\xi}\right|$, the Bayes estimator is the posterior median. In the general case, the closed-form expression may not be known but the estimator can be obtained numerically.

Figure 4.4 illustrates the difference between the MAP, the posterior mean and median for a mixture of two normal distributions. There is a 10% chance that the true parameter comes from the left cluster (area under the curve of 0.1), and 90% it comes from the right cluster (area under the curve of 0.9). The MAP is the left mode: despite the probability of this cluster being low, it is where the density reaches its maximum. The posterior mean and median results are both closer to the right-hand-side mode, because this is where most of the mass is.

A second example of a point estimation with a multimodal distribution is as follows. Consider the degenerate case where there are two possible defects with equal probability: a 0°-inclined crack, and 90°-inclined crack. The posterior median and mean are a 45°-inclined crack, because 45° minimises the error angle between 0° and 90°. However, this is neither of the two plausible defects. The MAP would be either the 90° or the 0° crack, which ignores the second plausible defect. Point estimation cannot therefore convey the full complexity of a multimodal distribution.

4.3.2 Posterior samples

To avoid the issues just described, a simple and very powerful way to visualise the characterisation results in their full complexity is to draw samples from the posterior distribution and plot them. Each sample corresponds to a plausible scatterer. The more plausible the scatterer is, the more likely similar scatterers will be drawn as well. For example, if there are two clusters of plausible scatterers, cluster A with a probability of 80% and cluster B with a probability of 20%, then on average 80% of the posterior samples will come from cluster A and 20% from cluster B. It is essential to draw a large number of samples to ensure the main clusters are well represented.

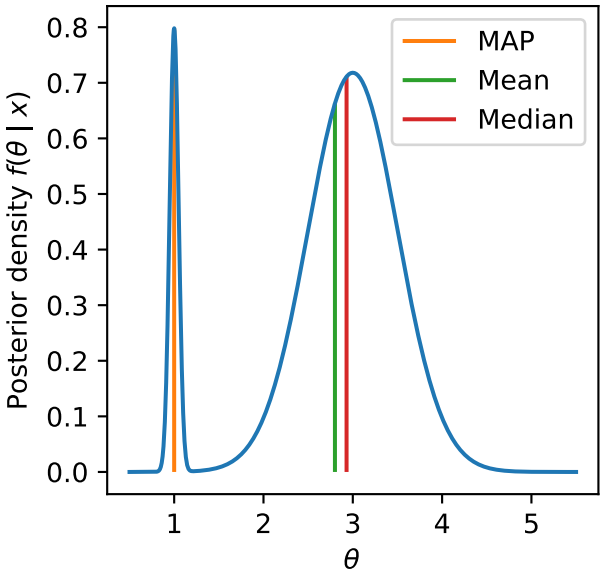

Figure 4.4 – Point estimation for a mixture of two normal distributions. The left mode has the highest density; the right mode corresponds to a larger probability (area under curve).

4.3.3 Visualising the density of the posterior distribution

The density of the posterior distribution, $f(\xi \mid x)$, is a function of ξ, of dimension 3 for the ellipse model, and 2 for the crack model. For visualisation purposes, the dimensionality is reduced by integrating out unwanted dimensions (marginalisation). For example, with $\xi = (l, r, \varphi)$, a 1D distribution is obtained by integration of two dimensions:

$$f(l \mid x) = \iint f(l, r, \varphi \mid x)\, dr\, d\varphi. \tag{4.14}$$

The distribution $f(l \mid x)$ is the distribution of the major length l of the credible scatterers, regardless of their aspect ratio r and their angle φ.

4.3.4 Highest posterior density credible sets

Credible sets are a way to quantify the characterisation: for example, "there is a 99% chance that the defect is (or at least scatters like) a crack between 0.4λ and 0.7λ". Formally, an α-credible set C_α is by definition a set of the parameter space so that the probability of this set under the posterior distribution is α:

$$P(\xi \in C_\alpha \mid x) = \int_{C_\alpha} f(\xi \mid x) d\xi = \alpha. \tag{4.15}$$

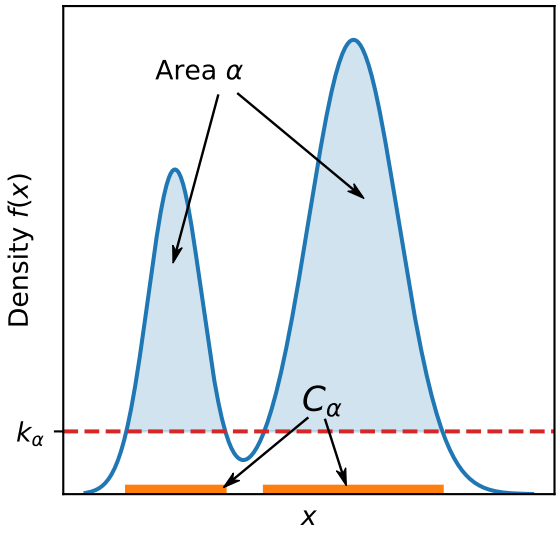

Figure 4.5 – Highest Posterior Density credible set, C_α, of the distribution of density $f(x)$. The total area above the threshold k_α is α.

A credible set is not unique: for a univariate distribution, the interval bounded by the 2.5th and 97.5th percentiles of the posterior distribution is a 95%-credible interval, but so is the interval bounded by the 0th and 95th percentiles.

A Highest Posterior Density (HPD) credible set is a credible set C_α so that there is threshold k_α so that

$$C_\alpha = \{\xi : f(\xi \mid x) \geq k_\alpha\}, \tag{4.16}$$

as illustrated in fig. 4.5. So a HPD set includes as a priority areas of the parameter space with the highest density. Note that eq. (4.16) is not valid if the posterior definition is flat over some intervals, see Robert [Rob07, Def. 5.5.2] for a more general definition. A criticism is that HPD sets depend on the arbitrary model parametrisation, which is undesirable [Dru07]; their simplicity makes them however a valuable tool.

4.3.5 Classification of the defect

Two types of defects are considered, leading to two characterisation models: M_1 for ellipses, and M_2 for cracks, which are run independently. They lead to different results: $\xi_1 \mid x$ under M_1, $\xi_2 \mid x$ under M_2. A solution to determine which model is the most suited is to treat them both as stochastic variables, and to calculate their posterior probability $f(M_i \mid x)$ [Rob07,

§5.2.2][Gel13, §7.4]. Using Bayes' theorem, the ratio of posterior probabilities is

$$K = \frac{f(M_1 \mid x)}{f(M_2 \mid x)} = \frac{f(M_1)}{f(M_2)} B_{12}, \tag{4.17}$$

where B_{12}, called the Bayes factor, is defined as

$$B_{12} = \frac{f(x \mid M_1)}{f(x \mid M_2)}. \tag{4.18}$$

Assuming the two models are as reasonable, their prior probabilities are equal $f(M_1) = f(M_2)$, so K and B_{12} are equal. B_{12} is often used as a more objective proxy for K as it does not depend on the prior on M_1 and M_2. For $i \in \{1, 2\}$, the likelihood term is

$$f(x \mid M_i) = \int f(x, \xi_i \mid M_i)\, d\xi_i = \int f(x \mid \xi_i, M_i) f(\xi_i \mid M_i)\, d\xi_i, \tag{4.19}$$

where $f(x \mid \xi_i, M_i)$ and $f(\xi_i \mid M_i)$ are respectively the likelihood function and the prior distribution defined in section 4.2, with a change of notation to make the model M_i explicit.

The Bayes factor quantifies how much the observation supports M_2 versus M_1. B_{12} is greater than 1 if the data supports M_1 more than M_2; B_{12} is less than 1 if the data support M_2 more than M_2. For example, $B_{12} = 10$ means that it is 10 times more likely the true defect is (or scatters like) an ellipse (M_1) than a crack (M_2). The choice of comparing M_1 against M_2, or M_2 against M_1, is arbitrary as the corresponding Bayes factors are related: $B_{12} = 1/B_{21}$. The following scale in dB ($20 \log_{10}(\cdot)$) is usually used [Kas95]: the evidence for M_1 against M_2 is *not worth more than a bare mention* if B_{12} is between 0 and 10 dB, *substantial* between 10 and 20 dB, *strong* between 20 and 40 dB, *decisive* above 40 dB. Conversely, the scale of evidence for M_2 against M_1 corresponds to opposite dB values: not worth more than a bare mention if B_{12} is between -10 and 0 dB, etc.

The Bayes factor automatically penalises unnecessarily complex models: if the two models fit the observations equally well, it favours the simpler model, which can be seen as an implementation of Ockham's razor [Jef92; Kas95]. The underlying reason is the probability density tends to spread more evenly as the number of model parameters increase, whereas the density of a simpler model remains sharper provided the model is adequate. Complex models always fit the data better than simpler ones because of their increased number of parameters, however this is not necessarily desirable as they also fit better arbitrary data, including meaningless data, which may lead to an erroneous interpretation of their results. Approximating

a crack by an infinitely thin ellipse, the ellipse model can be seen as a generalisation of the crack model; so the ellipse model should theoretically always fit the data at least as well as the crack model. A Bayes factor favouring the crack model, $B_{12} < 0\,\mathrm{dB}$, indicates that the marginally better fit provided by the extra aspect ratio parameter is not worth the increased complexity.

4.4 Numerical implementation

A limitation of Bayesian models is their high computational cost. As seen in section 4.3, Bayesian analysis relies on the integration of the posterior distribution. Except in trivial examples, this must be done numerically as closed-form expressions are not known. This section presents and compares two approaches. Further resources on Bayesian computation can be found in [Rob07, chapter 6] [Rob10] [Hel14, chapter 8] [Gel13, chapter 10] [OHa04, chapter 9]. For a review of recent techniques, see Green et. al [Gre15].

4.4.1 Numerical integration

A first approach is to calculate the integrals using standard numerical integration techniques, such as the rectangle or trapezium rules. These techniques approximate the integrand with a function easier to integrate, typically a piecewise polynomial. The availability of off-the-shelf numerical integration libraries makes this approach easy to implement. The main problem is the so-called *curse of dimensionality*: the computational cost increases exponentially with the numbers of parameters, which leads to an unreasonably large computation time for anything except a small number of parameters. Robert recommends as a rule of thumb to avoid this technique when the number of variables is larger than 4 [Rob07, §6.2.1]. A quick analysis of the memory footprint confirms this guideline: assuming 100 points per dimension and single-precision floating numbers, it takes 0.4 GB to store the whole posterior distribution with 4 variables, but 37 GB with 5 variables, which is more than usually available in desktop computers. There are workarounds to cope with the amount of data, such as storing it on the hard drive instead of memory, or recalculating values multiple times instead of storing them, but this makes the implementation more difficult.

4.4.2 Markov chain Monte Carlo (MCMC)

A second approach is based on the generation of posterior samples. The analysis of these samples replace the analysis of the posterior density. A difficulty specific to sampling the posterior distribution $f(\xi \mid x) = f(x \mid \theta)f(\theta)/f(x)$ is that the normalisation term $f(x)$ is unknown in general, and is difficult to calculate with numerical integration when the parameter space is high-dimensional. Markov chain Monte Carlo (MCMC) methods are a class of algorithms widely used to sample the posterior distribution. These techniques have their roots in the calculation of integrals in physics in the 1950s, and became more widespread with the increase of computational power in the 1990s [Rob11]. A fundamental method is the Metropolis–Hastings algorithm, described here for educational purposes [Gre15]. The objective is to generate a sequence of samples $(\theta_1, \theta_2, \dots)$ from the posterior distribution $f(\theta \mid x)$. First, an arbitrary probability distribution $q(\cdot|\theta)$ (Markov kernel), for example a Gaussian distribution centred around θ, is chosen to simulate a random walk near θ. The initial point θ_0 is arbitrary. At iteration k :

1. Generate a candidate $\theta^* \sim q(\cdot \mid \theta_{k-1})$ (random walk)
2. Calculate the acceptance ratio $\rho = \min\{1, f(\theta^* \mid x)q(\theta_{k-1} \mid \theta^*)/f(\theta_{k-1} \mid x)q(\theta^* \mid \theta_{k-1})\}$
3. Generate $u_k \sim \text{Unif}(0, 1)$
4. If $u_k \leq \rho$, accept the candidate: $\theta_k = \theta^*$. Otherwise, reject the candidate: $\theta_k = \theta_{k-1}$.

This method only needs to know the posterior distribution up a multiplicative term, which bypasses the difficult calculation of $f(x)$. Consecutive samples obtained with the Metropolis-Hastings algorithm are obviously correlated; however, it can be demonstrated that after an initial number of samples (warm-up), the probability density of the accepted samples θ_k is $f(\theta \mid x)$, as desired, and the samples are independent from the intial point θ_0. The essence of this algorithm is that the sequence of samples tends to remain in high density areas: for a symmetric Markov kernel $q(x \mid y) = q(y \mid x)$, if the new candidate θ^* is in a higher density area than θ_{k-1}, it is always accepted. Otherwise, it is accepted with a probability ρ, and rejected with a probability $1 - \rho$, which ensures the density of the sequence is as desired. Adjusting the Markov kernel changes the convergence rate of the sequence.

Other MCMC algorithms exist: notably Gibbs sampling and Hamiltonian Monte Carlo [Gre15]. In practice for the end user, the Bayesian community provides off-the-shelf software libraries containing state-of-the-art and carefully-tuned MCMC samplers: notably Stan [Car17b], PyMC [Sal16] and JAGS [Plu03]. Regardless of the sampler, it is critical to ensure the chain has converged before exploiting the samples; this is usually done by running multiple chains and comparing them [Gel92; Bro98]. Contrary to numerical integration, MCMC sampling is adapted to solve high-dimensional problems. An essential difference is that MCMC sampling is a stochastic technique, whereas numerical integration is deterministic: the former requires monitoring of the convergence of the chain, the latter of the convergence against the integration step size.

4.4.3 Practical comparison

The quantities related to Bayesian analysis presented in section 4.3 were introduced in their integral form, which makes it clear how numerical integration can be used to calculate them. This section illustrates how they can be estimated from the posterior samples, denoted $(\xi_k, \sigma_k)_{k=1..n}$, obtained with MCMC approaches. If the dimension of the problem is too large for numerical integration, only this latter approach is computationally tractable. Reciprocally, it may be interesting to calculate posterior samples using numerical integration to avoid the extra complexity of MCMC.

For an arbitrary function $g(\cdot)$, the expected value $\mathrm{E}(g(\xi) \mid x)$ is

$$\mathrm{E}(g(\xi) \mid x) = \int g(\xi) f(\xi \mid x)\, d\xi. \tag{4.20}$$

This integral can clearly be calculated with numerical integration. Alternatively, this quantity is expressed from the posterior samples thanks to the law of large numbers:

$$\mathrm{E}(g(\xi) \mid x) \approx \frac{1}{n} \sum_{k=1}^{n} g(\xi_k). \tag{4.21}$$

Two applications are the calculation of the posterior mean, with $g(\xi) = x$, and the expected posterior loss $\mathrm{E}(L(\xi, \hat{\xi}) \mid x)$ (section 4.3.1).

The q-quantile can be obtained by solving with respect to $\xi^\star$ (in the univariate case)

$$\int_{-\infty}^{\xi^\star} f(\xi \mid x)\, d\xi = q, \tag{4.22}$$

or simply from the ordered posterior samples: for example, for 100 samples, the 5%-quantile is the fifth smallest sample. An application is the calculation of the posterior median (50%-quantile) mentioned in section 4.3.1.

A density can be estimated from the samples with a histogram, or with Kernel Density Estimation. This applies for the joint posterior, $f(\xi \mid x)$, but also marginals: for example, the density $f(l \mid x)$, previously obtained by integrating out the other components of ξ (eq. (4.14)), can be estimated by taking the histogram of the l-component of the posterior samples.

In the univariate and unimodal case, the HPD set comes down to the shortest interval which contains a given mass, which makes it simple to obtain using the quantile function calculated from either MCMC samples or the probability distribution itself [Che99]. The multivariate and multimodal case, as encountered here, is more computationally expensive. Using numerical integration, the HPD region can be obtained by solving eq. (4.16) for the threshold k_α. Using MCMC samples and density estimation, Hyndman proposes a density quantile approach [Hyn96].

An alternative to MCMC techniques to sample the posterior distribution using numerical integration is the grid approximation [Gel13, p. 76], illustrated here for $f(\xi \mid x) = f(r, l \mid x)$:

1. Calculate the posterior distribution $f(r, l \mid x)$ on a discrete grid (axes r and l)

2. Calculate the marginal $f(l \mid x)$ on a discrete grid with numerical integration, similarly to eq. (4.14)

3. For the k-th sample:

   (a) Draw a sample l_k from the discrete distribution $f(l \mid x)$

   (b) Draw a sample r_k from the discrete distribution $f(r \mid x, l_k) \propto f(r, l_k \mid x)$

   (c) Add a uniform random jitter centred at zero with a width of the grid step to l_k and r_k to simulate a continuous distribution

This method is simpler to implement and use than MCMC, as it avoids the delicate monitoring of the convergence of the chain.

4.4.4 Chosen implementation

Two implementations of the characterisation model were made, the first one with numerical integration (rectangle rule and Simpson's rule), and the second one with the No-U-Turn MCMC sampler (Hamiltonian Monte Carlo) [Hof14]. Both approaches gave consistent results. However, the MCMC approach was found to be less practical because the chains converge slowly (more than minutes) compared to the runtime of the numerical integration implementation (around 10 seconds). The underlying reason is the presence of multiple disconnected modes in the posterior distribution, which makes its exploration with MCMC difficult. A possible solution, left untested, would be to switch to a MCMC sampler designed for multimodal distributions, such as the Wormhole Hamiltonian Monte Carlo algorithm [Lan14]. An additional difficulty is that the number of samples required for convergence is highly dependent on the dataset, so an *ad hoc* convergence analysis is always necessary. For these reasons, only the numerical integration implementation was kept. Its runtime (excluding the ultrasonic forward model) is typically around 15 seconds on a desktop computer with the ellipse model, and around 5 seconds with the crack model. The current bottleneck of this characterisation technique is the calculation of the scattering matrices (approximatively 1 hour) and the forward model (approximately 20 minutes); there is however room for code optimisation.

4.5 Results

Having described the characterisation framework, its performance is demonstrated in this section on the SDH, notch and crack datasets described in table 3.1. The Bayesian analysis is done by drawing posterior samples, and calculating point estimates, HPD credible sets, and Bayes factor to classify the defect.

4.5.1 SDH

The characterisation results for the SDH using ellipses are presented in fig. 4.6 as marginal densities, and fig. 4.7 as point estimates and samples. There are two main clusters, visible in the posterior samples (fig. 4.7b) and the 2D marginal distribution (fig. 4.6d): the first one, near the posterior mean and median, is close to the true defect boundaries; the second one, near the MAP, corresponds to a larger and more oblong defect. The uncertainty on the angle

is high (only 8 degrees are not in the 99% HPD), which is not surprising as the true defect is axisymmetric. The characterised aspect ratio is between 0.6 and 1.0, which includes the true value (1.0). The characterised major length is between 0.2λ and 0.7λ (except a 0.04λ-large region), which includes the true value (0.4λ).

Thin ellipses are unlikely, which supports the hypothesis that the true defect is volumetric. To confirm this, the characterisation model using cracks is run. The resulting Bayes factor (eq. (4.18)) is $B_{12} = 139.9\,\mathrm{dB}$, which corresponds to decisive evidence for the ellipse model against the crack model.

4.5.2 Crack

The characterisation results for the crack using ellipses are presented in fig. 4.8 as marginal densities, and fig. 4.9 as point estimates and samples. The posterior distribution has a single mode, which includes the true value. A precision of 0.14λ for the major length, and 9.9° for the angle, is achieved. The aspect ratio marginal peaks at the lower bound (0.1), which suggests that the defect has a narrower aspect ratio as 0.1. An aspect ratio below 0.1 seems credible, but a proper investigation would require to run the model with thinner ellipses, which is difficult due to meshing issue in the finite-element simulation.

The characterisation model using cracks is run to complete the analysis. Its marginals are shown in fig. 4.10, and the samples in fig. 4.11. The results are comparable with the ellipse model (without the aspect ratio): a single mode near the true values. The crack model slightly underestimates the major length; the MAP is 10% under the true value. A Bayes factor of $B_{12} = -32.8\,\mathrm{dB}$ is obtained, which is a strong evidence for the crack model. This does not guarantee the true defect is a crack; strictly speaking, this Bayes factor only suggests the aspect ratio variable of the ellipse model is an unnecessary complication to explain the observed TFM amplitudes. It does not exclude that the true defect may be an ellipse thinner than investigated in the ellipse model. However, engineering prudence dictates interpreting the results as the worst case scenario, i.e. that the true defect is a crack.

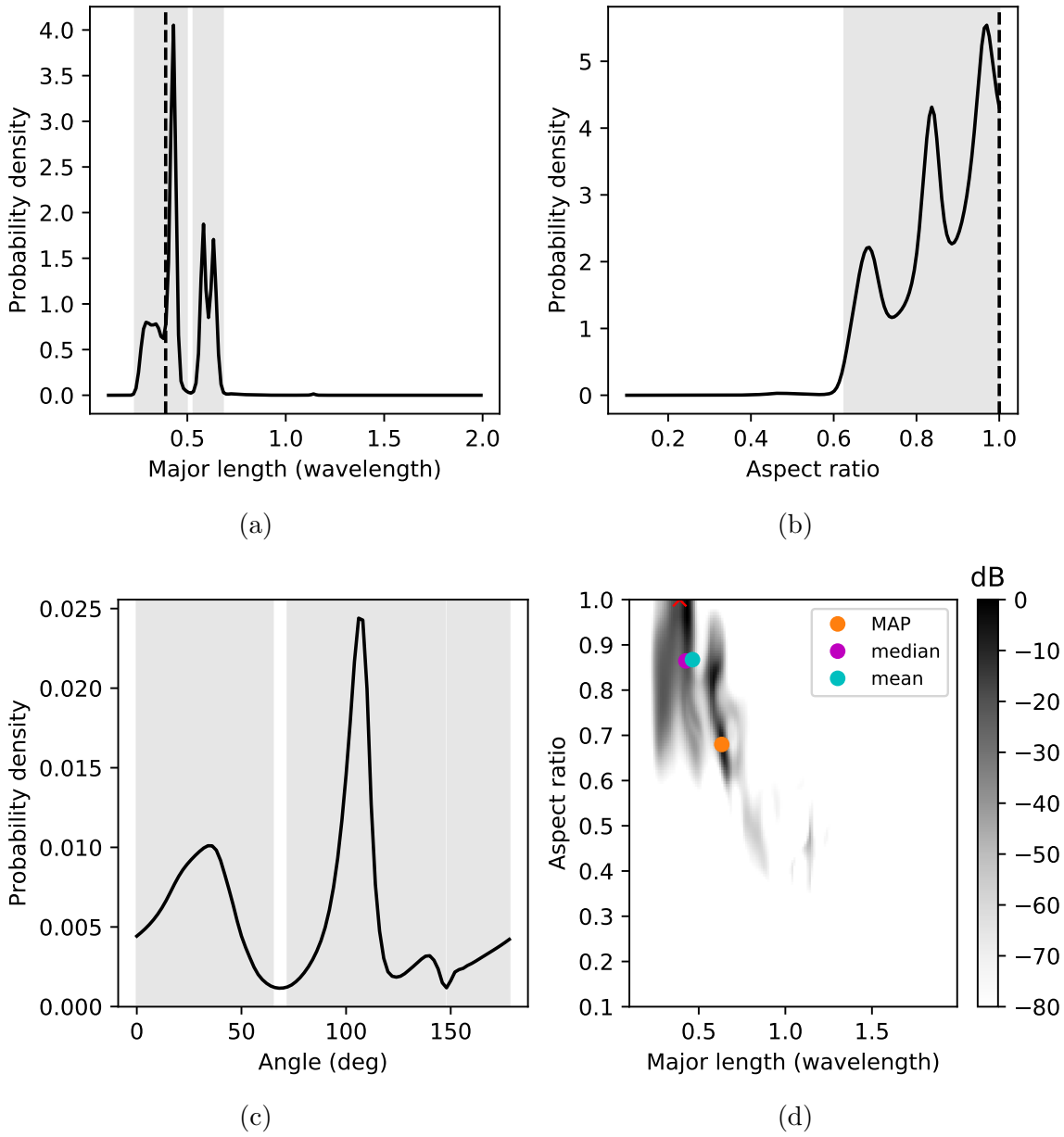

Figure 4.6 – Probability density of the marginals of the posterior distribution for the characterisation of a SDH with ellipses. The 99% HPD regions are shown in light grey in (a), (b), (c). The dash lines and the red cross correspond to the true defect. Point estimates are shown in (d).

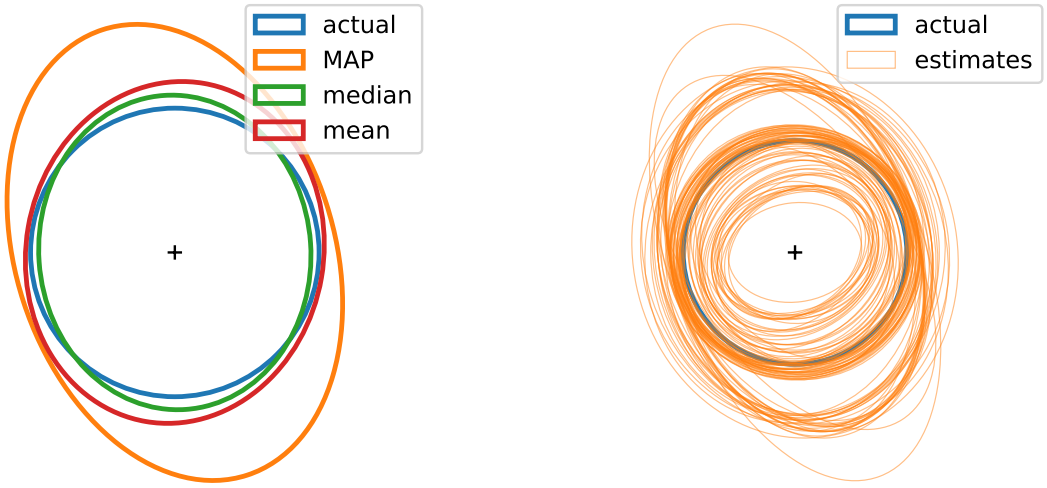

(a) (b)

Figure 4.7 – Characterisation of the SDH using ellipses. (a) Point estimates. (b) 100 posterior samples.

4.5.3 Notch

The characterisation results for the notch using ellipses are presented in fig. 4.12 as marginal densities, and fig. 4.13 as point estimates and samples. The true defect is a vertical (90°) rectangular notch of dimensions $1.2 \times 0.4\lambda$ (0.33 aspect ratio). The posterior distribution presents multiple clusters and large uncertainties. A first cluster corresponds to a small ($\approx 0.3\lambda$) horizontal (0°) ellipse, which may be explained by the scattering of the upper and lower part of the notch. The other credible ellipses match more closely the true dimensions and orientation of the notch. In particular, the MAP is an ellipse of major length 1.1λ, which is a 7% relative error compared to the notch. The HPD of the major length ranges from 0.2λ to 2.0λ (measure of 1.1λ after removing the gaps), which is close to the full range studied. Also, its density increases near the upper bound (2.0λ), which was chosen as the validity limit of the ultrasonic model (point-like assumption). This is problematic as it indicates the characterisation depends on the arbitrary chosen upper bound, so the sizing results are questionable. This could show a fundamental limitation of this characterisation approach to size larger defects, and/or this could be caused by the degradation of the accuracy of the ultrasonic forward model, which is only valid for small defects. Despite these limitations, the characterisation model gives a reasonable idea of the orientation and aspect ratio of the defect, without providing undue

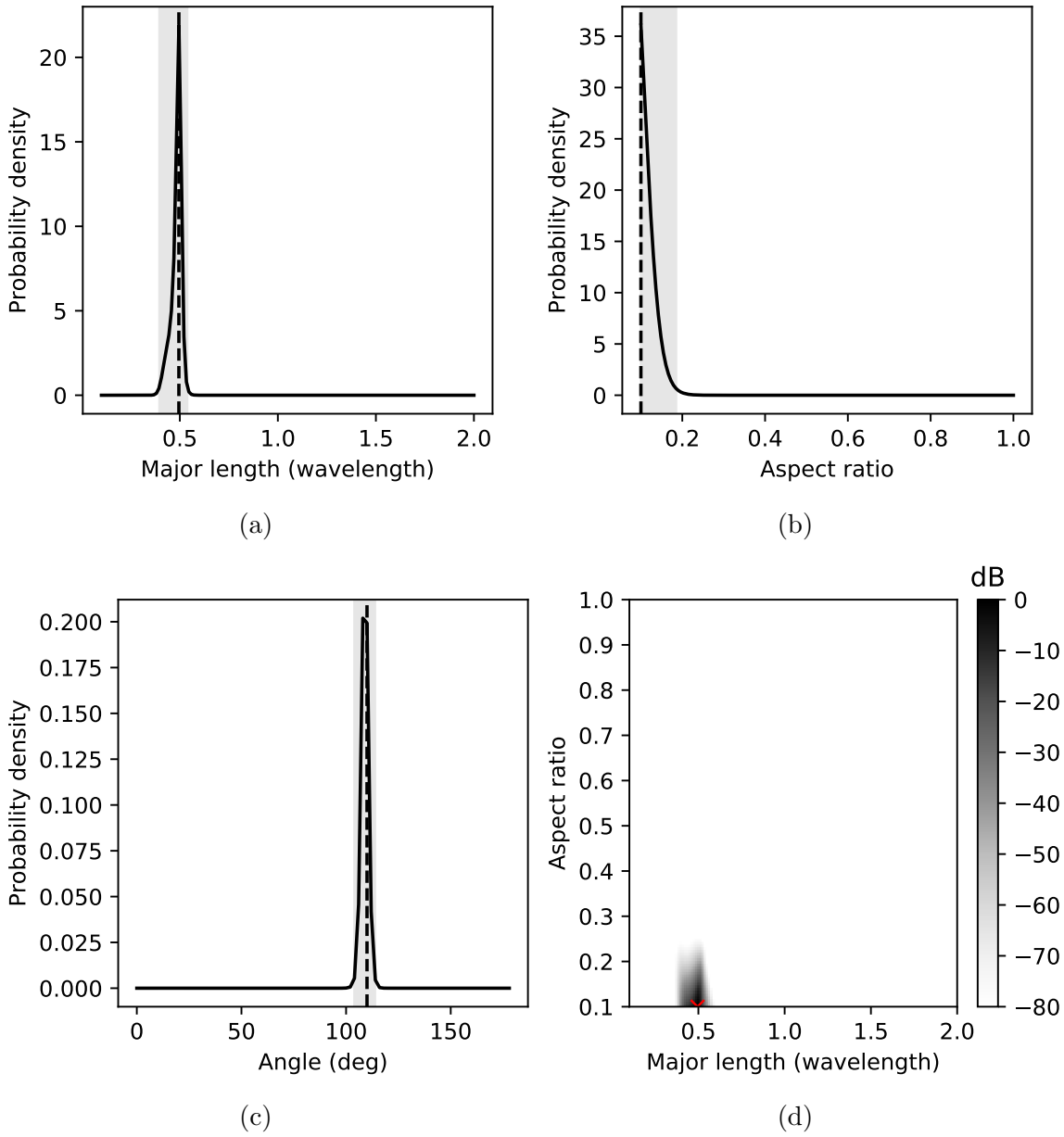

Figure 4.8 – Probability density of the marginals of the posterior distribution for the characterisation of a crack with ellipses. The 99% HPD regions are shown in light grey in (a), (b), (c). The dash lines and the red cross correspond to an ellipse with similar size and orientation as the true defect, and the minimum investigated aspect ratio.

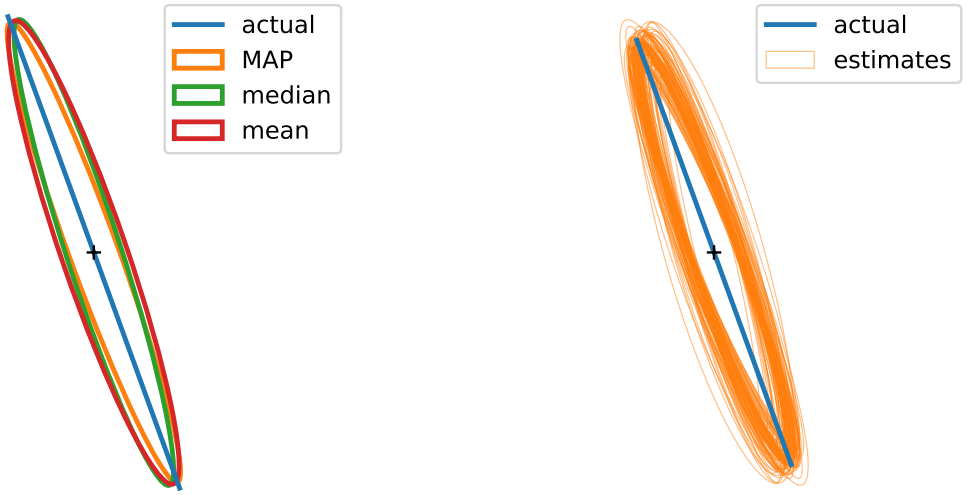

(a) (b)

Figure 4.9 – Characterisation of the crack using ellipses. (a) Point estimates. (b) 100 posterior samples.

certainty. The Bayes factor $B_{12} = 35.5\,\text{dB}$ confirms the data strongly supports the ellipse model against the crack model, so the defect is volumetric.

4.6 Conclusion

A Bayesian model was introduced to characterise a defect by comparing its signature against reference ellipses and cracks. The experimental validation was done for a crack, a SDH, and a rectangular notch. The characterisation is reasonably good, although the precision is variable: a precision of 0.14λ was obtained in the best case, 1.1λ in the worst case. The inherent uncertainty on the length, aspect ratio and angle of the defect is visualised and quantified with the posterior samples, the marginal densities and the HPD regions. This is especially important for the SDH and the notch, where several clusters of solutions exist. Point estimates are also obtained, although they convey less information and may be deceiving. The Bayes factor between the ellipse model and the crack model was used to classify a defect as volumetric or crack-like. The crack defect was however well approximated by a thin ellipse.

The main limit is that this characterisation technique was only tested on embedded smooth 2D defects. It could be extended to more realistic cases (3D rough defects), under the condition

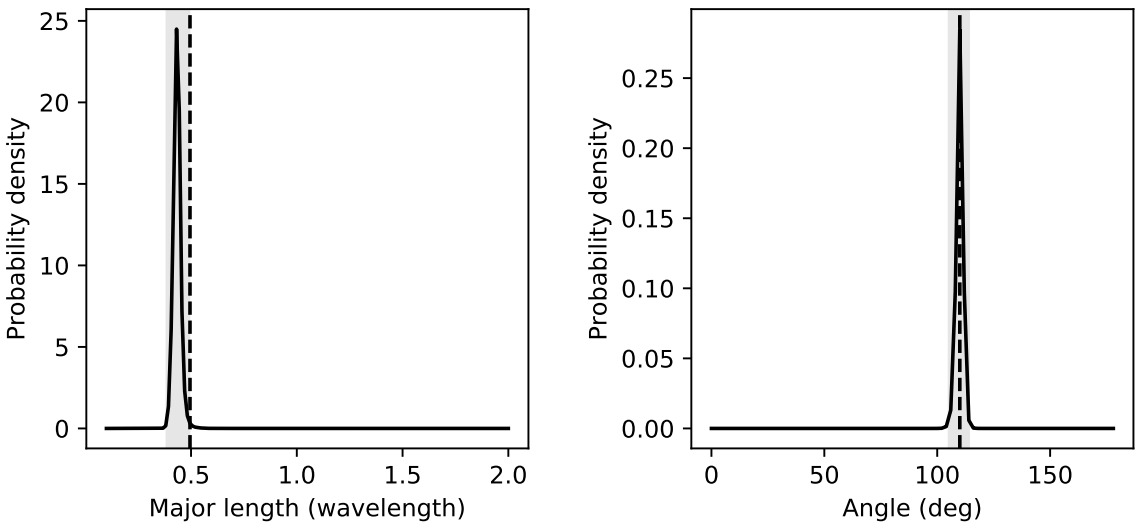

(a) (b)

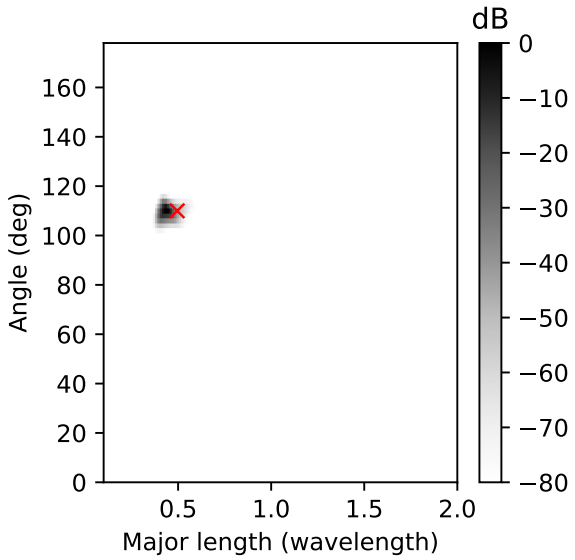

(c)

Figure 4.10 – Probability density of the marginals of the posterior distribution for the characterisation of a crack using cracks. The 99% HPD regions are shown in light grey in (a) and (b). The dash lines and the red cross correspond to the true defect.

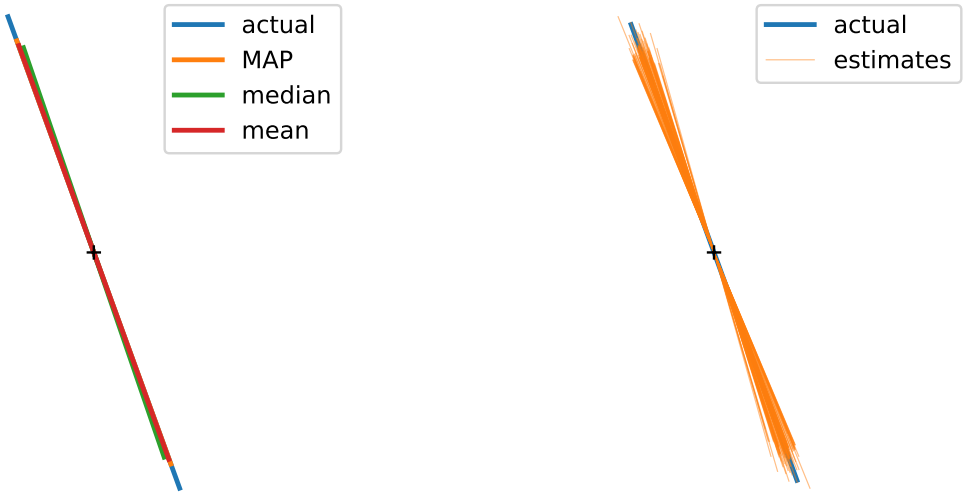

(a) (b)

Figure 4.11 – Characterisation of the crack using cracks. (a) Point estimates. (b) 100 posterior samples.

that a suitable ultrasonic model is available. Adding more variables would however require switching from the numerical implementation to the MCMC implementation, due to the high computational burden in high dimensions. A second limit is that the assumption that the measured TFM amplitude is the defect response plus-minus a noise term (eq. (4.1)) breaks down if the image signal-to-noise ratio (SNR) is low: if the structural noise is larger than the signal, the measured value is in reality the noise floor. A workaround is to exclude TFM images with low SNR from the characterisation. A more systematic solution is to somehow include the structural noise level in the uncertainty model, possibly as an additive term in linear scale. A starting point to do so is to probabilistically model the structural noise in a TFM image, which is the subject of the next chapter.

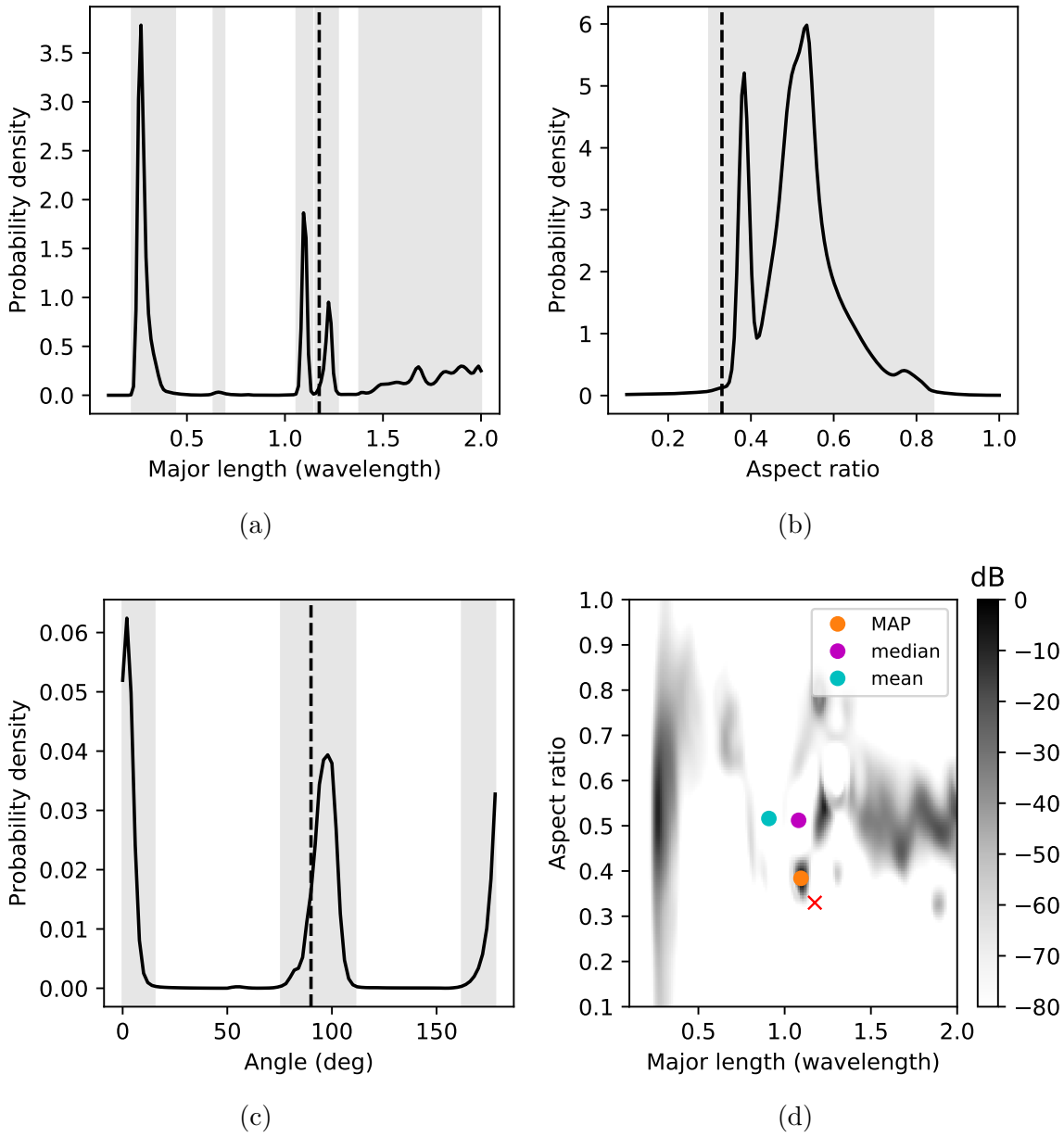

Figure 4.12 – Probability density of the marginals of the posterior distribution for the characterisation of a notch with ellipses. The 99% HPD regions are shown in light grey in (a), (b), (c). The dash lines and the red cross correspond to an ellipse with the same major length and aspect ratio as the notch. Point estimates are shown in (d).

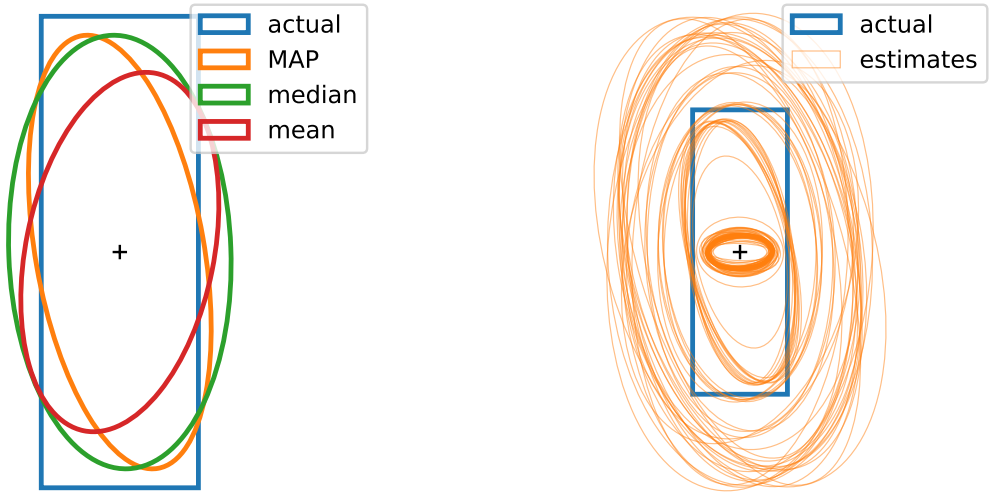

(a) (b)

Figure 4.13 – Characterisation of the notch using ellipses. (a) Point estimates. (b) 100 posterior samples.

Chapter 5

Statistics of the noise speckle

5.1 Introduction

In ultrasonic testing, the peak amplitude of the envelope of the A-scan or the image is an essential metric for analysing the response. Typically, this peak amplitude is compared against an evaluation threshold to classify the response as a defect or noise [AST14]. The threshold may be set based on the minimum acceptable defect size, using a calibration block or modelling. Under this approach, an indication is classified as a defect if its response is similar to reference defects. A different route consists in classifying an indication as a defect if it is *not* similar to the noise, by setting the evaluation threshold somewhat above the noise floor, or equivalently, defining a Signal to Noise Ratio (SNR) threshold. The choice of the threshold is critical: too low, actual noise will likely exceed it, which produces false alarms; too high, an actual defect may remain underneath, which produces a miss. Probabilistic modelling of the noise and the defect helps to quantify the performance of the classifier and to define a suitable threshold [Oli96; Ogi93]. For example, setting the threshold to the 99% quantile of the probability distribution of the noise response produces theoretically a probability of false alarm of 1%. The critical part is to accurately model the probability distribution of the peak amplitude of the noise and the defect; this is relatively easy for a single pixel or A-scan time point, but significantly more challenging for an image region or time window because consecutive pixels/time points are correlated due to the finite width of the ultrasonic toneburst.

The grain noise (or structural noise), which results from the interaction of the elastic waves and the microstructure of the sample, is the main practical concern for detectability [Wil13].

In an ultrasonic image, it manifests itself as speckle. Thorough statistical investigations of the speckle were done by Goodman in laser optics [Goo75], and Wagner, Smith et al. in medical ultrasound B-scans [Wag83; Smi83; Wag87]. They showed that when the material microstructure is much finer than the point spread function, the speckle amplitude (modulus of the complex amplitude) is accurately modelled by a Rayleigh distribution, parametrised by σ, and the speckle can be approximated to some extent as a collection of n_{eff} independent speckle cells, n_{eff} being calling the effective sample size. As the speckle is spatially correlated, part of the information in a measurement is redundant; the effective sample size quantifies the amount of independent information. These authors did not address the question of peak amplitude over an area. The ultrasonic testing literature on this topic is scarce. The only relevant paper that was found is from Margetan et al. [Mar96], who studied the peak amplitude over a gate in an A-scan: the signal is also modelled as a collection of independent segments of identical length, and a good experimental agreement is achieved. The segment length, which can be seen as the fraction of the length of the gate by the effective sample size, is however left as an adjustable parameter, and no method is given to determine it, which is one of the questions explored in this chapter.

This chapter focuses on the probability distribution of the peak amplitude of the speckle in an ultrasonic image. Theoretical results on the origins and the statistics of the speckle are recalled. Several estimators of σ and n_{eff} are introduced and compared. Results obtained on numerically generated speckle are presented.

The code to generate the results presented in this chapter is available at `https://github.com/nbud/speckle_properties`.

5.2 Theoretical background

5.2.1 Origin of the speckle

The origin of the speckle is the superposition of coherent waves with uniformly distributed phases; the speckle is the resulting interference pattern [Goo75]. For example in optics, the reflection of a laser beam against a rough surface is modelled as a superposition of rays arising from each point of the surface; as the travelled distances to an observation point are slightly different for each ray, the rays are out of phase so their superposition produces an interference

pattern. In ultrasonic testing, the incident elastic wave is scattered by the microstructure of the material: the superposition of these grain scattering events produces a backscattered wave, which manifests as speckle on the image [Yal96; Wag83]. Also, in optics as in ultrasonics, the imaging system itself is a source of speckle: such a system is diffraction-limited, i.e. its Point Spread Function (PSF) is finite, so multiple sources in the imaged object contribute to the same image point; as the distances between the image point and the sources vary, the contributing waves are out of phase, which produces a speckle pattern in the image. The speckle in an ultrasonic image depends therefore on the material microstructure texture and the PSF; in the limit case where the texture is much finer than the PSF, that is that there are numerous grains in a resolution cell, the speckle depends only on the PSF [Wag83]. This chapter focuses mainly on the latter case; the reader is referred to Goodman [Goo75] for a more general treatment.

5.2.2 Distribution of the speckle amplitude

In an ultrasonic image, consider the complex-valued speckle amplitude A obtained by the summation of N grain scattering events. Each grain response is supposed to have the same magnitude $\sigma/\sqrt{N}$, which is reasonable for a material with approximately uniformly sized grains, and a uniformly distributed phase. Supposing the number of contributing grains is large, that is the microstructure is fine, then by the central limit theorem, the summation is asymptotically normally distributed, that is its probability density function (PDF) is for large N [Goo75]

$$f(A) = \frac{1}{2\pi\sigma^2} \exp\left(-\frac{\mathrm{Re}(A)^2 + \mathrm{Im}(A)^2}{2\sigma^2}\right), \tag{5.1}$$

where $\mathrm{Re}(\cdot)$ and $\mathrm{Im}(\cdot)$ denote the real and imaginary parts. The real part and the imaginary parts of A have zero means, the same variance σ^2 and are uncorrelated. As a consequence, it can be demonstrated that the speckle amplitude $I = |A|$ follows the Rayleigh distribution with the scale parameter σ, denoted Rayleigh(σ), of density

$$f(I) = \frac{1}{\pi\sigma^2} \exp\left(-\frac{I^2}{2\sigma^2}\right). \tag{5.2}$$

A refresher on the scale parameter is provided in appendix D.3. The good agreement of the speckle distribution with this model has been experimentally demonstrated on medical B-scans [Bur78; Wag83] and on TFM images [Bev18]. Selected properties of the Rayleigh distribution

are presented in table 5.1. As a remark, the K-distribution can be used in lieu of the Rayleigh distribution if the number of contributing grains is small [Mar96; Jak76].

Table 5.1 – Rayleigh distribution with scale $\sigma > 0$, defined for $x \geq 0$

PDF	$f(x) = \frac{x}{\sigma^2} \exp\left(-\frac{x^2}{2\sigma^2}\right)$
CDF	$F(x) = 1 - \exp\left(-\frac{x^2}{2\sigma^2}\right)$
Mean	$\mathrm{E}(X) = \sigma\sqrt{\frac{\pi}{2}} \approx 1.25\sigma$
Mode	σ
Root mean square	$\sqrt{\mathrm{E}(X^2)} = \sqrt{2\sigma^2} \approx 1.41\sigma$
Standard deviation	$\sqrt{\mathrm{Var}(X)} = \sqrt{\frac{4-\pi}{2}}\sigma \approx 0.66\sigma$
Quantile q	$\sigma\sqrt{-2\log(1-q)}$

5.2.3 Distribution of the peak response of independent and identically distributed pixels

In ultrasonic testing, the SNR is defined as the peak amplitude of the defect signal divided Root Mean Square (RMS) of the noise speckle, $\sqrt{\mathrm{E}(I^2)}$, where $I = |A|$ is the modulus of the complex amplitude. In the absence of a defect, or when the defect signal is much weaker than the noise speckle, the measured SNR is the peak amplitude of the *speckle* divided by its RMS; this quantity is hereafter referred to as the *normalised peak amplitude*. This section studies the probability distribution of this quantity for a single monitored pixel, and a set of independent and identically distributed (i.i.d.) pixels. It is assumed that the true value of the RMS is known; how to estimate it in practice is not addressed.

5.2.3.1 Single pixel

The normalised peak amplitude at a single speckle pixel of Rayleigh(σ)-distributed amplitude I is simply $I/\mathrm{RMS} = I/\sqrt{2\sigma^2}$, which is a Rayleigh($1/\sqrt{2}$) distribution. As a consequence, in the absence of a defect, the expected value is $E(I/\mathrm{RMS}) = \sqrt{\pi/4} \approx 0.88 \approx -1.0$ dB and 99% of the normalised peak amplitudes are under $\sqrt{-\log(0.01)} \approx 2.15 \approx 6.6$ dB.

5.2.3.2 n i.i.d. pixels

In practice, the location of potential defects is not known *a priori* so a region of an image must be monitored rather than a pixel. Although the speckle is spatially correlated, so neighbouring pixels are not independent, it is educational to first consider the peak response of several i.i.d. speckle pixels.

Consider n i.i.d. speckle amplitudes, denoted $I_1, \dots, I_n$, of identical cumulative distribution function (CDF) $F(x)$ and PDF $f(x)$. Recall the cumulative function of the distribution of the random vector $(I_1, \dots, I_n)$, that is the speckle amplitudes considered collectively, is by definition

$$F_{I_1,\dots,I_n}(x_1, \dots, x_n) = P(I_1 \leq x_1, \dots, I_n \leq x_n). \tag{5.3}$$

Because $I_1, \dots, I_n$ are assumed to be independent,

$$F_{I_1,\dots,I_n}(x_1, \dots, x_n) = \prod_{i=1}^{k} P(I_k \leq x_k) = \prod_{i=1}^{k} F(x_k) \tag{5.4}$$

The maximum of $I_1, \dots, I_n$ (peak response) is denoted M_n. Its CDF, $F_{M_n}(x)$, is [Col01]

$$F_{M_n}(x) = P(M_n \leq x) = P(I_1 \leq x, \dots, I_n \leq x) = F_{I_1,\dots,I_n}(x, \dots, x) = F(x)^n. \tag{5.5}$$

The density of M_n is obtained by differentiation: $f_{M_n}(x) = nf(x)F(x)^{n-1}$. In particular, the distribution of the maximum of n independent Rayleigh(σ)-distributed speckle amplitudes is for $x \geq 0$

$$F_{M_n}(x) = \left(1 - \exp\left(-\frac{x^2}{2\sigma^2}\right)\right)^n \tag{5.6}$$

$$f_{M_n}(x) = n\frac{x}{\sigma^2}\exp\left(-\frac{x^2}{2\sigma^2}\right)\left(1 - \exp\left(-\frac{x^2}{2\sigma^2}\right)\right)^{n-1}. \tag{5.7}$$

This distribution is hereafter referred to as the MaxRayleigh(n, σ) distribution. The quantile q of M_n is $\sigma\sqrt{-2\log\left(1 - q^{1/n}\right)}$. The distribution of the normalised peak amplitude, $M_n/\sqrt{2\sigma^2}$, is the same as M_n up to a scaling: MaxRayleigh($n, 1/\sqrt{2}$). Figure 5.1 illustrates this distribution for various n. 99% of the normalised peak amplitudes are below 6.6 dB for $n = 1$, 8.4 dB for $n = 10$, 9.6 dB for $n = 100$, 10.6 dB for $n = 100$. The expected value of the peak response is therefore an increasing function of the number of pixels monitored, so it is essential to account for it. In comparison, the mean amplitude of the speckle, $\mu_n = 1/n \sum_1^n I_n$, which is a metric used notably in medical ultrasound imaging, has a simpler behaviour. Its expected value

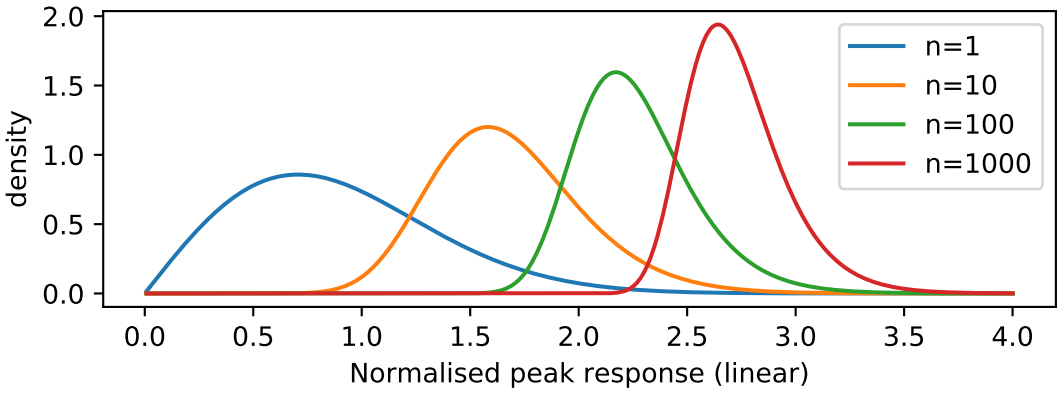

Figure 5.1 – Distribution of the SNR (linear scale) of n i.i.d. speckle amplitudes (MaxRayleigh).

$\mathrm{E}(\mu_n) = \mathrm{E}(I_1)$ does not depend on n; however, its variance does as by the Bienaymé formula, $\mathrm{Var}(\mu_n) = \mathrm{Var}(I_1)/n$.

5.2.3.3 Asymptotic of the peak amplitudes of n i.i.d. pixels

The extreme value theory is a branch of statistics focusing on modelling the extrema of probability distribution [Lea83; Col01; De 07]. In particular, it provides asymptotic results ($n \to +\infty$) on the distribution of $M_n = \max(I_1, \ldots, I_n)$ considered previously. Studying this limit case may seem of a limited interest as the exact distribution of M_n when I_k is Rayleigh-distributed was already obtained in the last section; however, the results presented here will be useful for the study of the correlated speckle later on.

A fundamental result of the extreme value theory is the extremal types theorem [Col01, theorem 3.1], which states the following. Let $\hat{M}_n = \max(\xi_1, \ldots, \xi_n)$, where ξ_k are i.i.d. random variables. If there exists two sequences of constants $\{a_n > 0\}$ and $\{b_n\}$ such that

$$\lim_{n \to +\infty} P\left(\frac{\hat{M}_n - b_n}{a_n} \leq z\right) = G(z), \tag{5.8}$$

where G is a non-degenerate distribution function, then G belongs to one of three families of distribution: the Gumbel distribution (type I), the Fréchet distribution (type II) and the Weibull distribution (type III). Loosely stated, type I corresponds to the case where ξ_k has a thin tail, type II to a heavy tail, type III to a tail with finite upper bound; see Leadbetter [Lea83, §1.6] for a rigorous treatment.

Denoting the CDF of ξ_k as $F(x)$, a sufficient condition for $\hat{M}_n$ to have the Gumbel law

Table 5.2 – Gumbel distribution with location μ and scale $s > 0$, defined for any x. $\gamma \approx 0.577$ is the Euler-Mascheroni constant.

PDF	$f(x) = \frac{1}{s} \exp\left[-\frac{x-\mu}{s} - \exp\left(-\frac{x-\mu}{s}\right)\right]$
CDF	$F(x) = \exp\left[-\exp\left(-\frac{x-\mu}{s}\right)\right]$
Mean	$\mathrm{E}(X) = \mu + s\gamma$
Mode	μ
Standard deviation	$\pi s/\sqrt{6}$

(type I) as limit distribution is [Von36][Dav03, theorem 10.5.2]

$$\lim_{x \to F^{-1}(1)} \left(\frac{d}{dx} \frac{1 - F(x)}{f(x)} \right) = 0. \tag{5.9}$$

For the Rayleigh(σ) distribution, where $F^{-1}(1) = +\infty$,

$$\frac{d}{dx} \frac{1 - F(x)}{f(x)} = \frac{d}{dx} \frac{\exp\left(-\frac{x^2}{2\sigma^2}\right)}{\frac{x}{\sigma^2} \exp\left(-\frac{x^2}{2\sigma^2}\right)} = \frac{d}{dx} \frac{\sigma^2}{x} = -\frac{\sigma^2}{x^2} \xrightarrow[x \to +\infty]{} 0, \tag{5.10}$$

so $(M_n - b_n)/a_n$ tends to the standard Gumbel distribution with

$$b_n = F^{-1}\left(1 - \frac{1}{n}\right) = \sigma\sqrt{2 \log n}, \tag{5.11}$$

$$a_n = \frac{1 - F(b_n)}{f(b_n)} = \frac{\sigma}{\sqrt{2 \log n}}. \tag{5.12}$$

So M_n tends to the Gumbel distribution with scale a_n and location b_n; its properties are presented in table 5.2. The SNR is M_n rescaled by $\sqrt{2\sigma^2}$, so the SNR tends to the Gumbel distribution with location $\sqrt{\log n}$ and scale $1/(2\sqrt{\log n})$, as illustrated in fig. 5.2. The location parameter, which coincides with the mode of the distribution, has a sub-logarithmic growth, which is very slow. As a consequence, an estimation error of n only causes a relatively small error on the prediction of the peak response.

5.2.4 Distribution of the peak response of spatially correlated speckle

Due to the finite size of the grains and the PSF, the speckle pattern is spatially correlated. As before, the distribution of the speckle amplitude I_k is Rayleigh(σ), of CDF $F(x)$. In the i.i.d. case (previous section), the distribution of the random vector $(I_1, \ldots, I_n)$, is known (eq. (5.4)).

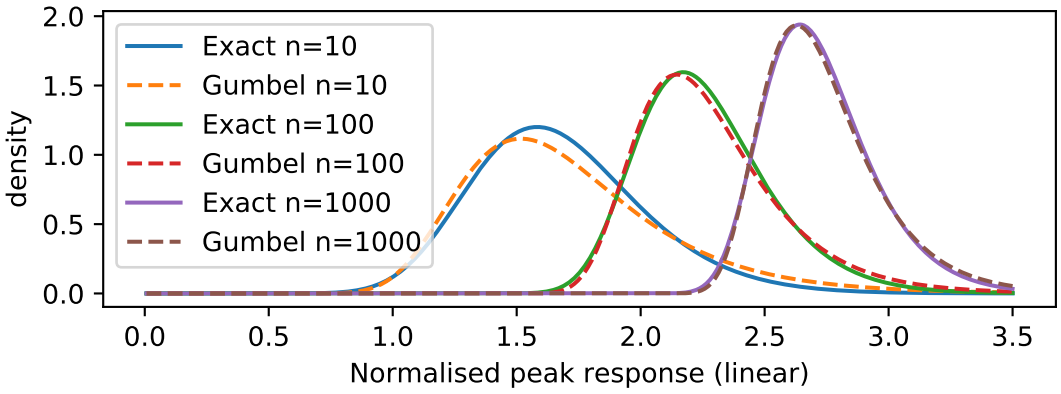

Figure 5.2 – Comparison of the exact (MaxRayleigh) and asymptotic (Gumbel) distributions of the SNR (linear scale) of n i.i.d. speckle amplitudes.

However, this distribution is unknown when the speckle amplitudes are correlated. This makes the calculation of the distribution of a statistic integrated over an area significantly more difficult.

5.2.4.1 The effective sample size approach

It is instructive to consider first the distribution of the average speckle amplitude over a measurement area $\mathcal{S}$

$$I_{\mathcal{S}} = \frac{1}{\mathcal{S}} \iint_{\mathcal{S}} I(x,z)\, dx\, dz, \tag{5.13}$$

where $I(x,z)$ is the Rayleigh(σ) distributed speckle amplitude. The expected value of $I_{\mathcal{S}}$ is simply

$$\mathrm{E}(I_{\mathcal{S}}) = \frac{1}{\mathcal{S}} \iint_{\mathcal{S}} \mathrm{E}(I(x,z))\, dx\, dz = \mathrm{E}(I) = \sigma\sqrt{\frac{\pi}{2}}, \tag{5.14}$$

as $\mathrm{E}(I(x,z)) = E(I)$ is independent of x and y. The speckle cell area $\mathcal{S}_c$ is defined as [Wag83, eq.31]

$$\mathcal{S}_c = \iint_{-\infty}^{\infty} \frac{C_I^2(\Delta x, \Delta y)}{C_I^2(0,0)}\, d\Delta x\, d\Delta y, \tag{5.15}$$

where $C_{I^2}(\Delta x, \Delta y)$ is the autocorrelation function of the centred speckle intensity $\bar{I}^2 = I^2 - \mathrm{E}(I^2)$. The variance of $I_{\mathcal{S}}$ is [Smi83][Goo75, §2.6]

$$\mathrm{Var}(I_{\mathcal{S}}) = \frac{\mathrm{Var}(I)}{n_{\mathrm{eff}}} = \frac{(4-\pi)\sigma^2}{2n_{\mathrm{eff}}}, \tag{5.16}$$

with $n_{\mathrm{eff}} \approx \mathcal{S}/\mathcal{S}_c$ if the measurement area contains a large number of cells ($\mathcal{S}_c \ll \mathcal{S}$), and $n_{\mathrm{eff}} = 1$ if the opposite limit case ($\mathcal{S}_c \gg \mathcal{S}$). When $\mathcal{S}_c \ll \mathcal{S}$, n_{eff} is interpreted as the number

of speckle cells in the measurement area.

Recalling that the variance of n i.i.d. variables is $\mathrm{Var}(I)/n$, it is tempting to interpret n_{eff} in eq. (5.16) as an equivalent number of i.i.d. speckle amplitudes, i.e. an effective sample size. This is consistent with the intuition that because the correlation between two points in the speckle decreases as the distance between them increases, these points can be considered independent after a certain distance governed by the speckle cell size. This speckle cell size is governed by the material microstructure and the PSF. The main caveat is that this number n_{eff} is only valid for the statistic $I_{\mathcal{S}}$: there is no theoretical guarantee that there is such a number for the case of interest here, the peak amplitude in the measurement area $\mathcal{S}$, and that this number if it exists would equal the effective sample size derived for $I_{\mathcal{S}}$. An experimental attempt to determine an effective sample size for the peak response is presented later in this chapter.

5.2.4.2 The extremal index approach

A second avenue to explore comes from the extreme value theory. The objective remains to characterise the distribution of $M_n = \max(I_1, \ldots, I_n)$, where $\{I_k\}$ are the Rayleigh(σ)-distributed amplitudes of the *correlated* speckle. Consider the *independent* sequence $I_1^*, ..., I_n^*$, also Rayleigh(σ)-distributed. It was shown in section 5.2.3.3 that $M_n^* = \max(I_1^*, \ldots, I_n^*)$ tends asymptotically to a non-degenerate Gumbel distribution, denoted G_0, of parameters given in eq. (5.12). Then under suitable regularity conditions, M_n also tends to a Gumbel distribution, $G = G_0^\theta$ for a constant $0 < \theta \leq 1$, named the *extremal index* [Col01, theorem 5.2][Lea83, chapter 3]. With a_n and b_n defined in eq. (5.12), the location and scale parameters of G are respectively

$$\mu_n = b_n + a_n \log\theta = \sigma\sqrt{2\log n} + \log\theta \frac{\sigma}{\sqrt{2\log n}}, \tag{5.17}$$

$$s_n = a_n = \frac{\sigma}{\sqrt{2\log n}}. \tag{5.18}$$

So G and G_0 have the same scale parameter, but the location parameter of G is shifted by $a_n \log\theta < 0$ due to the effect of the correlation. The extremal index is interpreted as the inverse of the number of points in the average cluster size [Col01, p. 97]. The number $n_{\text{eff}} = n\theta$, where n the total number of pixels in the area of measurement, can therefore be seen as an effective number of speckle cells, or effective sample size, for the peak response. This brings theoretical

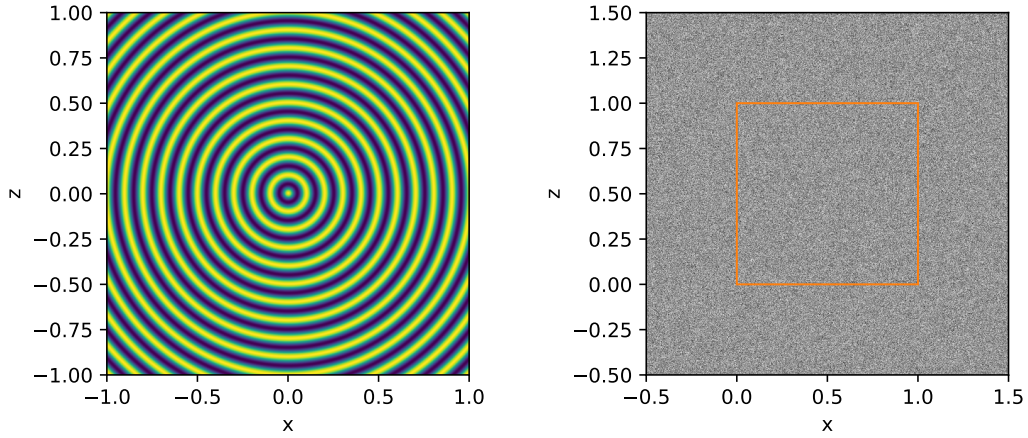

(a) (b)

Figure 5.3 – (a) Real part of the point spread function for $\lambda = 0.1$. (b) Real part of the normally distributed field $u(x, z)$. The orange square is the measurement surface.

foundations to the intuition formulated in the previous section that such a number exists. Note however that the theorem used here was demonstrated for 1D stationary sequences; the assumption has been made that the result holds for 2D stationary sequences such as the speckle. Nevertheless, the crux is to determine this extremal index for the speckle; an experimental attempt is presented later in this chapter.

5.3 Numerical generation of speckle

A pragmatic approach to confirm or refute certain intuitions on the peak amplitude distribution is to perform experiments. As a first step, a Monte Carlo study is conducted as it allows full control of the shape of the point spread function and quick generation of data.

The complex speckle amplitude is modelled using the linear imaging system theory [Wag83; Low70]

$$A(x, z) = \iint_{-\infty}^{+\infty} h(x - x', z - z')u(x', z')\, dx'\, dz' = (h * u)(x, z) \tag{5.19}$$

where $h(x, z)$ is the impulse response (point spread function), $u(x, z)$ is the imaged microstructure of the sample (input of the system), and $*$ denotes the convolution. The speckle is generated on a regular square grid $\mathcal{S}_E = \{(x_i, z_j) : i, j = 1 \,..\, N\}$, bounded by $(x_1, z_1) = (-0.5, -0.5)$ and $(x_N, z_N) = (1.5, 1.5)$, where $N = 512$ is the number of pixels in each direction, leading to a step size of $2/512 \approx 0.004$. The Fourier transform is used to make computation more efficient,

as by the convolution theorem [Bra00],

$$I(x,z) = \mathcal{F}^{-1}\{\mathcal{F}(h)\mathcal{F}(u)\}(x,z), \tag{5.20}$$

where $\mathcal{F}$ is the Fourier transform and $\mathcal{F}^{-1}$ its inverse. Using the discrete Fourier transform effectively replaces the convolution by a circular discrete convolution; to circumvent potential wrapping issues, only the measurement surface $\mathcal{S} = [0,1[\cup[0,1[$ (256×256 pixels) is considered.

The point spread function is set to

$$h(x,z) = h_1(x,z) = \exp\left(2\imath\pi\sqrt{x^2+z^2}/\lambda\right), \tag{5.21}$$

where λ is the wavelength. This PSF is used for illustrative purposes to introduce spatial correlation; however, it does not aim to model a realistic TFM PSF; in particular, the chosen PSF is independent of the position, and its amplitude is constant over space rather than decreasing with the distance from its centre. The microstructure is sampled from the circularly-symmetric normal distribution (complex numbers being seen here as 2D real vectors)

$$u(x_i,z_j) \sim \text{Normal}\left(0, \frac{\sigma^2}{N^2}\mathbf{1}\right), \tag{5.22}$$

where $\mathbf{1}$ is the 2×2 identity matrix. The pixels $u(x_i,z_j)$ are independent; in particular, there is no correlation between neighbouring pixels. This models a large number of grains for each resolution cell so that the speckle autocorrelation is governed primarily by the PSF. The speckle amplitude

$$A(x_k,z_k) = \sum_{i=1}^{N}\sum_{j=1}^{N} h(x_k-x_i, z_k-z_j)u(x_i,z_j) \tag{5.23}$$

has therefore the circularly-symmetric normal distribution

$$A(x_k,z_k) \sim \text{Normal}\left(0, \frac{\sigma^2}{N^2}\sum_{i=1}^{N}\sum_{j=1}^{N}|h(x_i,z_j)|^2\mathbf{1}\right). \tag{5.24}$$

For the considered PSF, the resulting covariance matrix is $\sigma^2\mathbf{1}$, so the speckle amplitude $I = |A|$ is Rayleigh(σ)-distributed.

Figure 5.3 shows the PSF and a realisation of the field $u(x,z)$. Figure 5.4 shows random samples of the generated speckle for various wavelengths; the finer the wavelength, the smaller the speckle cell size. The qualitative similarity between the generated speckle and actual TFM speckle is sufficient for this study; anticipating from the final results, a spatially decaying PSF leads to similar conclusions as for h_1. This microstructure model could also be improved if desired, for example using spherical grains [Yal96] or a Voronoi diagram [Bai19].

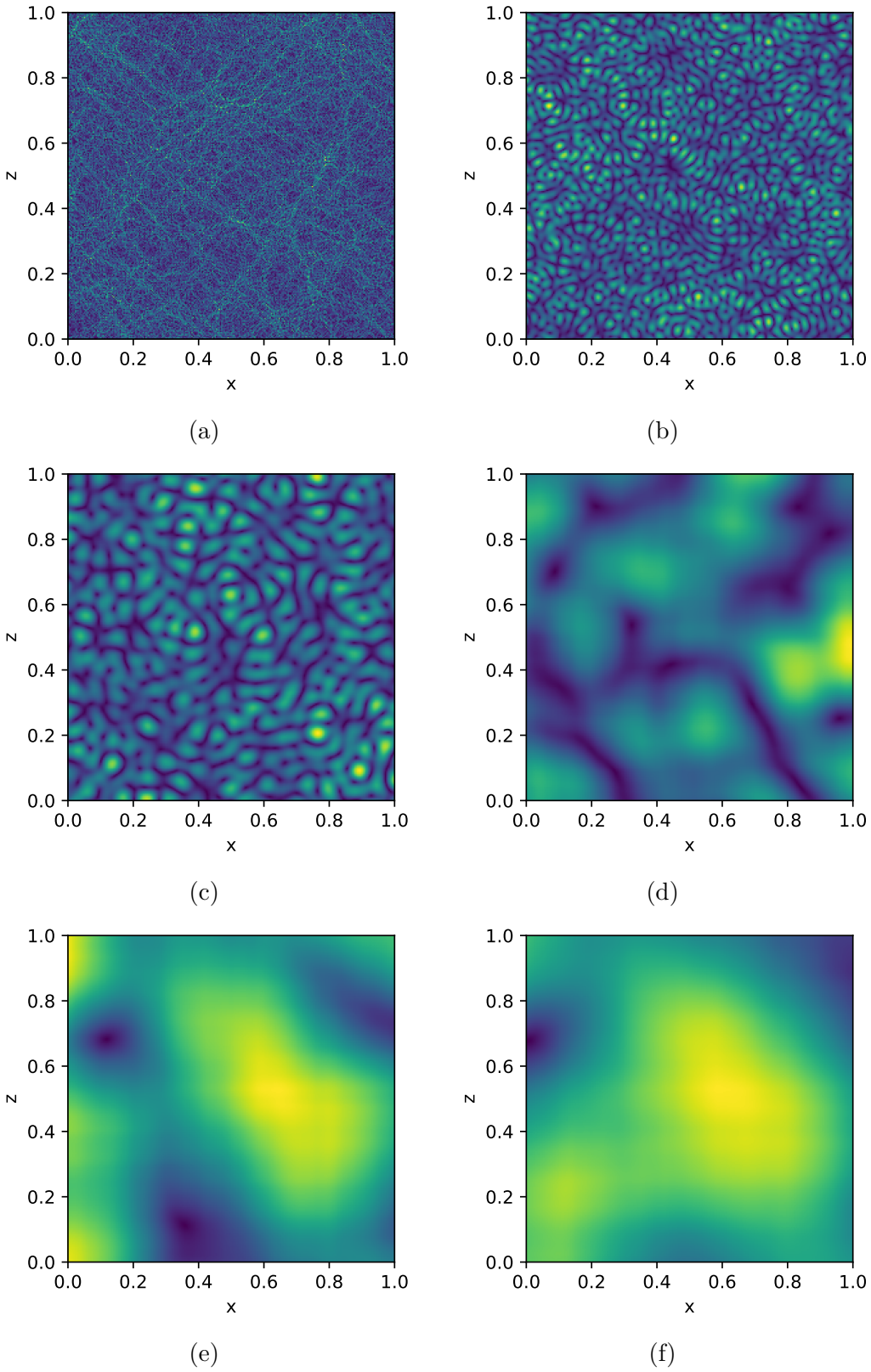

Figure 5.4 – Samples of the speckle $I = |A|$ at different wavelengths. (a) $\lambda = 0.01$, (b) $\lambda = 0.05$, (c) $\lambda = 0.1$, (d) $\lambda = 0.5$, (e) $\lambda = 1.0$, (f) $\lambda = 1.5$.

5.4 Experimental determination of the parameter σ

The Rayleigh distribution of the speckle amplitude is parametrised by σ. This quantity is generally unknown and must be estimated experimentally. Several estimators of σ are presented and studied in Siddiqui [Sid64], mainly in the i.i.d. case. One estimator from correlated observations is obtained by substituting the i.i.d. variables by the correlated ones. This substitution constitutes a pragmatic approach to build estimators; however, their theoretical properties are poorly understood. This section compares such estimators empirically.

5.4.1 Methods

5.4.1.1 Standard deviation of the normally distributed real part

Both the real and the imaginary part of the complex speckle amplitude are normally distributed $\mathrm{Norm}(0, \sigma^2)$. The maximum likelihood estimation of σ in the i.i.d. case is first recalled. Consider n independent variables $x_1, \dots, x_n$ of identical distribution $\mathrm{Norm}(0, \sigma^2)$. Its log-likelihood function is

$$\log \mathcal{L}(\sigma) = -n \log \sigma - \frac{n}{2} \log 2\pi - \frac{x_1^2 + \cdots + x_n^2}{2\sigma^2}. \tag{5.25}$$

Its derivative is

$$\frac{d \log \mathcal{L}}{d\sigma}(\sigma) = -\frac{n}{\sigma} + \frac{x_1^2 + \cdots + x_n^2}{2\sigma^3}. \tag{5.26}$$

Equating this equation to zero gives the well-known sample standard deviation

$$\hat{\sigma} = \sqrt{\frac{x_1^2 + \cdots + x_n^2}{n}}. \tag{5.27}$$

For the correlated amplitudes $\mathrm{Re}(A_1), \dots, \mathrm{Re}(A_n)$, the likelihood function is unknown in the general case, and there is no reason to believe that $\hat{\sigma}$ is a maximum likelihood estimator. Nevertheless, by analogy with the i.i.d. case, the sample standard deviation is considered as an estimate of σ:

$$\sigma_{\mathrm{std}} = \sqrt{\frac{\mathrm{Re}(A_1)^2 + \cdots + \mathrm{Re}(A_n)^2}{n}}. \tag{5.28}$$

5.4.1.2 Maximum likelihood estimation of the Rayleigh distribution

The log-likelihood of n independent variables $x_1, \dots, x_n$ of identical distribution $\mathrm{Rayleigh}(\sigma)$ is

$$\log \mathcal{L}(\sigma) = -2n \log \sigma - \sum_{k=1}^{n} \frac{x_k^2}{2\sigma^2} + \sum_{k=1}^{n} \log x_k. \tag{5.29}$$

Its differentiate is

$$\frac{d\log\mathcal{L}}{d\sigma}(\sigma) = -\frac{2n}{\sigma} + \frac{\sum_{k=1}^{n} x_k^2}{\sigma^3}. \tag{5.30}$$

Equating this equation to zero gives the maximum likelihood estimator

$$\hat{\sigma} = \sqrt{\frac{x_1^2 + \cdots + x_n^2}{2n}}. \tag{5.31}$$

As in the previous section, the actual maximum likelihood estimator for the correlated amplitudes is unknown. By analogy with the i.i.d. case, an estimator of σ from the correlated amplitudes $I_1, \ldots, I_2$ is obtained by substituting x_k by I_k:

$$\sigma_{\mathrm{ML}} = \sqrt{\frac{I_1^2 + \cdots + I_n^2}{2n}}. \tag{5.32}$$

Remark: it is easy to show that the maximum likelihood estimator of independent circularly-symmetric normally distributed complex amplitudes coincides with $\hat{\sigma}$ in eq. (5.31). So there is no practical advantage in considering the complex amplitude A as all the available information for the estimation of σ is carried by its modulus, i.e. I.

5.4.1.3 Method of moment

The mean (first moment) of a Rayleigh(σ) distribution is $\sigma\sqrt{\pi/2}$. An estimator of σ from the sample mean is therefore

$$\sigma_{\mathrm{MOM}} = \sqrt{\frac{2}{\pi}}\ \frac{I_1 + \cdots + I_n}{n}. \tag{5.33}$$

5.4.1.4 Order statistic

Consider n independent variables $X_1, \ldots, X_n$ of identical distribution Rayleigh(σ). The k-th order statistic of this sample is by definition the k-th smallest value, denoted X^k; for example, $X^{(1)}$ is the minimum and $X^{(n)}$ is the maximum. Siddiqui demonstrated that the optimum unbiased estimator from a single order statistic is approximatively [Sid63]

$$\sigma_{\mathrm{OS}} = 0.6275\ X^{(k)}, \tag{5.34}$$

$$k = \lfloor 0.79681\ (n+1) - 0.39841 + 1.16312\ (n+1)^{-1} \rceil, \tag{5.35}$$

where $\lfloor\cdot\rceil$ denotes the rounding to the nearest integer. As an example, for $n = 256^2$, the selected order statistic corresponds to the 79.7th percentile. The main practical advantage of

this estimator is that it relies on a single and relatively large value, so it remains accurate even though the smaller values are truncated (lack of dynamic range) or distorted due for example to quantisation error introduced by the acquisition hardware. As before, the estimator for the speckle is obtained by substituting the i.i.d. X_k by the correlated I_k.

5.4.2 Results

Table 5.3 – Statistics of the estimates of $\sigma = 1$ for $\lambda = 0.1$.

Estimator	Mean	Abs. bias	St. dev.	$Q_{95} - Q_5$
σ_{std}	0.99821	0.00179	0.06313	0.20300
σ_{ML}	0.99821	0.00179	0.04486	0.14770
σ_{MOM}	0.99926	0.00074	0.04504	0.14984
σ_{OS}	0.99888	0.00112	0.04517	0.15117

Table 5.4 – Statistics of the estimates of $\sigma = 1$ for $\lambda = 0.5$.

Estimator	Mean	Abs. bias	St. dev.	$Q_{95} - Q_5$
σ_{std}	0.98575	0.01425	0.14918	0.48094
σ_{ML}	0.99669	0.00331	0.10685	0.34621
σ_{MOM}	1.00190	0.00190	0.10924	0.35930
σ_{OS}	1.00037	0.00037	0.11092	0.36135

Two essential properties of an estimator $\hat{\sigma}$ are its bias, $\mathrm{E}(\hat{\sigma}) - \sigma$, that is whether on average the estimator is right, and its dispersion (or variability) around $\mathrm{E}(\hat{\sigma})$, quantified here by the standard deviation and the percentile range $Q_{95} - Q_5$, which ideally should be zero. The four estimators introduced in section 5.4.1 are compared empirically.

2000 independent speckle samples were generated as described in section 5.3; each sample containing 256^2 pixels. Tables 5.3 and 5.4 present the statistics of the estimates of σ for $\lambda = 0.1$ and $\lambda = 0.5$. For calculating the bias, the mean of the estimates is used as an approximation of the (theoretical) expected value of the estimator. The four techniques provide a reasonably

good estimation of σ. σ_{ML} has the smaller dispersion. Both σ_{MOM} and σ_{OS} have a smaller bias than σ_{ML}, at the cost of a marginally larger dispersion. Even in the most favourable scenario, $\lambda = 0.1$, the relative error made from a single estimation is 90% of the time up to $\pm 7.5\%$; averaging estimates from independent samples is needed to reduce this error. As the dispersion of the estimates is 2 orders of magnitude larger than the bias, it seems reasonable to prioritise control of the dispersion and therefore to select σ_{ML} as the best estimator; σ_{OS} and σ_{MOM} are however good alternatives. σ_{std} clearly stands out as the worse estimator as it has the largest bias and dispersion; it is not surprising as it ignores the imaginary part, which carries information. Regardless of the estimator, the estimations are worse for the larger wavelength, which is explained by the larger degree of correlation between the pixels.

5.5 Experimental determination of the effective sample size

This section aims to determine the equivalent number of independent points that would explain the peak response of correlated speckle, as introduced in section 5.2.4. The true value of the parameter σ is assumed to be known.

5.5.1 Methods

5.5.1.1 From the wavelength

As seen in sections 5.2.1 and 5.3, the PSF is parametrized by λ, and the speckle cell size is primarily driven by the PSF. Based solely on dimensional analysis, it is reasonable to define the speckle cell area as λ^2 (or $k\lambda^2$ for any $k > 0$). The number of cells in a measurement area $\mathcal{S} = 1$ is

$$n_\lambda = \frac{\mathcal{S}}{\lambda^2} = \frac{1}{\lambda^2}. \tag{5.36}$$

The actual value of n_λ is irrelevant ($k = 1$ is arbitrary); however, the trend provides a baseline for the comparison of various estimates of the effective sample size.

The quantity n_λ is only valid when the microstructure is much finer than the wavelength; otherwise, the speckle size depends on both the PSF and the microstructure. It is recalled the microstructure texture is governed by the pixel size (0.004). The actual number of independent

cells does not tend to infinity when the wavelength tends to zero, as eq. (5.36) suggests, as it is bounded by the number of degrees of freedom of the microstructure, which is here the total number of pixels.

5.5.1.2 Area of the main lobe of the autocorrelation function

As seen in section 5.2.4, Wagner et al. considered the speckle size area

$$\mathcal{S}_c = \iint_{-\infty}^{\infty} \frac{C_{I^2}(\Delta x, \Delta y)}{C_{I^2}(0,0)}\, d\Delta x\, d\Delta y, \tag{5.37}$$

where $C_{I^2}(\Delta x, \Delta y)$ is the autocovariance of I^2, that is the autocorrelation of $\bar{I}^2 = I^2 - \mathrm{E}(I^2)$. The terminology to describe $\mathcal{S}_c$ is awkward. $\mathcal{S}_c$ has the unit of a squared length, so it is technically an area. It is however tempting to call it a volume as it is obtained by a double integration over length axes. It will be called here "area", as in area under the curve of a 1D function.

The corresponding effective sample size in the measurement area $\mathcal{S}$ is

$$n_{\text{area}} = \frac{\mathcal{S}}{\mathcal{S}_c}. \tag{5.38}$$

The numerical implementation is as follows. The sample centred speckle intensity is

$$\bar{I}^2(x,z) = I^2(x,z) - \frac{1}{\mathcal{S}} \iint_{\mathcal{S}} I^2(x,z)\, dx\, dz. \tag{5.39}$$

As for the convolution in section 5.3, the autocorrelation is replaced by its circular counterpart and implemented with the discrete Fourier transform. Following Smith and Wagner [Smi84], the side lobes are excluded as they are contaminated by artefacts, which increases the robustness to noise but may also underestimate the true degree of correlation. The selection of the main lobe is illustrated in fig. 5.5. First, the gradient of the autocorrelation function along the axial distance $r = \sqrt{x^2 + z^2}$ is calculated (b). The autocorrelation function initially decreases from the centre, so this gradient is negative at the main lobe (c). The point at which the gradient becomes positive separates the main lobe from the first side lobe. The main lobe is finally isolated by determining the centremost cluster of connected pixels with a negative gradient (d).

In Goodman [Goo75], $\mathcal{S}_c$ is introduced in the study of the statistics of the speckle intensity I^2. In ultrasonics, it is more common to consider the speckle amplitude I. A second estimate of the effective sample size is obtained by substituting I^2 by I in the definition of $\mathcal{S}_c$ and the subsequent numerical implementation. Similarly, a third estimate is derived from the speckle complex amplitude A as this quantity is readily available.

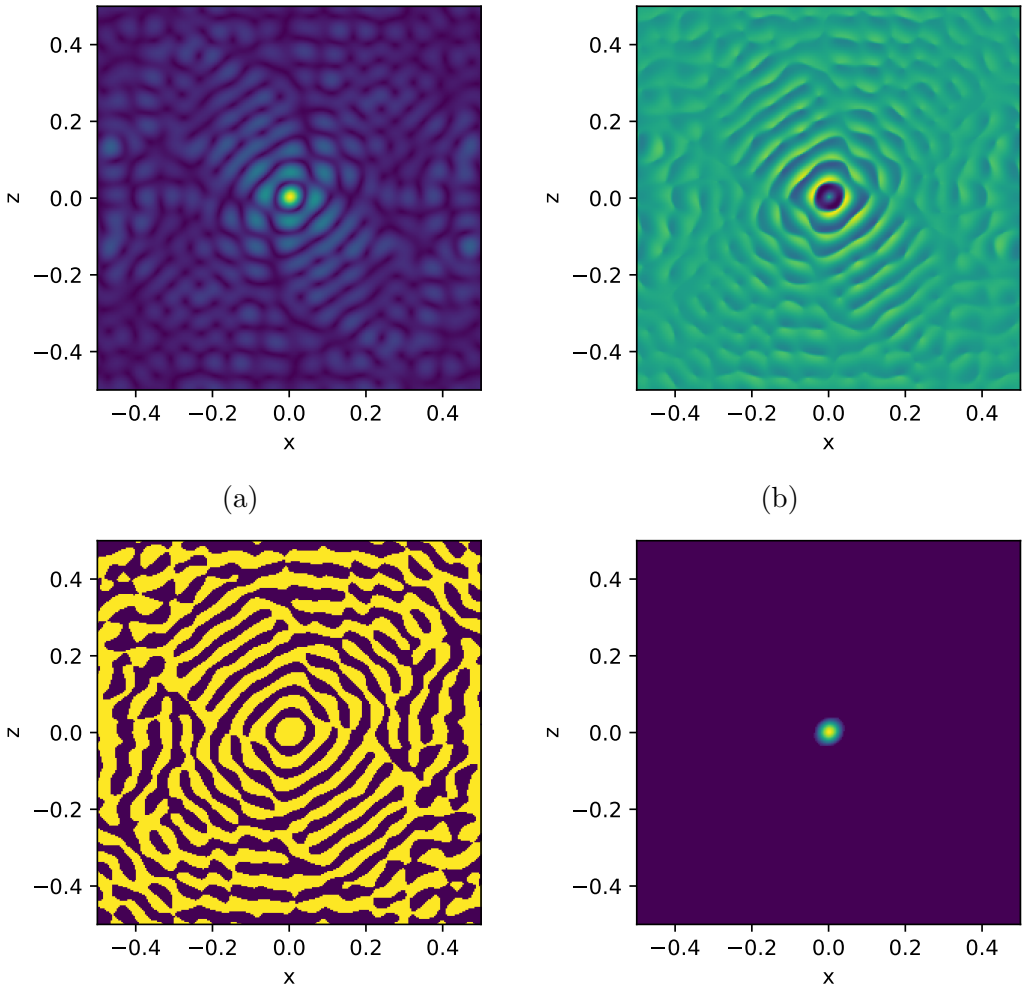

Figure 5.5 – Illustration of the calculation of n_{area}. (a) Initial autocorrelation function. (b) Gradient along $r = \sqrt{x^2 + z^2}$. (c) Threshold the gradient at 0. (d) Retain only the main lobe identified with the gradient.

5.5.1.3 Width of the main lobe of the autocorrelation function

A usual metric derived from the autocorrelation function of the speckle amplitude is the measure of the region over which this function exceeds a fraction τ of its maximum, such as 0.5 [Fos83] or $1/e \approx 0.37$ [Bev18], that is in 2D the area of

$$\left\{ \Delta x, \Delta y : \frac{C_{I^2}(\Delta x, \Delta y)}{C_{I^2}(0,0)} \geq \tau \right\} \tag{5.40}$$

In 1D, the term "full width at half maximum" is generally used for $\tau = 0.5$. By analogy, the term "width" will be used here, to avoid any confusion with the speckle area defined in the previous section section 5.5.1.2. As previously, the sides lobes are excluded from the calculation of the width. Figure 5.8 illustrates this calculation. The pixels where the autocorrelation function (a) exceeds $1/e$ are identified (b). The different pixel clusters are labelled (c), then only the main lobe is retained (d). The area of these pixels is calculated with numerical integration (rectangle rule). The ratio of the measurement area $\mathcal{S}$ by the lobe area defines the effective sample size n_{width}. As for the area of the autocorrelation function, it is unclear whether the speckle complex amplitude A, amplitude I or intensity I^2 should be used; the three quantities are considered.

5.5.1.4 From the MaxRayleigh distribution

As seen in section 5.2.3.2, the distribution of the maximum of n independent Rayleigh(σ)-distributed pixels is the MaxRayleigh(n, σ) distribution defined in eq. (5.7). Determining n such that this distribution best fits the observed peak amplitudes is the most natural definition of an effective sample size. As a first approach, n is estimated with maximum likelihood estimation. Suppose $p_1, \ldots, p_m$ are the peak amplitudes of each of m independent speckle samples. Recalling the PDF of M_n is

$$f_{M_n}(x) = n \frac{x}{\sigma^2} \exp\left(-\frac{x^2}{2\sigma^2}\right) \left(1 - \exp\left(-\frac{x^2}{2\sigma^2}\right)\right)^{n-1}, \tag{5.41}$$

the log-likelihood of the MaxRayleigh for these observations assuming σ is known is

$$\log \mathcal{L}(n) = m \log n + (n-1) \sum_{k=1}^{m} \log\left(1 - \exp\left(-\frac{p_k^2}{2\sigma^2}\right)\right) + K, \tag{5.42}$$

where the constant K is independent of m. Differentiating by n gives

$$\frac{d \log \mathcal{L}}{dn}(n) = \frac{m}{n} + \sum_{k=1}^{m} \log\left(1 - \exp\left(-\frac{p_k^2}{2\sigma^2}\right)\right). \tag{5.43}$$

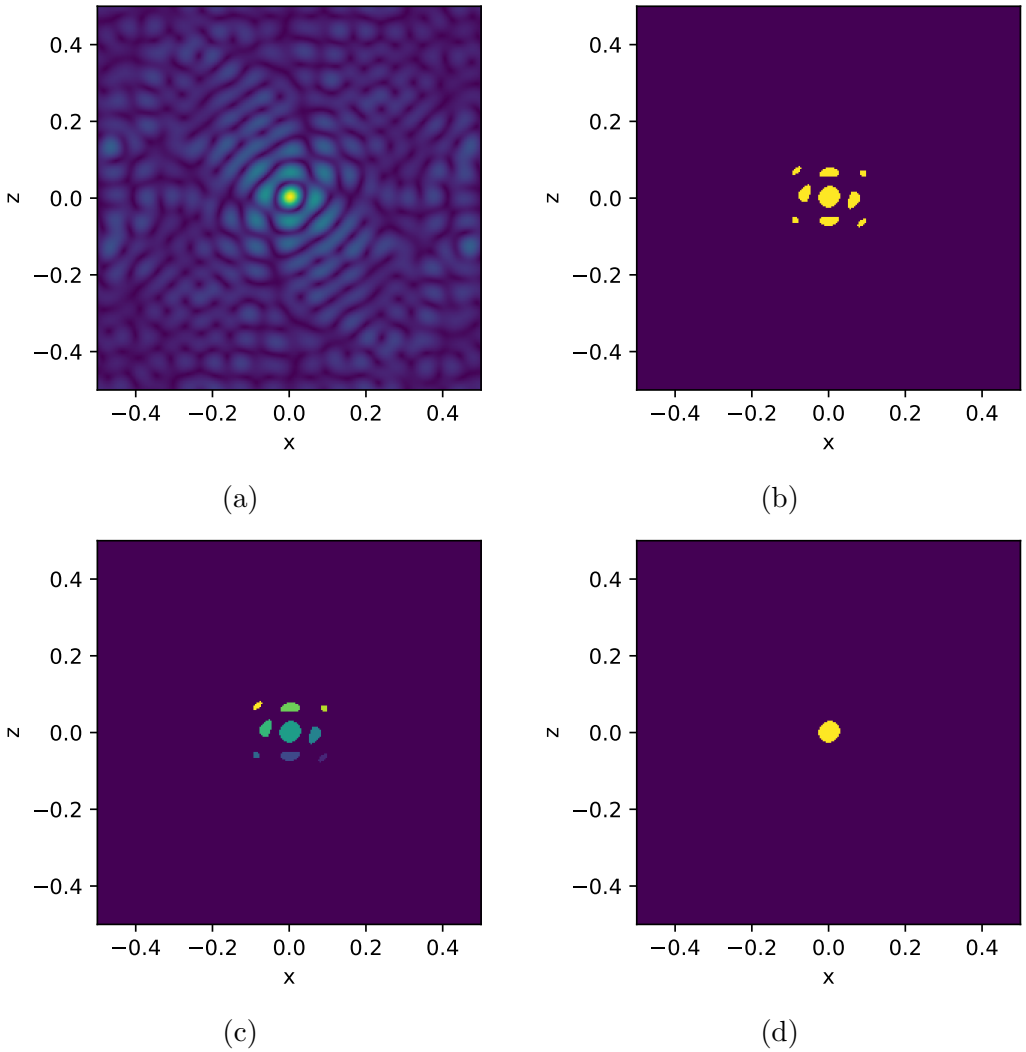

Figure 5.6 – Illustration of the calculation of n_{width}. (a) Initial autocorrelation function. (b) Threshold at $1/e$. (c) Identify the clusters of connected pixels. (d) Select the region over the threshold corresponding to the main lobe.

Equating this equation to zero gives the maximum likelihood estimator

$$n_{\text{MaxRayl}} = -\frac{m}{\sum_{k=1}^{m} \log\left(1 - \exp\left(-\frac{p_k^2}{2\sigma^2}\right)\right)} = -\frac{m}{\sum_{k=1}^{m} \log F(p_k)}, \tag{5.44}$$

where F is again the CDF of the Rayleigh(σ) distribution.

Obtaining n_{MaxRayl} experimentally is difficult as each value p_k requires an independent measurement of the speckle. Therefore, dozens of experiments could be required to obtain an accurate estimate. This contrasts with n_{area} and n_{width} which operate on a single speckle realisation.

5.5.1.5 From the extremal index

Recall from section section 5.2.4.2 that the distribution of the maximum of n *correlated* amplitudes is asymptotically the Gumbel distribution with the location and scale parameter

$$\mu = \sigma\sqrt{2\log n} + \log\theta\frac{\sigma}{\sqrt{2\log n}}, \tag{5.45}$$

$$s = \frac{\sigma}{\sqrt{2\log n}}, \tag{5.46}$$

where $\theta \in]0, 1]$ is the extremal index. θ is determined using maximum likelihood estimation. Given that n and σ are fixed, the likelihood depends on θ only via the parameter μ. As μ is a strictly increasing function of θ, maximising the likelihood for θ is equivalent as maximising it for μ. The latter option is considered as it makes the algebra easier. Denoting again $p_1, \ldots, p_m$ the peak amplitudes of each of m independent speckle samples, the associated log-likelihood and its derivatives are

$$\log\mathcal{L}(\mu) = -m\log s - \sum_{k=1}^{m}\frac{p_k - \mu}{s} - \sum_{k=1}^{m}\exp\left(-\frac{p_k - \mu}{s}\right), \tag{5.47}$$

$$\frac{d\log\mathcal{L}}{d\mu}(\mu) = \frac{m}{s} - \frac{1}{s}\sum_{k=1}^{m}\exp\left(-\frac{p_k - \mu}{s}\right), \tag{5.48}$$

$$\frac{d^2\log\mathcal{L}}{d\mu^2}(\mu) = -\frac{1}{s^2}\sum_{k=1}^{m}\exp\left(-\frac{p_k - \mu}{s}\right). \tag{5.49}$$

The second derivative is strictly negative for all μ so the first derivative is strictly decreasing so the equation $\frac{d\log\mathcal{L}}{d\mu}(\mu) = 0$ has a unique solution. It is easy to verify this solution is [For11, §19.3]

$$\hat{\mu} = -s\log\left[\frac{1}{m}\sum_{k=1}^{m}\exp\left(-\frac{p_k}{s}\right)\right]. \tag{5.50}$$

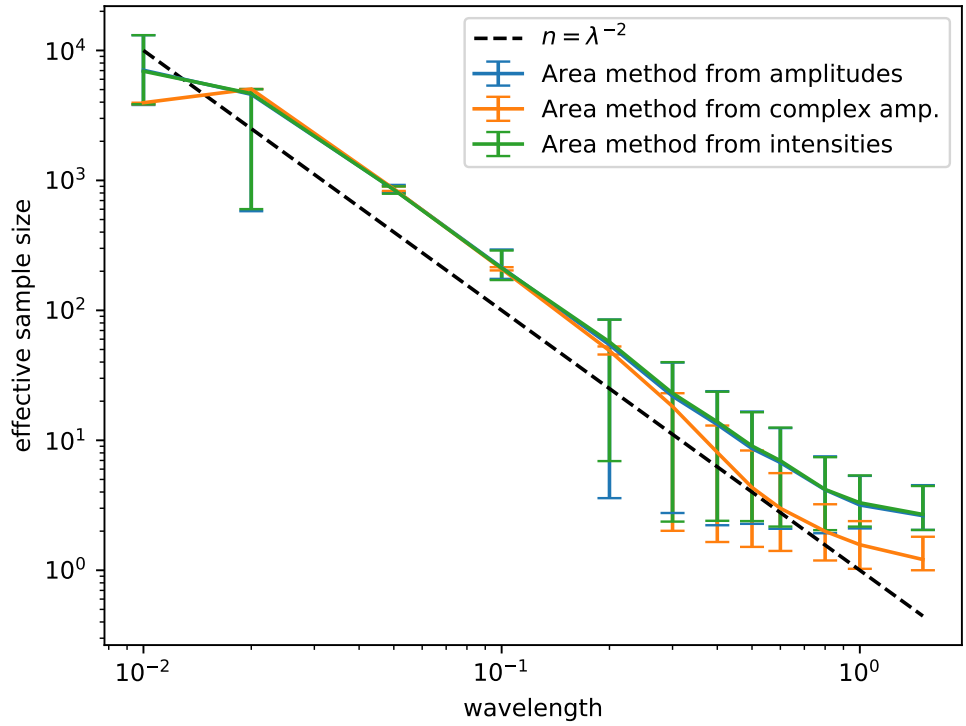

Figure 5.7 – Comparison of the n_{area} for the complex amplitudes, amplitudes and intensities. Error bars: 5th and 95th percentiles.

Combined with eq. (5.45), the maximum likelihood estimator of the extremal index is

$$\hat{\theta} = \left(n^2 \sum_{k=1}^{m} \exp\left(-\frac{p_k}{s}\right) \right)^{-1}. \tag{5.51}$$

The effective sample size derived from the extremal index (EI) is finally

$$n_{\text{EI}} = n\hat{\theta} = \left(n \sum_{k=1}^{m} \exp\left(-\frac{p_k}{s}\right) \right)^{-1}. \tag{5.52}$$

This number is interesting as it has more solid theoretical foundations that n_{MaxRayl}, based on the assumed existence of an effective sample size. As n_{MaxRayl}, its calculation requires many independent samples. This estimator is also only valid for a large number of speckle cells in the area of measurement.

5.5.2 Results

The quantities n_λ, n_{area}, n_{width}, n_{MaxRayl} and n_{EI} are compared for a range of 12 wavelengths between 0.01 and 1.5. For each wavelength, $m = 200$ independent speckle samples are generated

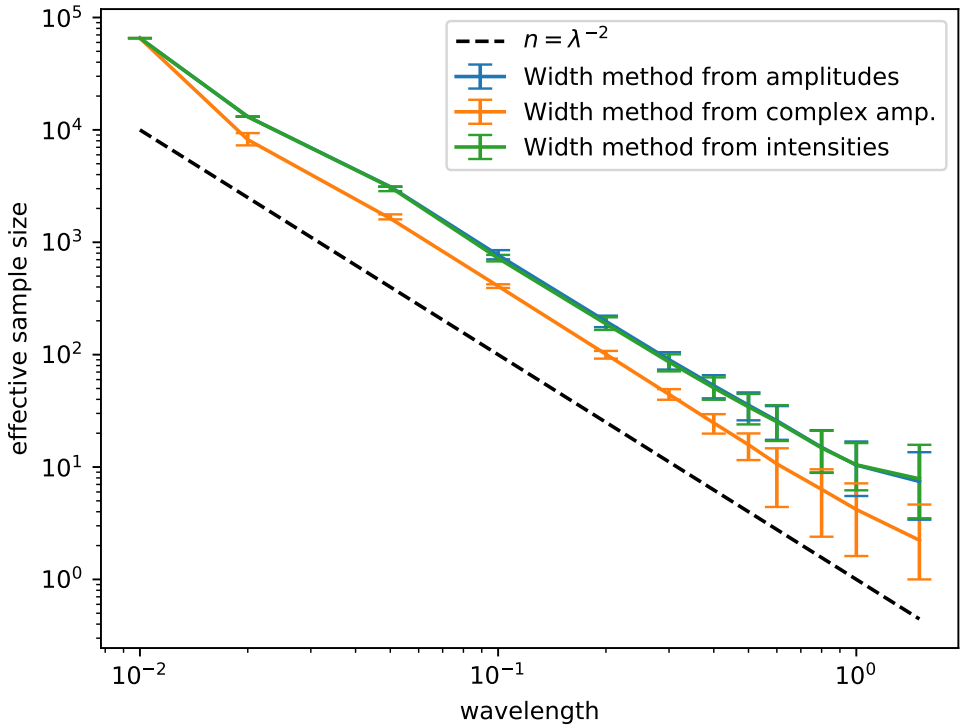

Figure 5.8 – Comparison of the n_{width} for the complex amplitudes, amplitudes and intensities. Error bars: 5th and 95th percentiles.

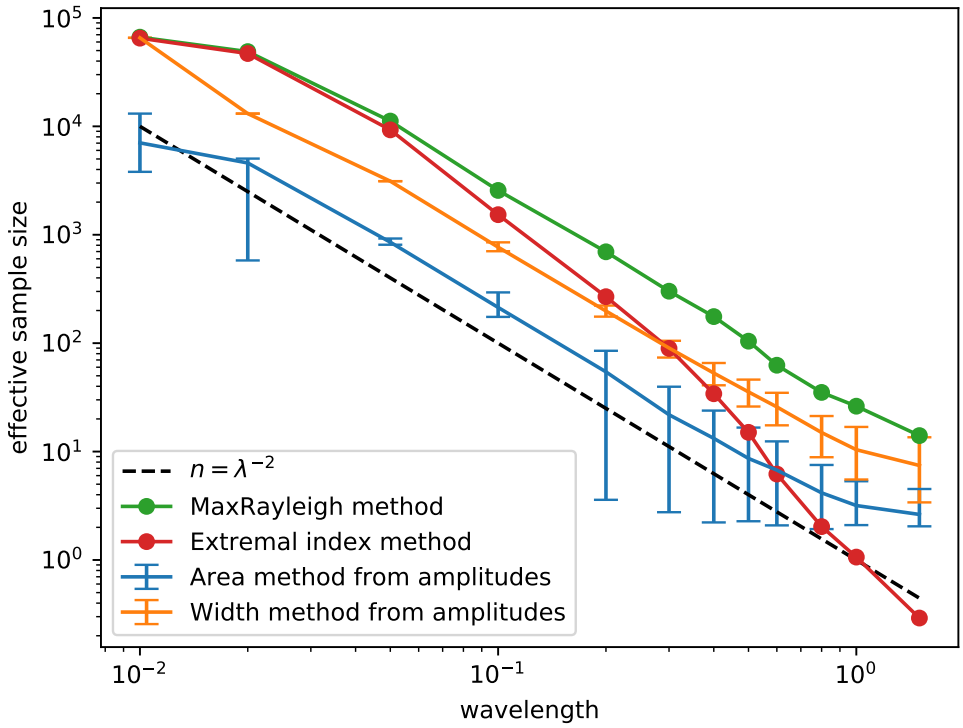

Figure 5.9 – Comparison of n_{MaxRayl}, n_{EI}, n_{area} and n_{width}.

as described in section 5.3. For n_{area} and n_{width}, one estimate is obtained per speckle realisation; in the figures, the mean, the 5th and 95th percentiles (error bars) are reported. For n_{MaxRayl} and n_{EI}, only a single estimate is obtained from all samples; no error bar can be provided.

Figure 5.7 presents the results of the estimator n_{area}. There is reasonable agreement with the predicted trend $n = \lambda^{-2}$. The estimates obtained from the speckle complex amplitudes A, amplitudes I and intensities I^2 have overlapping error bars; this suggests they all estimate the same quantity; the only exception is $\lambda = 1.5$ which presents systematic errors as explained below. For wavelengths between 0.02 and 0.2, the estimates based on the complex amplitudes are credible and have the least dispersion. Overall most data points have large uncertainties, more than one order of magnitude in the worst cases. They are primarily caused by measurement errors. For smaller wavelengths, the density of pixels is too low to discretise sufficiently the main lobe, which causes two kinds of errors: 1) the main lobe is well identified but its area is miscalculated due to the poor resolution and rounding errors, 2) the technique based of the axial gradient described in section 5.5.1.2 fails to separate the main lobe from the side lobes, connecting more pixels than necessary, which eventually underestimates the effective sample size. For larger wavelengths, two causes of errors were identified: 1) again, the main lobe is misidentified, for example when its shape is elliptical rather than circular, 2) the main lobe does not fully fit in the measurement box. Overall, the estimator n_{area} could greatly benefit from a better lobe separation technique.

Figure 5.8 presents the results of the estimator n_{width}. There is a very good agreement with the trend $n = \lambda^{-2}$. The one identified measurement error is at the smallest wavelength ($\lambda = 0.01$): the peak is reduced to a single pixel, its width is not measured accurately. As in the previous case, it is expected that the measurement becomes unreliable when the peak size becomes larger than the measurement area; this would happen for wavelengths larger than studied here. All data points except $\lambda = 0.01$ are credible; the dispersion around the estimates, which progressively increases as the number of effective samples decreases, is explained solely by the sampling error. The estimator n_{width} obtained from the amplitudes and the intensities give very similar results; however, using the complex amplitudes gives a different result; the estimators are therefore not interchangeable. The two former estimators should be preferred as they have a lower dispersion.

Figure 5.9 presents the results of the estimators n_{width}, n_{area}, n_{MaxRayl} and n_{EI}. The

estimator n_{MaxRayl} has a good agreement with the trend $n = \lambda^{-2}$; no reason to suspect the credibility of these estimates was identified. The estimates from n_{EI} tend to n_{MaxRayl} as the wavelength decreases; although these estimators have different foundations, they asymptotically estimate the same quantity, which retrospectively brings confidence in the heuristic argument on which n_{MaxRayl} is based. The erratic trend of n_{EI} is explained by the insufficient number of speckle cells in the measurement area; this estimator is indeed only valid asymptotically. Depending on the estimator, the effective sample size varies by an order of magnitude: at $\lambda = 0.1$, $n_{\text{MaxRayl}} = 2563$, $n_{\text{width}} = 718$ and $n_{\text{width}} = 213$; equivalently, as a speckle cell length $\sqrt{\mathcal{S}/n_{\text{eff}}}$, the results are respectively 0.20λ, 0.36λ, 0.68λ. However, only n_{MaxRayl} is relevant for the prediction of the peak response of the speckle: as illustrated in figs. 5.10 and 5.11, the MaxRayleigh distribution with the parameter n_{MaxRayl} fits well the observed peak responses. The Gumbel distribution with the fitted extremal index fits well the data for the smallest wavelength; the agreement decreases as the wavelength increases, once again because this distribution is only asymptotically valid. The MaxRayleigh distributions with parameters n_{width} or n_{area} have a poor agreement. Fundamentally, this shows the effective sample size for the peak amplitude is different from the one for the mean speckle amplitude (section 5.2.4.1).

The effect of the PSF is now briefly addressed. Throughout this chapter, the PSF defined in eq. (5.21), $h_1(x, z)$, was used for the numerical results. For completion, two other PSFs which a spatial exponential decay are considered, which model more closely the reality:

$$h_2(x, z) = \exp\left(2\imath\pi\sqrt{x^2 + z^2}/\lambda\right) \exp\left(-\frac{x^2 + z^2}{\lambda^2}\right) \tag{5.53}$$

$$h_3(x, z) = \exp\left(2\imath\pi\sqrt{x^2 + z^2}/\lambda\right) \exp\left(-\frac{x^2 + z^2}{a^2}\right) \tag{5.54}$$

with a such that the window amplitude is 0.01 at a distance of 1 from the centre. Figure 5.12 presents the results of the estimators n_{width}, n_{area}, n_{MaxRayl} and n_{EI} for these two PSFs, as done previously for h_1 in fig. 5.9. The effective sample size, here estimated with the MaxRayleigh method, depends on the PSF: for $\lambda = 0.1$, $n_{\text{eff}} = 2563$ for h_1, $n_{\text{eff}} = 4179$ for h_2, $n_{\text{eff}} = 3015$ for h_3. This is not surprising: the degree of spatial coherence in the speckle depends on the PSF. More importantly for this study, the estimates of the effective sample size as a function of the wavelength have very similar trends regardless of the chosen PSF. This confirms that the conclusions drawn above on the estimation of n_{eff} hold for spatially decaying PSFs.

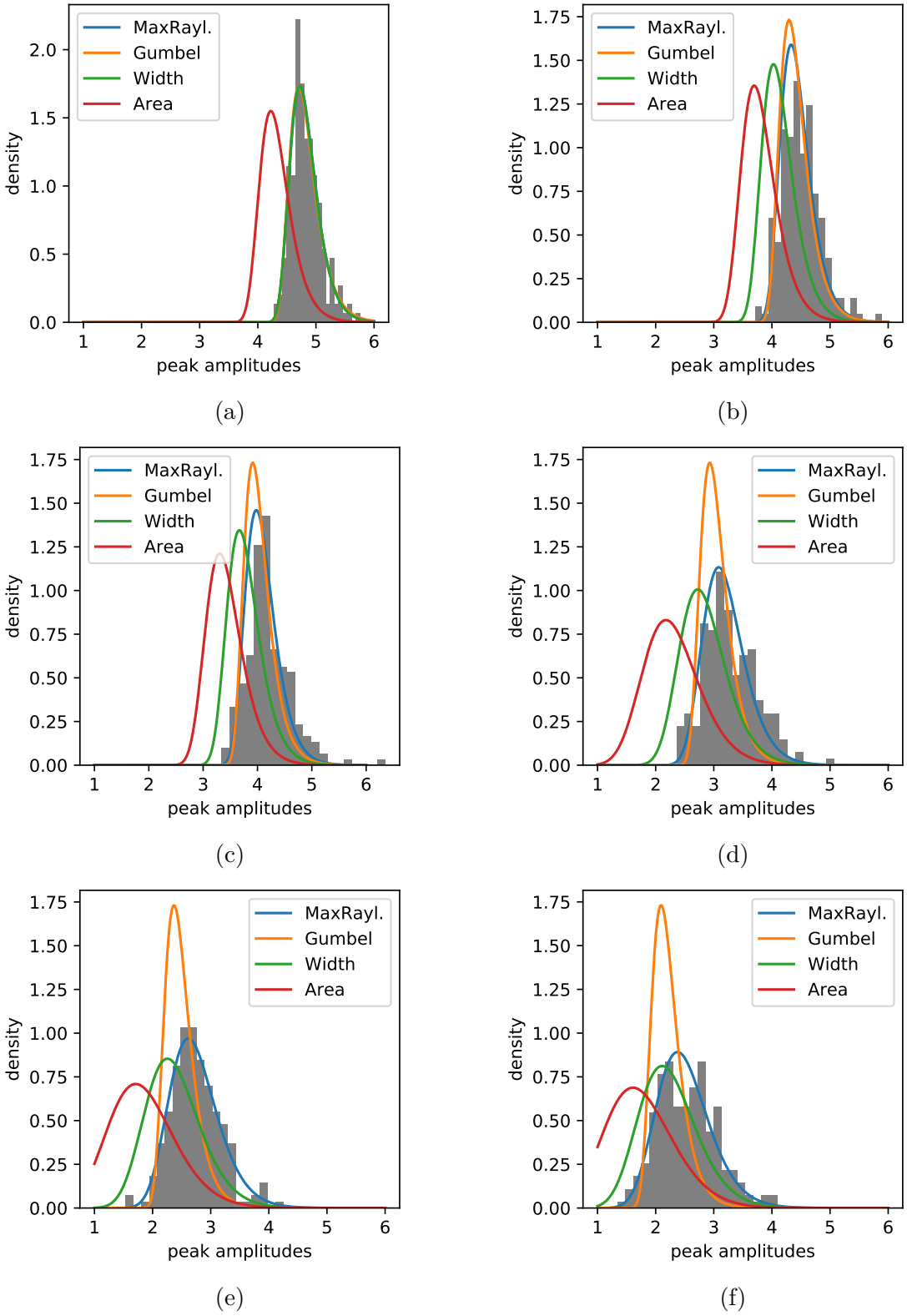

Figure 5.10 – Histograms of the observed peak amplitudes against the MaxRayleigh distributions with parameters n_{MaxRayl}, n_{area} and n_{width}, and the Gumbel distribution with the fitted extremal index. (a) $\lambda = 0.01$, (b) $\lambda = 0.05$, (c) $\lambda = 0.1$, (d) $\lambda = 0.5$, (e) $\lambda = 1.0$, (f) $\lambda = 1.5$.

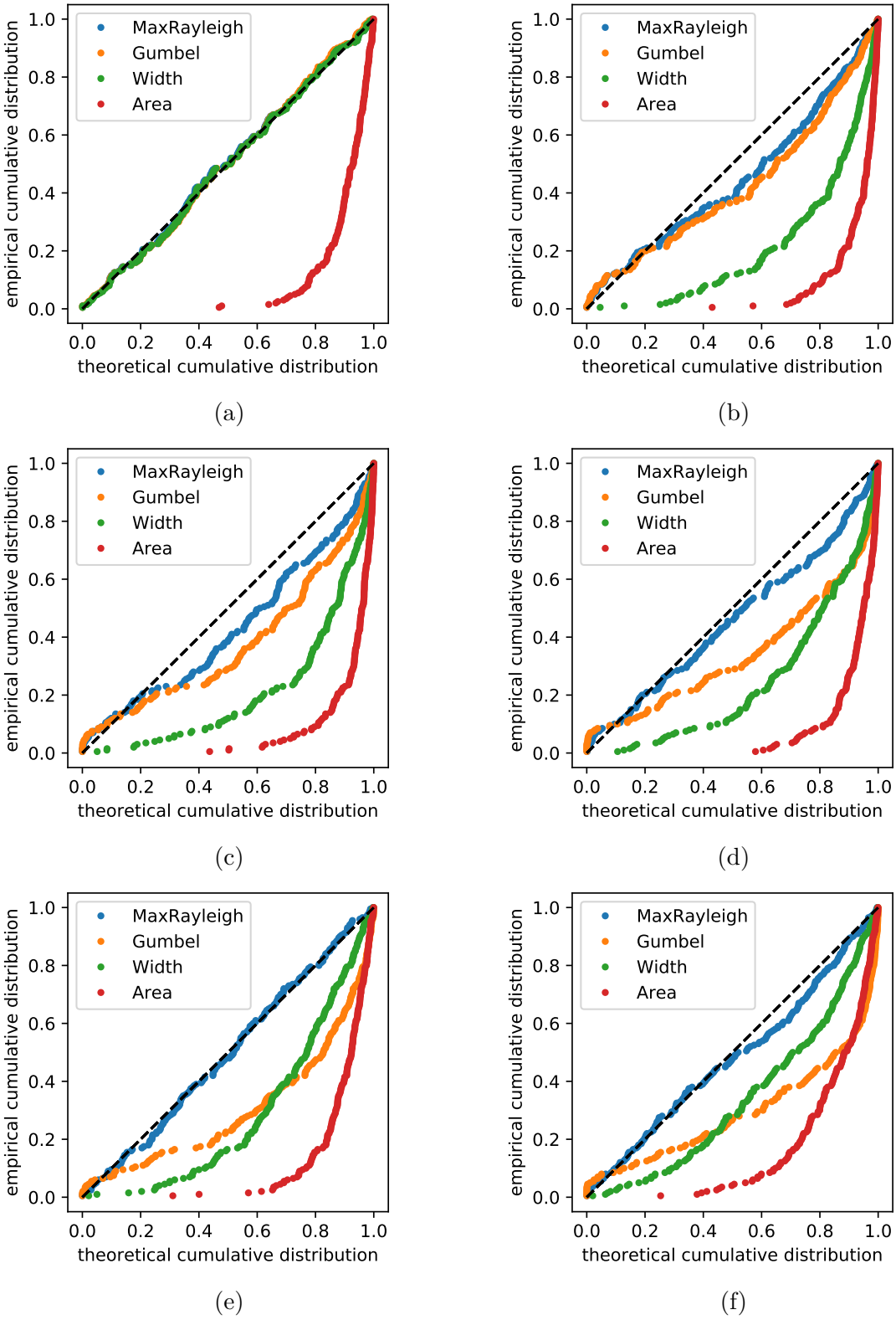

Figure 5.11 – P-P plots of the observed peak amplitudes against the MaxRayleigh distributions with parameters n_{MaxRayl}, n_{area} and n_{width}, and the Gumbel distribution with the fitted extremal index. (a) $\lambda = 0.01$, (b) $\lambda = 0.05$, (c) $\lambda = 0.1$, (d) $\lambda = 0.5$, (e) $\lambda = 1.0$, (f) $\lambda = 1.5$.

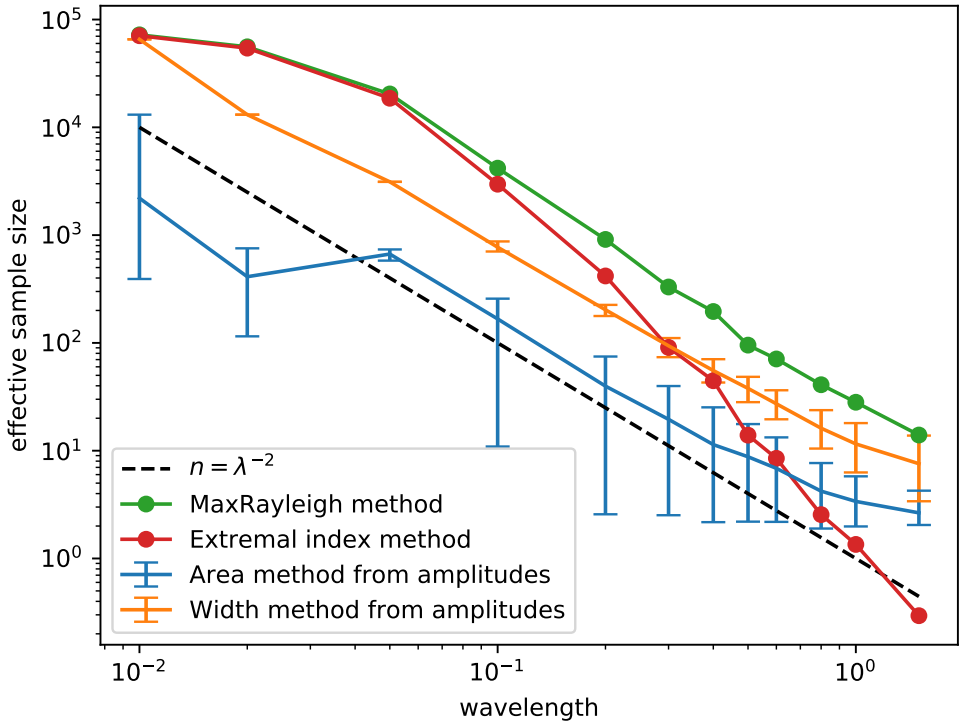

(a)

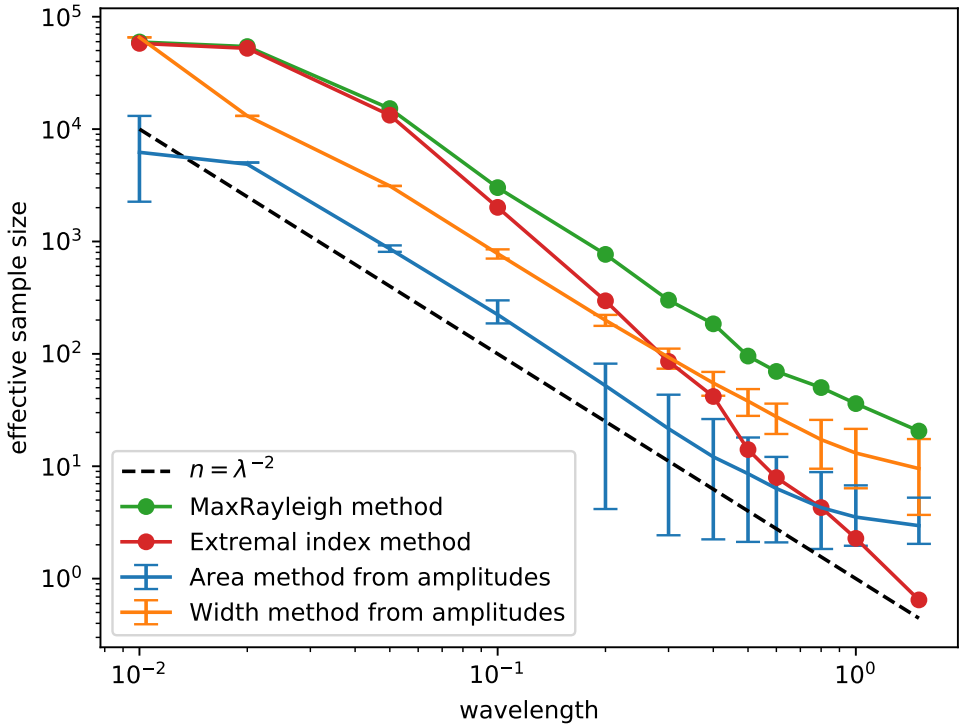

(b)

Figure 5.12 – Comparison of n_{MaxRayl}, n_{EI}, n_{area} and n_{width} for the alternative PSFs (a) $h_2(x, z)$ and (b) $h_3(x, z)$.

5.6 Conclusion

This chapter studied the distribution of the peak amplitude of the speckle, that is up to a scaling factor the SNR of an image in the absence of a defect. At an individual pixel, the speckle amplitude is accurately modelled by a Rayleigh(σ) distribution. The distribution of independent pixels is also well understood. The distribution of correlated pixels, as for realistic speckle, is more challenging, which motivated the empirical approach adopted in this chapter.

Several techniques were compared to experimentally determine the Rayleigh scale σ. The maximum likelihood estimator, σ_{ML} (eq. (5.32)), obtained by taking the root-mean-square of the image pixel amplitudes, is the recommended one as it has the smallest dispersion and an acceptable bias; the estimate obtained from an order statistic, σ_{OS} (eq. (5.35)), is a good alternative if the lower range of the speckle amplitudes is truncated or distorted. It is highly desirable to repeat the estimation of σ on independent speckle samples and to average them to obtain a more accurate final estimation.

Contrarily to the mean amplitude of the speckle, used notably as a metric in medical ultrasound, the peak amplitude depends on the size of the measurement box: the larger the area, the higher the expected peak amplitude. It was empirically demonstrated that the peak amplitude distribution of the observed speckle is well modelled by the distribution of the peak amplitude distribution of n_{eff} independent points, termed MaxRayleigh in this chapter, n_{eff} being the effective sample size. In other words, the peak amplitude in a measurement area $\mathcal{S}$ is explained by the peak amplitude of n_{eff} independent speckle cells of average size $\mathcal{S}/n_{\mathrm{eff}}$; however, this interpretation in terms of independent speckle cells is restricted to a specific statistic (the peak amplitude) rather than being universal; in particular, a different speckle cell size is obtained for the mean amplitude. The best estimator of n_{eff} that was obtained is the maximum likelihood estimator of the MaxRayleigh distribution, n_{MaxRayl} (eq. (5.44)), which remains reliable in the whole range of wavelengths considered in this study. Although n_{MaxRayl} is obtained with a heuristic, it coincides asymptotically with the estimator based on the extremal index, n_{EI} (eq. (5.52)), which is derived from mathematically rigorous results of the extreme value theory. However, these two estimators are difficult to use in practice as they require many independent samples. Two other estimators based on the autocorrelation function of the speckle, n_{area} and n_{width}, previously studied in the literature, were shown to

differ mainly from n_{MaxRayl} by a multiplicative coefficient. This coefficient likely depends on the PSF and the microstructure; if it was known, these estimators could be used to practically determine n_{MaxRayl} with a limited number of samples.

Chapter 6

A variant of delay-and-sum imaging using the geometric median

6.1 Introduction

Delay-and-sum imaging algorithms are a class of established techniques which form an image by synthetically backpropagating the ultrasonic wave field as a post-processing step, which leads to a constructive interference of the target signal and a destructive interference of the noise [Wil13]. As discussed in chapter 2, delay-and-sum algorithms include the Total Focusing Method[Hol05; Zha10b], the Synthetic Aperture Focusing Technique[Doc86], Plane Wave Imaging [Le 16], and Virtual Source Aperture [Sut12; Kar95].

Multiple images of the same specimen can be formed with any of these techniques by exploiting different wave modes including or not a reflection against the back wall, an approach known as multi-mode or multi-view imaging. As the recorded ultrasonic data contains a superposition of wave modes, imaging with one mode leads to the creation of artefacts in the image caused by the others [Por08]. Existing artefact filtering techniques are based on the identification (manually or with a threshold) then suppression (with zeroing or subtraction) of the signal which creates artefacts in other views [Por08; Iak14]. Another artefact filtering strategy consists in reducing the influence of unphysical ultrasonic paths in the reconstruction using appropriate weights, which has been done in composite materials [Li13] and for planar defects [Iak14]. The weights may also be chosen based on the signal statistics, an approach termed adaptive beamforming [Li12; Eng11; Tia19]. A different strategy to mitigate the

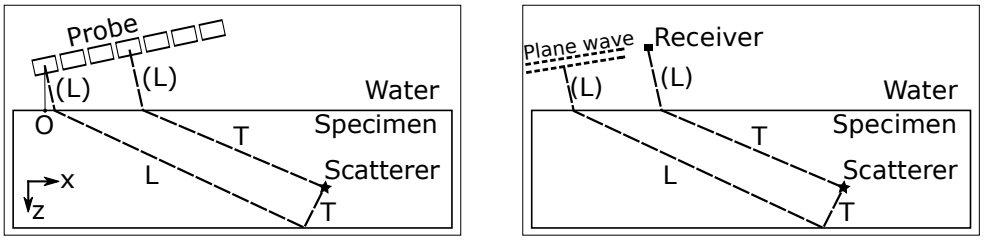

(a) (b)

Figure 6.1 – Inspection configuration. The rays shown correspond to (a) the TFM view LT–T and (b) the PWI view LT–T, where L stands for longitudinal and T for transverse. The point O is the origin of the coordinate system.

influence of artefacts, when a specific defect type can be assumed, is to only consider views where the known defect has a significant amplitude [Sy18c; Bud19].

In all delay-and-sum techniques, the pixel amplitude is obtained by summing ultrasonic signals to achieve constructive interference of the defect signal and destructive interference of the noise. Under suitable assumptions, this is an approximate solution of the inverse scattering problem under the Born approximation [Gil06; Sim08]. However, in the presence of high amplitude boundary reflections, typically neglected in the inverse problem, this theoretical justification becomes more questionable. Using probabilistic modelling, this chapter demonstrates the summation is justified for normally distributed noise, but may cause imaging artefacts in case of contamination by high amplitude spurious signals, such as boundary reflections. In this chapter, the summation is replaced by the more statistically robust geometric median to achieve the suppression of some artefacts. The consequences for the defect signal-to-noise ratio, the noise and the artefacts are explored and experimental results are presented for the inspection of a copper block using TFM and PWI.

The content of this chapter was the object of a publication, along with the code and the raw data [Bud20]. The experimental data were kindly provided by Dr Rhodri Bevan.

6.2 Delay-and-sum algorithms in ultrasonic array imaging

Consider an ultrasonic array of N elements. The continuous-time signal transmitted by element i and recorded by element j is denoted $f_{ij}(t)$; it can be obtained from its discrete-time equivalent with any interpolation technique; Lanczos interpolation [Duc79] is used here. The Full Matrix Capture (FMC) data is the set of the N^2 time signals $\{f_{ij}(t) : i = 1\,..\,N, j = 1\,..\,N\}$. An image can be formed by post-processing the FMC using the Total Focusing Method [Hol05; Zha10b]

$$I_0^{\mathrm{TFM}}(\boldsymbol{r}) = \sum_{i=1}^{N}\sum_{j=1}^{N} \tilde{f}_{ij}(\mathcal{T}_{ij}(\boldsymbol{r})), \tag{6.1}$$

where $\left|I_0^{\mathrm{TFM}}(\boldsymbol{r})\right|$ is the pixel amplitude at position $\boldsymbol{r}$, $\tilde{f}_{ij}(t)$ is the analytic (complex) signal obtained with the Hilbert transform, and $\tau_{ij}(\boldsymbol{r})$ is the propagation time corresponding to the ray path from the transmitter i to the position $\boldsymbol{r}$ and finally to the receiver j, calculated with any suitable ray tracing technique. Apodisation is ignored here but could be included if desired. Different images, or views, are obtained by considering ray paths which include or not a reflection against the back wall and which are either longitudinal (L) or transverse (T) waves; for example, fig. 6.1a shows the TFM view LT–T, where LT is the ray path from the transmitter to the scatterer and T the path from the scatterer to the receiver; this nomenclature ignores the ray leg in the water which is always longitudinal. In eq. (6.1), first the double sum is rewritten as a single sum, second the notation $x_k \coloneqq \tilde{f}_{ij}(\mathcal{T}_{ij}(\boldsymbol{r}))$ is used for brevity, and third the result is scaled by $n \coloneqq N^2$, leading to

$$I_1^{\mathrm{TFM}}(\boldsymbol{r}) = \frac{1}{n}\sum_{k=1}^{n} x_k. \tag{6.2}$$

$I_0^{\mathrm{TFM}}(\boldsymbol{r})$ and $I_1^{\mathrm{TFM}}(\boldsymbol{r})$ are equal up to a multiplicative factor $1/n$; as an image is generally rescaled by an arbitrary image point, this factor has no practical consequence. The use of this factor is not strictly necessary, it merely makes the probabilistic model developed in the following section easier to follow. However, it becomes clear with Eq. (6.2) that $I_1^{\mathrm{TFM}}(\boldsymbol{r})$ is the (complex) mean of $\{x_k : k = 1\,..\,n\}$.

Plane Wave Imaging algorithm [Le 16] has a similar form:

$$I_0^{\mathrm{PWI}}(\boldsymbol{r}) = \sum_{q=1}^{Q}\sum_{j=1}^{N} \tilde{g}_{qj}(\mathcal{T}_{qj}(\boldsymbol{r})), \tag{6.3}$$

where $g_{qj}(t)$ is the time signal corresponding to the q-th emitted plane wave and the j-th receiver, and $\mathcal{T}_{qj}(\boldsymbol{r})$ is the total propagation time of the q-th plane wave from the probe to the image point, and of a cylindrical wave from the image point to the receiver j; details are given in appendix C As for the TFM algorithm, several views can be formed; for example, fig. 6.1b shows the PWI view LT–T, where LT is the plane wave path in transmission and T is the cylindrical wave path in reception. Again, this equation can be rewritten (up to a scaling n) as

$$I_1^{\mathrm{PWI}}(\boldsymbol{r}) = \frac{1}{n}\sum_{k=1}^{n} x_k, \tag{6.4}$$

with this time $x_k \coloneqq \tilde{g}_{qj}(\mathcal{T}_{qj}(\boldsymbol{r}))$ and $n \coloneqq N \times Q$.

In conclusion, delay-and-sum algorithms form an image pixel by summing appropriately chosen data points, which is equivalent to calculating their mean up to a multiplicative constant. The consequence of this operation is explored in the following sections.

6.3 Probabilistic modelling of noise and signal

6.3.1 Theory

A probabilistic model of the ultrasonic data x_k in the absence or presence of a defect is introduced in this section. Following Wilcox [Wil13], two sources of noise are considered: the random noise (thermal acoustic noise in the sample, electronic noise in the instrumentation), and the coherent noise, which includes grain noise. The random noise can be suppressed by averaging multiple independent transmissions but the coherent noise cannot, which ultimately limits the defect detectability. As discussed in section 5.2, the grain noise is caused by the interaction of the elastic wave with the material microstructure. It is classically modelled as the superposition of grain scattering events [Wag83; Yal96]. Each grain response is assumed to have the same amplitude and a uniformly distributed phase. Ignoring multiple scattering, then the grain responses are independent and by the central limit theorem their superposition is the circularly-symmetric normal distribution

$$x_k^{\mathrm{grain}} \sim \mathrm{Normal}(0, \sigma^2\mathbf{1}). \tag{6.5}$$

The complex random variable x_k is interpreted for clarity as a 2×1 real random vector $(\mathrm{Re}(x_k), \mathrm{Im}(x_k))$. Normal stands here for the bivariate normal distribution; its mean is the

2×1 vector $(0, 0)$, also denoted 0, and its 2×2 covariance matrix is the product of the 2×2 identity matrix $\mathbf{1}$ by the (scalar) variance σ^2. In a first approximation, the $\{x_k\}_k$ are assumed to be independent so their mean is also normally distributed

$$I_1^{\text{grain}}(\boldsymbol{r}) = \frac{1}{n}\sum_{k=1}^{n} x_k^{\text{grain}} \sim \text{Normal}\left(0, \frac{1}{n}\sigma^2\mathbf{1}\right), \tag{6.6}$$

where $I_1(\boldsymbol{r})$ is I_1^{TFM}, I_1^{PWI} or another delay-and-sum algorithm. As a consequence, $\left|I_1^{\text{grain}}(\boldsymbol{r})\right|$ is Rayleigh distributed, which was experimentally validated on B-scans [Wag83] and TFM images [Bev18].

The signal in the presence of a defect is modelled as the addition of the deterministic defect response, μ, and the grain noise

$$x_k^{\text{defect}} = \mu + x_k^{\text{grain}}, \tag{6.7}$$

which leads to

$$x_k^{\text{defect}} \sim \text{Normal}\left(\mu, \sigma^2\mathbf{1}\right) \tag{6.8}$$

and

$$I_1^{\text{defect}}(\boldsymbol{r}) = \frac{1}{n}\sum_{k=1}^{n} x_k^{\text{defect}} \sim \text{Normal}\left(\mu, \frac{1}{n}\sigma^2\mathbf{1}\right), \tag{6.9}$$

Note that (i) the variation of the defect response with respect to the angles of the incident and scattered waves, and (ii) the variation of transmission and reflection coefficients at the interfaces, are neglected, which is reasonable for a narrow insonification beam typical in the multi-view immersion inspections studied here. Physically, summing x_k creates a constructive interference of the defect response and a destructive interference of the noise. Note that estimating the parameter μ from the $\{x_k\}$ is known in statistics as the *location problem*; the mean of x_k is an example of a *location estimator*. This last equation shows the image point has a $\sqrt{n}$-times higher Signal-to-Noise amplitude Ratio (SNR) than the time signals. This must be seen as a theoretical upper limit; in practice, the SNR increase is smaller because (1) the time signals are correlated because the probe elements are spatially close to each other, so the $\{x_k\}$ are not truly independent and (2) the variation of defect response may not be negligible ($\mu \neq \mu_k$). Nevertheless, this model illustrates how averaging signals through delay-and-sum imaging improves the SNR up to a certain point. A more important limit, which this chapter aims to address, is that there are other sources of coherent noise than grain noise: other ultrasonic signals have arrival times which may coincide with the delay laws used to image

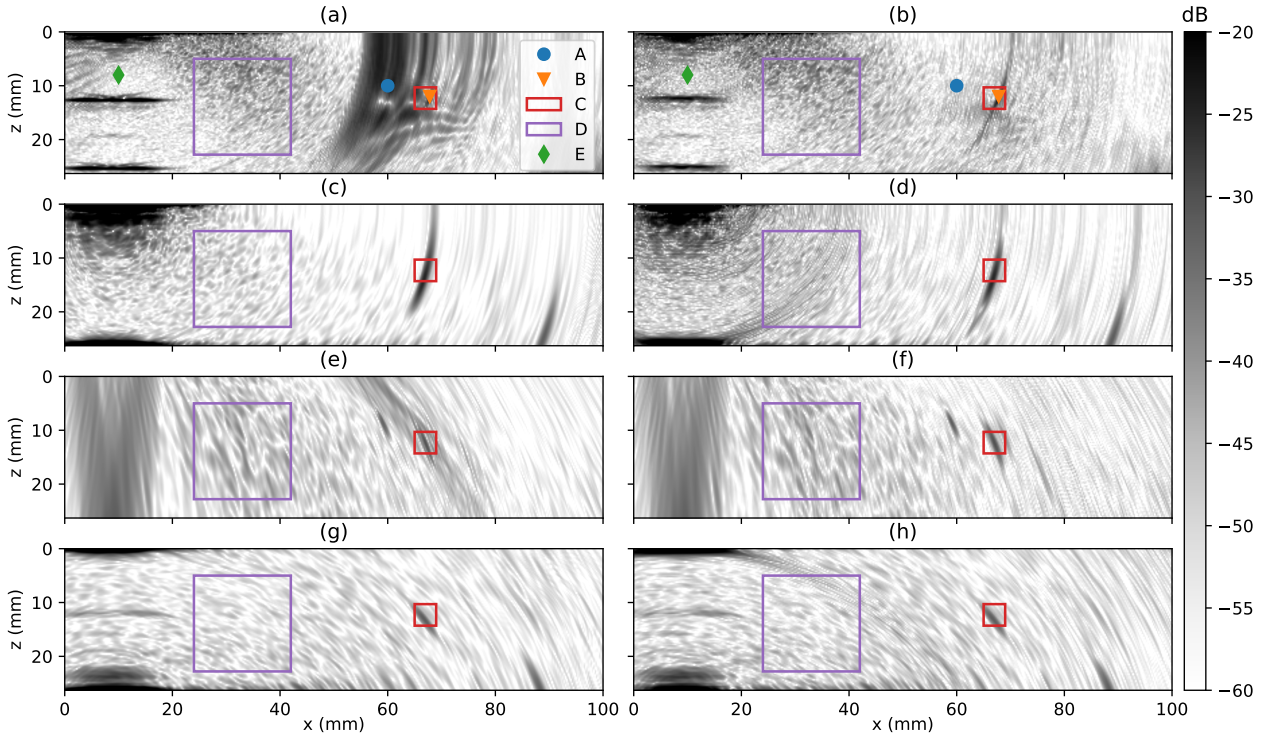

Figure 6.2 – Comparison of TFM images using the mean (left column) and the median (right column). Rows from top to bottom: T–T, L–L, LT–T, LL–LL. Common dB scale, where 0 dB is the peak amplitude of the back wall in (c). An artefact created by the front wall reflection is visible in (a) around point A. square C surrounding the defect is used for signal-to-noise ratio measurement. square D is used for speckle level comparison.

a point; for example, boundary reflections, whose amplitudes may be an order-of-magnitude higher than the defect response or the grain noise. These spurious signals contaminate only a fraction of the $\{x_k\}$, as their physical source is not located at the image point $\boldsymbol{r}$ for which the delay laws are tuned; however, they may have a detrimental effect as illustrated below with experimental data.

6.3.2 Experimental validation and discussion

Consider the inspection configuration presented in fig. 6.1. The 64-element 5-MHz ultrasonic linear array (pitch 0.3 mm) is held above the top surface with an angle of 12°. The distance between the closest probe element and the top surface is 30 mm. The specimen is a 26.3 mm-thick copper block (longitudinal velocity $v_L = 4730\,\mathrm{m\,s^{-1}}$, shear velocity $v_T = 2280\,\mathrm{m\,s^{-1}}$)

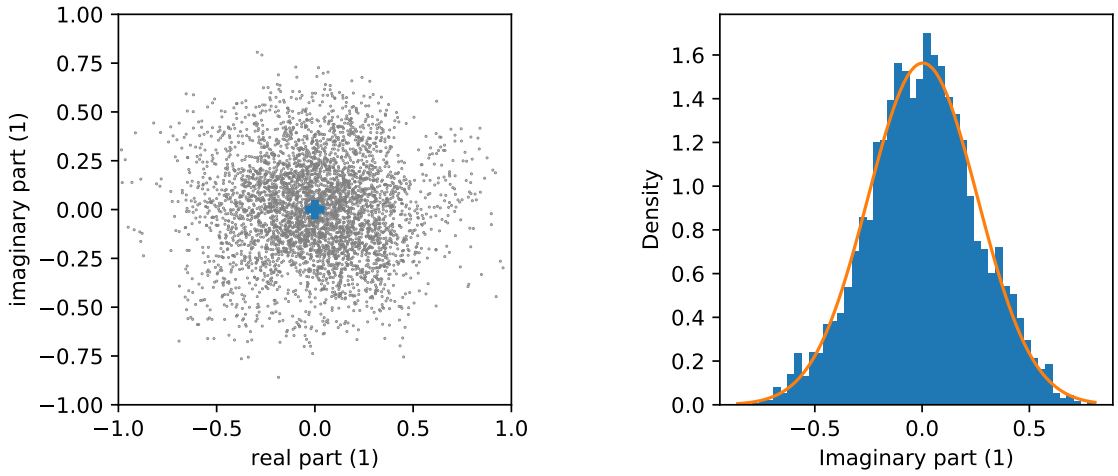

(a) (b)

Figure 6.3 – Ultrasonic data $\{x_k\}$ which contribute to the point E (grain noise) in TFM view T–T. (a) Scatter plot, full range. The blue cross indicates the (0, 0) point. (b) Histogram of the imaginary part and fitted normal distribution.

with a side-drilled hole (SDH) of 2 mm diameter centred at $x = 67$ mm and $z = 12.5$ mm. Figure 6.2 (a, c, e, g) presents multiple TFM images of the sample: the SDH located at point B is clearly identified in the views L–L, LT–T, LL-LL but the artefact located near point A in the view T–T (fig. 6.2a) hinders the detection. This artefact corresponds to the second front wall reflection whose arrival time coincidences partially with the delay laws used in this view. Moving the probe further away from the sample would shift it or make it disappear, however, this solution may not be practical due to limited accessibility. In an inspection using a solid wedge rather than liquid couplant, similar echoes would be created by reflections in the wedge.

Before studying this artefact, the point E is first considered. Point E is virtually pure grain noise as all signals except the front wall echo have greater times of flight. Figure 6.3 presents the ultrasonic data points x_k which contribute to this pixel. The points are scattered in all directions and are approximatively centred on zero; their density decreases with the distance to zero. As shown in fig. 6.3b, the normal distribution, fitted with the sample mean and the sample standard deviation, fits the data very well. So the grain noise model eq. (6.5) appears to accurately explain the observed data. As a consequence, the resulting TFM amplitude, modelled by eq. (6.6), is close to zero, as desired for grain noise.

The ultrasonic data contributing to the artefact are more pathological. Figure 6.4 presents

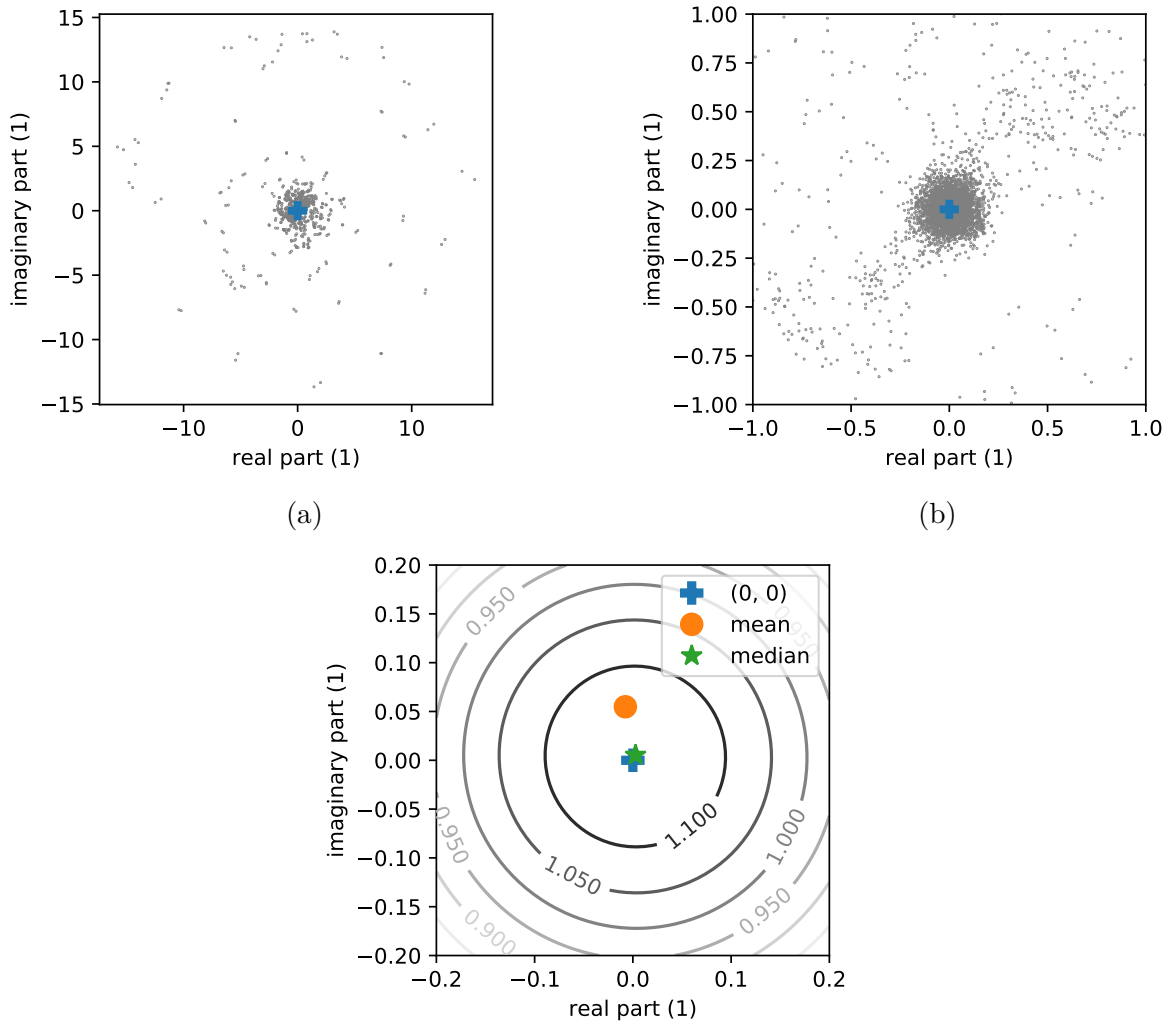

Figure 6.4 – Ultrasonic data $\{x_k\}$ which contribute to the point A (artefact) in TFM view T–T. (a) Scatter plot, full range. (b) Scatter plot, clipped. (c) Contour of the empirical density function, clipped.

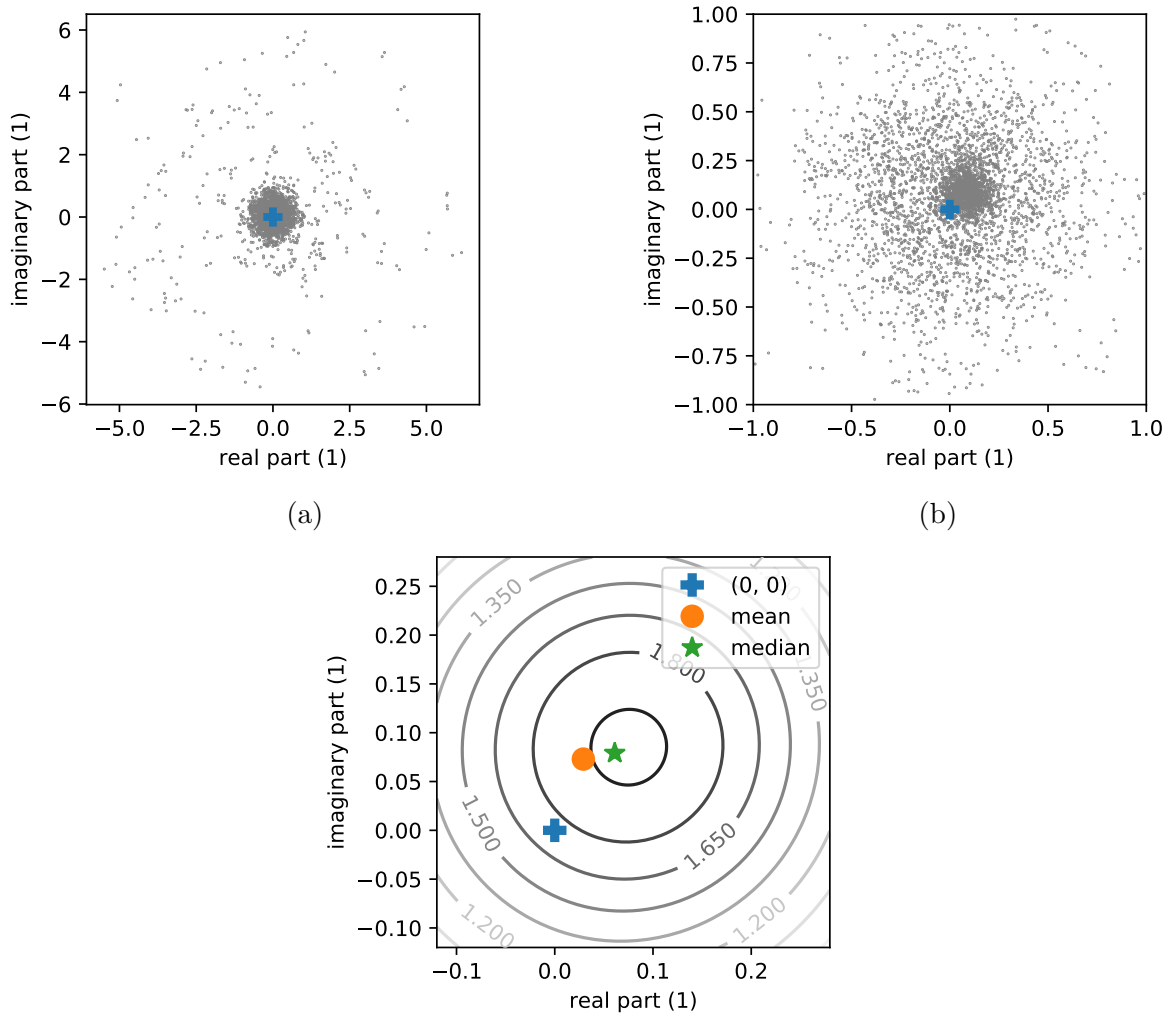

Figure 6.5 – Ultrasonic data $\{x_k\}$ which contribute to the point B (defect) in TFM view T–T. (a) Scatter plot, full range. (b) Scatter plot, clipped. (c) Contour of the empirical density function, clipped.

the points which form pixel A, and their empirical density obtained with kernel density estimation [Sco15]. As for point E, there is a cluster of points spherically distributed around zero in a 0.25 radius, which corresponds to the grain noise. However, there is a halo of points of magnitude up to 16.6 which is left unexplained by the normal distribution: the probability of having points further away than a few standard deviations from the mean is practically zero due to the exponential decay of the density function. This halo is actually caused by the reflection of the front wall of the sample, not by the grain noise. If an image was formed with only the point in the main cluster (magnitude less than 0.25, 78% of the points), the TFM amplitude at this pixel would be 0.0028 (−51 dB), i.e. the grain noise floor; however, including all points leads to an amplitude of 0.055 (−25 dB), which demonstrates the strong influence of the 22% remaining points. As seen in fig. 6.4c, the mean point differs significantly from zero, which ultimately causes the artefact in and near pixel A.

The ultrasonic data points contributing to the defect image (point B) are shown in fig. 6.5. Compared to pixel E, the cloud of points is shifted away from zero, due to the presence of the defect, which is consistent with the signal model introduced earlier (eq. (6.8)). The points have a higher dispersion than for pixel E, likely because the defect response itself is dispersed; this is neglected in the model eq. (6.8), and has little practical importance here. There are also high magnitude points, unexplained by the normal distribution, which may correspond to boundary echoes; contrary to point A, they have little effect here as they are not coherent.

This brief analysis shows that the normal distributions (eqs. (6.5) and (6.8)) are appropriate to model the bulk of the data but not the remaining large spurious signals. A proper probabilistic treatment of them is difficult, yet they cannot be ignored as they may significantly degrade the image. The solution explored in this chapter is to aim to mitigate their influence using robust statistics.

6.4 Robustness/efficiency trade-off

This section presents fundamental results of robust statistics in the univariate case for simplicity, following Tukey [Tuk60], Huber [Hub64] and Maronna, Martin and Yohai [Mar06, chapter 2]. The objective is to obtain an estimate of μ from n measurements $x_k = \mu + \varepsilon_k$, where ε_k is a zero-centred noise. For normally distributed noise $\varepsilon_k \sim \text{Normal}(0, \sigma^2)$, the sample mean

$\sum_{k=1}^{n} x_k/n \sim \text{Normal}(\mu, \sigma^2/n)$ is the optimal estimator in the sense it has the lowest possible asymptotic (i.e. for large n) variance. However, real data is not always that well-behaved; one can consider instead Tukey's contaminated normal distribution, which models the presence of 5% of outliers of higher variance:

$$x_k \sim 0.95\,\text{Normal}(\mu, \sigma^2)) + 0.05\,\text{Normal}(\mu, 100\sigma^2)). \tag{6.10}$$

The mean of n samples of this distribution is $\text{Normal}(\mu, 5.95\sigma^2/n)$. The presence of outliers causes a large increase of the variance of the mean, which statisticians refer to as the *lack of robustness* of the mean. This detrimental effect becomes even higher when the proportion of outliers or their variance increase. The fundamental reason is that the mean minimises $\sum_{k=1}^{n}(x_k - \hat{\mu})^2$, which gives a great influence to large $|x_k - \hat{\mu}|$ due to the square.

An alternative to the mean is the median, which is the value separating the higher half from the lower half of the data. Another characterisation is that the median minimises $\sum_{k=1}^{n} |x_k - \hat{\mu}|$; there is no square in contrast to the mean. The median of n samples is, for large n, $\text{Normal}(\mu, 1.57\sigma^2/n)$ for the normal distribution, and $\text{Normal}(\mu, 1.72\sigma^2/n)$ for the contaminated normal distribution above; the presence of outliers causes only a mild increase (10%) of the variance of the median, which is why it is described as being more robust than the mean. The main drawback is that in absence of outliers (x_k normally distributed), the median has a 57% higher variance than the mean, which statisticians refer to as a *lower efficiency* at the normal distribution. Choosing the mean or the median is essentially a robustness/efficiency trade-off. Although the contaminated normal may not be an accurate model for ultrasonic data, it illustrates how a robust statistic can mitigate the detrimental effect of a limited number of high amplitude signals.

6.5 Geometric median

As seen previously, the delay-and-sum algorithm is essentially the mean of complex data, or equivalently, 2D real vectors. Also, the mean lacks robustness, which makes it a suboptimal estimator in the presence of outliers; this was presented in the previous section in the univariate case but remains true in the bivariate case [Het10, chapter 6]. So one may wish to replace the mean in the delay-and-sum algorithm by a more robust estimator. Massé and Plante compared ten bivariate location estimators with a Monte Carlo study using 26 different noise distributions

and concluded that the geometric median 'clearly stands as the best overall' [Mas03]. The geometric median, also known as the spatial median, L_1 median or L_1 estimator, is defined as the point minimising the Euclidean distance to all data points, that is [Wei09]

$$\text{Median}\,\{x_k : k = 1\,..\,n\} = \arg\min_{x\in\mathbb{R}^2} \sum_{k=1}^{n} \|x_k - x\|_2. \tag{6.11}$$

This extends the univariate median to multiple dimensions as the 1D median minimises the sum of absolute values to all data points ($|\cdot|$ instead of $\|\cdot\|_2$ in eq. (6.11)). Taking the gradient of the sum of distances leads to a second equivalent definition: the geometric median is the solution of $S(x) = 0$ with

$$S(x) = \sum_{k=1}^{n} \frac{x - x_k}{\|x - x_k\|_2}. \tag{6.12}$$

This calls for three remarks, borrowed from the thorough theoretical analysis made by Hettmansperger and McKean [Het10, chapter 6]. First, $S(x)$ is a sum of unit vectors, so the geometric median depends on the direction of the vector $x - x_k$ rather than its magnitude, which explains why the magnitude of individual values has no influence. Second, the geometric median is more robust than the mean but has a lower efficiency for the spherically-symmetric bivariate normal distribution (variance increased by 27%); as in the univariate case, efficiency and robustness are being traded. Third, the geometric median is different from the componentwise median, which is the vector of the univariate medians component by component: the geometric one is invariant by the rotation of the complex plane, whereas the componentwise one is not; the geometric median has also a higher efficiency than the componentwise one for spherical distributions; see also Small [Sma90] for a survey of multidimensional medians.

As an alternative to the classic delay-and-sum imaging algorithm is introduced

$$I_2(\boldsymbol{r}) = \text{Median}\,\{x_k : k = 1\,..\,n\}, \tag{6.13}$$

where x_k corresponds to either TFM (eq. (6.2)) or PWI (eq. (6.4)). The consequences of replacing the mean by the median in imaging are two-fold. First, due to the increased robustness, the noise in the pixels strongly affected by a small number of high amplitude data points will decrease. Second, due to the decreased efficiency, the noise in the pixels non-affected by outlying data points will increase.

The geometric median is calculated numerically as it has no general closed-form expression. Fritz, Filzmoser and Croux compared several algorithms and concluded that a Newton-type

algorithm with a line search provides 'a stable, fast and reliable approach' [Fri10]. The Newton's descent with backtracking line search [Noc06, algorithm 3.1] and analytically calculated Hessian was used in this chapter.

Note that for any strictly positive real $\lambda > 0$:

$$\text{Median}\,\{\lambda x_k\} = \underset{x\in\mathbb{R}^2}{\arg\min} \sum_{k=1}^{n} \|\lambda x_k - x\|_2 = \lambda \underset{x\in\mathbb{R}^2}{\arg\min} \sum_{k=1}^{n} \|\lambda x_k - \lambda x\|_2 \tag{6.14}$$

$$= \lambda \underset{x\in\mathbb{R}^2}{\arg\min}\, \lambda \sum_{k=1}^{n} \|x_k - x\|_2 = \lambda \underset{x\in\mathbb{R}^2}{\arg\min} \sum_{k=1}^{n} \|x_k - x\|_2 \tag{6.15}$$

$$= \lambda\,\text{Median}\,\{x_k\}. \tag{6.16}$$

As a consequence, the median-based imaging algorithm could also be defined as

$$I_3(\boldsymbol{r}) = \text{Median}\,\{n x_k : k = 1\,..\,n\} = n I_2(\boldsymbol{r}) \tag{6.17}$$

to be on the same scale as the original delay-and-sum algorithm based on summation (eqs. (6.1) and (6.3)).

6.6 Results

Figure 6.2 displays the TFM images using the mean and the median for the views T–T, L–L, LT–T and LL-LL. For PWI, the ultrasonic data are derived from the FMC. Different plane wave angles are used depending on the view to ensure a good insonification of the specimen and in particular of the defect. 16 plane waves are used per view. For the direct views, the refracted angles of the plane waves are linearly sampled between 0° and 85° for the plane wave L (used in views L–X and L–XY), and 10° and 85° for T (used in views T–X and T–XY). For the skip paths, the reflected angles of the final leg are linearly sampled between 30° and 60° for LL, 30° and 85° for TL, 10° and 24° for LT, 30° and 60° for TT. Figure 6.6 displays the PWI images using the mean and the median for the views LL–T, L–L, LT–T and LL-LL. Overall the mean and the median aggregation give similar images; the main differences are highlighted in the following section.

6.6.1 Artefacts

In contrast to the classic (mean) TFM view T–T, median TFM is not contaminated by the front wall artefact (fig. 6.2a and b). The amplitude at point A is reduced by 20 dB, reaching

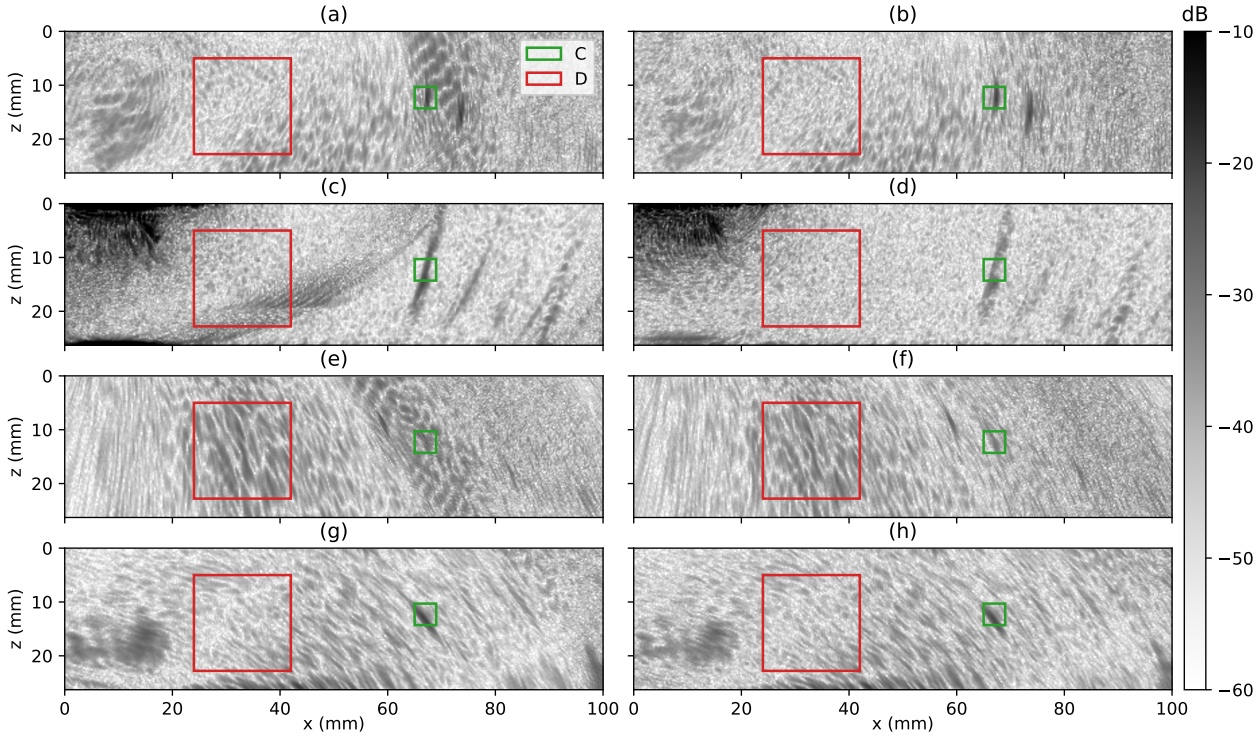

Figure 6.6 – Comparison of PWI images using the mean (left column) and the median (right column). Rows from top to bottom: LL-T, L–L, LT–T, LL–LL. Common dB scale, where 0 dB is the peak amplitude of the back wall in (c). The green square corresponds to the scatterer.

the grain noise floor. This can be visualised in fig. 6.4: the median is closer to 0 than the mean because it is less influenced by the outliers. The suppression of this artefact allows the area underneath to be correctly imaged and makes the scatterer B clearly visible. The same effect is observed to a lesser extent in TFM view LT–T (fig. 6.2e and f). The median does not remove all artefacts: for example, the artefact at $(x = 60, z = 10)$ in the same view, which corresponds to the defect response for the wave mode LL–T, is left untouched because it is caused by a large number of coherent signals.

A drawback of median TFM is the smearing of the back wall as in view L-L (fig. 6.2d) or front wall as in LL-LL (fig. 6.2h). The reason why these artefacts appear in the median image but not the mean one is not understood at this stage.

6.6.2 Noise level

This section compares the noise Root Mean Square (RMS) in the 18×18 mm square D shown in figs. 6.2 and 6.6 for all direct, half-skip and full-skip views in TFM and PWI. This area was chosen to contain mainly speckle noise in TFM views. Redundant TFM views (example: L–T and T–L) were ignored. This leads to 21 TFM views and 36 PWI views.

The noise RMS is increased by median TFM across all views by (1.6 ± 1.3) dB (mean $\pm$ standard deviation). The largest increase is 5.5 dB for the view L–L, caused mainly by the diffraction artefact near the back wall mentioned in the previous section. The overall increase of the speckle noise is consistent with the theoretical loss of efficiency of the median compared to mean discussed in sections 6.4 and 6.5: in the absence of spurious signals which create artefacts, the mean leads to a smaller noise level.

In PWI, the noise level seems dominated by numerous artefacts rather than the speckle, due to the limited number of transmissions. This is a situation where the median is advantageous (increased robustness): the noise RMS in square D is reduced across all views by (0.2 ± 1.8) dB (mean $\pm$ standard deviation); maximum decrease: 6.2 dB; maximum increase: 1.5 dB. The images produced by the median are also noticeably cleaner as artefacts are suppressed; for example, near the scatterer in views LL–T and LL-LL (first and third rows of fig. 6.6).

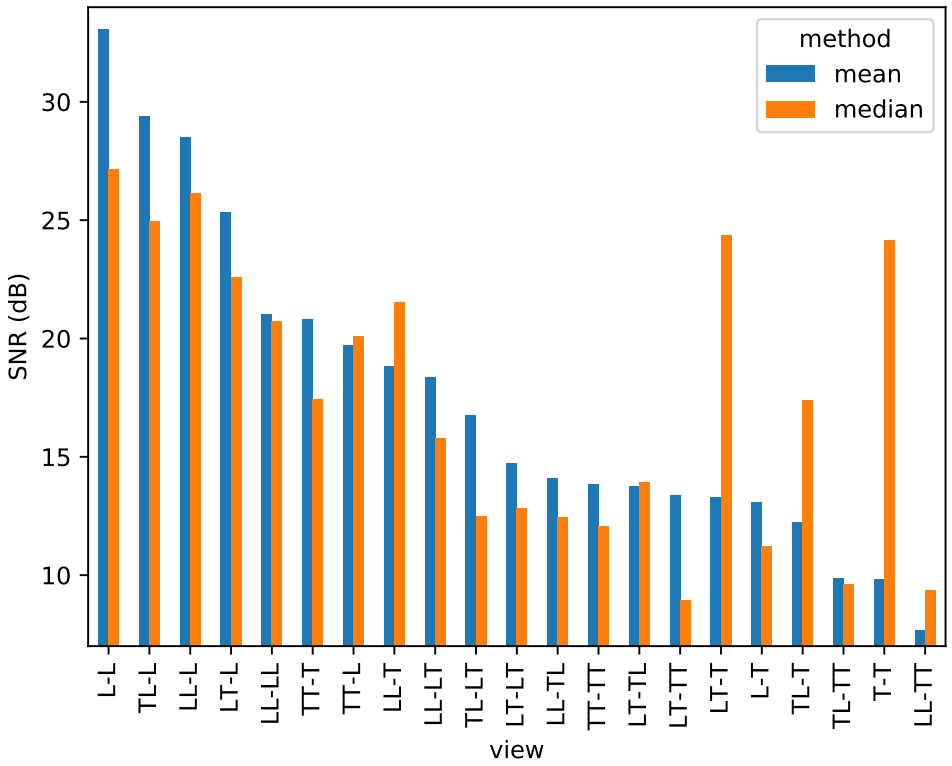

Figure 6.7 – Signal-to-Noise Ratio in TFM views measured in square C in fig. 6.2. Higher is better.

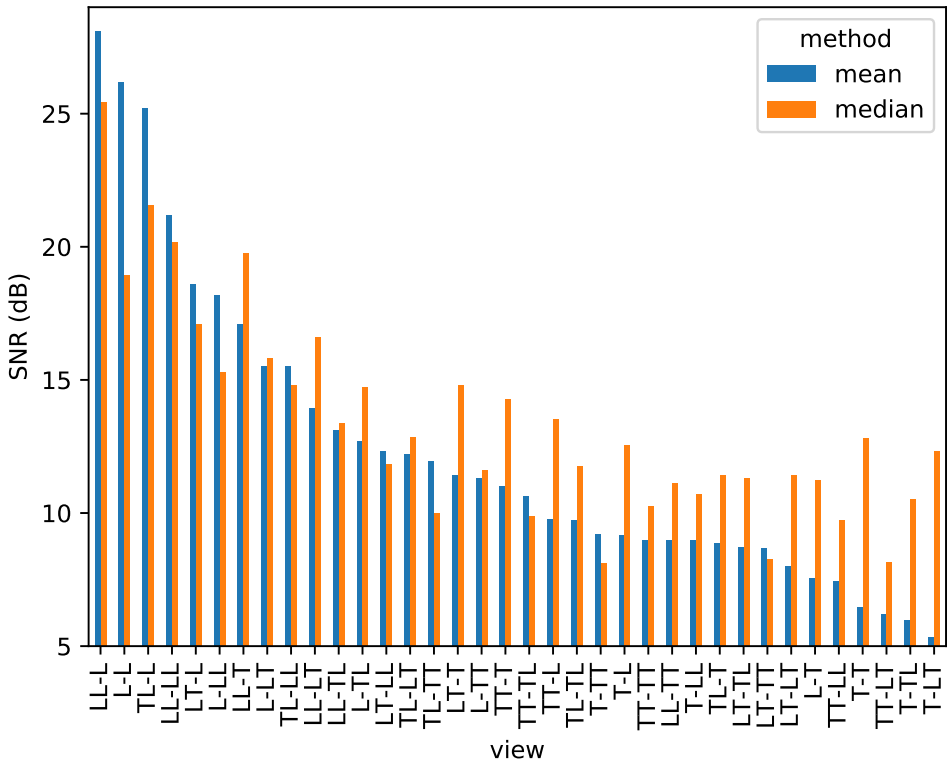

Figure 6.8 – Signal-to-Noise Ratio in PWI views measured in square C in fig. 6.6. Higher is better.

6.6.3 Signal-to-noise ratio

The Signal-to-Noise Ratios (SNR) of the side-drilled hole were measured in the same views as in section 6.6.2. The SNR is defined as the ratio of the maximum image amplitude in the $4 \times 4\,\text{mm}$ square C surrounding the defect by the RMS of pixels in the same area in a (not shown) defect-free acquisition. In the author's opinion, the SNR threshold above which a signal clearly stands out from the noise is around 10 dB; however, it is not a clear cut-off. The SNR is used here as a proxy for detectability, but it is not perfect; in practice, the presence of numerous echoes with high SNR may hinder the unambiguous identification of the defect; this scenario tends to happen for views with relatively low SNR (under 15 dB).

Figure 6.7 shows the SNR for each TFM view sorted by amplitude in the mean case. The signal amplitudes across all views are relatively constant (difference of $(0.8 \pm 1.5)\,\text{dB}$, mean $\pm$ standard deviation); the changes of SNR are mainly explained by a change of noise level. When the noise is dominated by the presence of artefacts, their suppression by the median leads to sharp increase of the SNR, as in T–T (14.3 dB) and LT–T (11.1 dB). When the noise is dominated by the speckle, the noise increases as seen previously, which ultimately decreases the SNR as in view L–L ($-5.9\,\text{dB}$, largest degradation across all views). Overall, the average SNR is almost equal: 17.5 dB for the mean, 17.3 dB for the median.

Figure 6.8 shows the SNR for each PWI view. The average SNR with the median (13.4 dB) is slightly better than with the mean (12.3 dB). The signal amplitudes with the median tend to be smaller (average difference of $-1.3\,\text{dB}$) but the noise level is also lower (average difference of $-2.4\,\text{dB}$) due to the suppression of artefacts. The largest SNR variations in both directions are at the view L–L ($-7.2\,\text{dB}$, fig. 6.6c and d) due mainly to a 5.7 dB decrease of the signal, and at the view T–LT (7.0 dB) due to an artefact suppression.

6.7 Conclusion

Delay-and-sum imaging techniques form images by summing ultrasonic data. Up to a multiplicative constant, this operation is equivalent to calculating the mean of the data. If the defect signal is polluted purely by grain noise that is accurately modelled as normally-distributed additive noise, the mean is optimal for its suppression. However, when accounting for other sources of unwanted image artefacts such as those caused by boundary reflections, the distribu-

tion of the polluting noise is only approximately normal; these high amplitude spurious signals have a large effect on the mean which may ultimately lead to a degradation of the image. Replacing the mean by the more robust geometric median in the imaging algorithm allows the suppression of some artefacts and the recovery of signals underneath. The main drawbacks are the mild increase of the grain noise level due to the lower efficiency of the median for normally distributed data, and additional diffraction artefacts at the ends of some wall echoes. The net effect on the SNR depends mainly on the noise mechanism: in the presence of an artefact, it is preferable to use the median; in the presence of grain noise speckle, it is preferable to use the mean.

This novel imaging approach is philosophically different from the regular delay-and-sum approach as it is justified by a statistical model (the location problem) rather than physical considerations on constructive/destructive interference of waves. It is also non-linear in the ultrasonic data. Contrary to existing artefact filtering methods, it is threshold-free and does not require any prior identification of problematic signals.

Chapter 7

Conclusion

7.1 Review of thesis

This thesis has investigated several areas relevant to multi-view imaging and defect characterisation.

First, in chapter 2, the Full Matrix Capture matrix was shown to closely relate to the transfer matrix of the linear and time-invariant ultrasonic system, which contains all the information possibly measurable by the array. Several techniques were presented to form images from the FMC data, notably multi-view imaging which exploits mode conversions and internal reflections in the specimen.

In order to quantify the defect amplitudes in the different views, a semi-analytical model for immersion inspection was implemented and experimentally validated against a side-drilled hole, a notch and a perfect crack, in chapter 3. A simpler model was derived for even faster computation, by retaining only the defect response at the probe centre frequency, and the pixel amplitude corresponding to the defect centre. This simpler model was used to calculate sensitivity images, which show the predicted TFM amplitudes of a given defect within and across the views. These images could be used to select the views with the highest signal level.

Using this semi-analytical model, a technique to characterise defects based on their multi-view TFM amplitudes was introduced in chapter 4. It has been demonstrated in the literature that defects that are large compared to the point spread function can be characterised by measuring their size on TFM images. However, this technique is not applicable for smaller defects, which are not resolved. To overcome this, the multi-view TFM amplitudes (one value

per view) are used in this thesis as a defect signature, which is compared against a database of ellipses and cracks populated by the ultrasonic model from chapter 3. The uncertainties of the characterisation are handled with a Bayesian framework. The results are the clusters of possible scatterers which are the closest to the unknown defect. The technique was applied to characterise a crack, a side-drilled hole and a notch. The main limitation of this technique is its reliance on an ultrasonic model and an accurate knowledge of the specimen geometry and velocities.

Extending the defect characterisation technique to account for the coherent noise, caused by the material microstructure, requires knowing the probability distribution of the maximum amplitude of the speckle in the image. The literature on this topic is scarce, so a theoretical analysis and numerical studies were undertaken in chapter 5 as a first step. The speckle was modelled as a collection of statistically independent cells, which simplifies the analysis. Several estimates of the speckle cell size were introduced and compared, to ultimately obtain the distribution of the maximum of the speckle, although the practicality of the method remains problematic.

Finally, chapter 6 introduced a variant of delay-and-sum (DAS) imaging where the summation of the signals is replaced by the calculation of their median. Using the standard model of normally distributed structural noise, the regular DAS technique is optimal. However, the noise may strongly deviate from this model due to the presence of wall reflections, causing artefacts in the images. In such case, using the median was experimentally demonstrated to suppress these artefacts.

7.2 Summary of findings

7.2.1 Sensitivity images

The semi-analytical model developed by Schmerr [Sch16] and extended by the current author to multi-view inspection was experimentally demonstrated to be a fast and accurate way to predict TFM amplitudes. The simpler model that was derived, around 3 orders of magnitude faster to run, is also reasonably accurate, and was used to create sensitivity images showing the predicted TFM amplitudes at any location in any view. This makes it a practical tool to help design multi-view TFM inspections.

7.2.2 Defect characterisation

The vector of the peak defect amplitudes in multiple TFM views carries enough information to characterise a 2D small defect, when combined with a reasonably accurate ultrasonic model. This technique makes it possible to determine the approximate shape, size and orientation of flaws which are too small to be well resolved on a TFM image. The probabilistic framework allows the uncertainty of the estimation to be quantified.

7.2.3 Statistics of the speckle

Following the optics and medical ultrasonics literature, the speckle is modelled as a collection of statistically independent cells, which simplifies the analysis. However, the cell size used in these fields is not appropriate for ultrasonic testing, as the target statistics are different, respectively the mean and maximum amplitudes of the speckle. The distribution of the speckle peak amplitudes is appropriately modelled with the MaxRayleigh distribution, parametrised by the cell size, or equivalently, by the effective sample size. This best estimate of this last quantity is the maximum likelihood of the MaxRayleigh distribution, however it is difficult to obtain in practice as it requires many independent samples.

7.2.4 Median-based imaging

Using the median instead of the mean in TFM imaging is an effective strategy to remove some artefacts, leading to large increase of the signal-to-noise ratio. The underlying reason is the lack of robustness of the mean to high amplitudes, as explained by the contaminated normal toy model. The main limits of this median-based approach are the increase of the speckle amplitude level, the decrease of the defect amplitude level.

7.3 Future work

7.3.1 Sensitivity images

Plane Wave Imaging (PWI) inspections require the number of plane waves to use and their angles to be defined. Also, contrarily to the cylindrical waves used in TFM, the plane waves have limited spatial extent. This makes modelling vital for ensuring the specimen is correctly

insonified. It would be interesting to adapt the model of chapter 3 to obtain sensitivity images for PWI inspections.

Another possible future work is extending the sensitivity model to 3D to account for the finite size of defects in the out-of-plane direction.

7.3.2 Defect characterisation

In its current form, the defect characterisation technique does not account for the material microstructural noise level, which may be higher than the defect amplitude in some views. The SNR could be added to the characterisation model in future work. Also, the characterisation of 3D defects could be investigated, provided a suitable ultrasonic model is available. Finally, the characterisation approach developed in this thesis could be compared against the scattering matrix approach developed by Velichko et al. [Vel17]. It could also be beneficial to combine them to account for both the angular variation of the scattering of a defect within individual views, and the multiple scattering modes.

7.3.3 Statistics of the speckle

Several questions in chapter 5 are left unanswered. First, although no reason to believe the conclusions of this study would not hold for real ultrasonic data was identified, this has to be confirmed experimentally. The main difficulty is that the PSF on an ultrasonic image varies spatially; therefore only local statistics from a relatively small number of pixels can be obtained per acquisition; eventually, such experimental work requires numerous acquisitions. By accounting somehow for the PSF spatial variation, a larger part of the image could be exploited to determine the microstructure statistics, which would greatly reduce the number of independent images needed. Second, it would be desirable to obtain more practical estimators of the effective sample size than n_{MaxRayl} and n_{EI}; the review of methods for estimating the extremal index by Ancona-Navarrete could be a starting point [Anc00]. Third, more theoretical work is needed to understand how the PSF and the microstructure relate to the peak amplitude distribution and the effective sample size: do they relate via the autocorrelation function of the speckle, or via a fundamentally different quantity, and how? Fourth, it remains unclear how to model the peak amplitude in the presence of a defect. The concept of independent speckle cells

may provide a possible starting point: the measured peak amplitude could be explained by the combination of one or multiple cells corresponding the deterministic signal contaminated by the stochastic noise (Rayleigh distribution if the noise is multiplicative, Rice distribution if the noise is additive and multiplicative), and the remaining cells corresponding to the grain noise. Such a model would be mathematically tractable; however its relevance has yet to be assessed.

7.3.4 Median-based imaging

It would be interesting to combine both mean-based and median-based images into a hybrid image that would retain the advantages of both approaches; it is yet unclear how to achieve this. Also, other than saying that the noise includes a small fraction of high amplitude outliers, a more precise model for the noise has intentionally not been introduced. For this reason, it is unknown whether the geometric median is the optimal location estimator to recover the scatterer signal. Finally, the use of the median in adaptive imaging could be assessed.

Appendix A

Probe position relative to the inspected object

This appendix describes a technique to determine the position of the probe relative to the inspected object from the pulse-echo ultrasonic signals. Figure A.1 shows the inspection configuration. The objective is to determine the distance between the probe and the object, d_A, and the inclination of the probe, θ.

Suppose that the element A transmits a cylindrical wave in the coupling medium. At the interface, the wave is partially reflected back towards the probe. The ultrasonic path which goes back to A corresponds to the ray A–P–A. The time of arrival, $\mathcal{T}$, of this pulse is measured in the pulse-echo timetrace. Knowing the velocity, c, in the coupling medium, the distance $d_A = |AP|$ is

$$d_A = \frac{\mathcal{T}c}{2} \tag{A.1}$$

Similarly, the distance $d_B = |BQ|$ is determined from the time of arrival of the wall reflection

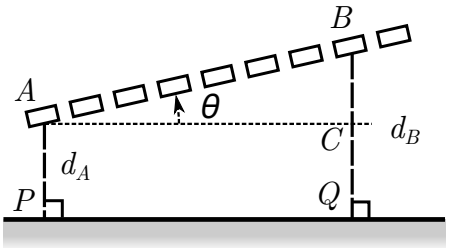

Figure A.1 – The ultrasonic array is held at a distance d from and inclined with an angle θ relative to the top surface of the inspected object.

in the pulse-echo timetrace of element B. The distance $|AB|$ is known as it is part of the probe geometry provided by the manufacturer. Using trigonometry and basic geometry,

$$d_B = |BQ| = |CQ| + |CB| \tag{A.2}$$

$$= d_A + |AB| \sin\theta, \tag{A.3}$$

which gives the angle θ

$$\theta = \arcsin \frac{|BQ| - d_A}{|AB|}. \tag{A.4}$$

d_A and θ can therefore be obtained from the two pulse-echo timetraces, and the velocity of the coupling medium. The precision is improved by repeating the time of arrival measurement for all array elements. In this case, eq. (A.3) is interpreted as a linear model between the inter-element distance $|AB|$ and the distance to the surface, d_B. The ordinary least squares method then gives the terms d_A and $\sin\theta$.

Appendix B

Beam spread

Consider a ultrasonic point source transmitting a cylindrical wave. Because the total energy carried by the wave is constant during the propagation (neglecting material attenuation), then the wave amplitude decreases as the wavefront becomes larger. This change of amplitude, termed beam spread, or geometrical attenuation, is described in the 2D case in this chapter, using elements of the ray theory [Sch15, §2.5]. This appendix was published as part of reference [Bud19].

B.1 Transmitter and scatterer in the same medium.

The beam spread coefficient for the transmit path between the i-th element located at $\boldsymbol{x}_i$ and a scatterer located at $\boldsymbol{y}$ is defined here as:

$$B_i(\boldsymbol{y}) = \sqrt{\frac{1}{\|\boldsymbol{x}_i - \boldsymbol{y}\|}} \tag{B.1}$$

where $\|\cdot\|$ denotes the Euclidean distance. By symmetry the beam spread coefficient for the receive path, $B'_i(\boldsymbol{y})$, is the same.

B.2 Beam spread after one transmission.

We consider a first ray that starts from M_0 in medium 1, intersects the interface at the point M_1 and ends in M_2 in medium 2 after refraction (appendix B.2). The Snell-Descartes law

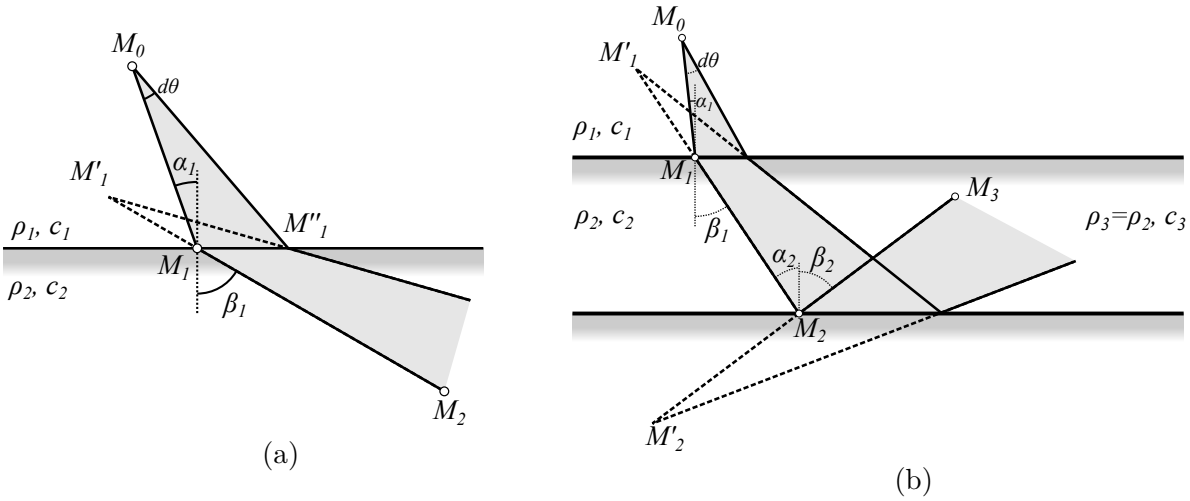

Figure B.1 – (a) Beam spread after one interface. (b) Beam spread after two interfaces.

states that:

$$\frac{\sin\alpha_1}{\sin\beta_1} = \frac{c_1}{c_2}. \tag{B.2}$$

The quantity c_2 is either the longitudinal or the transverse wave speed in medium 2.

A second ray that leaves M_0 with a angle difference of $d\theta$ from the first ray intersects the interface at the point M_1'' and is also transmitted in medium 2 following the Snell-Descartes law. The beam that emerges in medium 2 from the segment M_1M_1'' appears to come from a virtual point source M_1'. Using a first-order approximation for small $d\theta$ and the Snell-Descartes law, it can be shown that [Sch15, B.2]:

$$|M_1'M_1| = \gamma_1|M_0M_1| \tag{B.3}$$

where $|\cdot|$ denotes here the Euclidean distance between two points and where

$$\gamma_1 \coloneqq \frac{c_1\cos^2\beta_1}{c_2\cos^2\alpha_1}. \tag{B.4}$$

The distance between the end point M_2 and the virtual source M_1' is therefore

$$|M_1'M_2| = \gamma_1|M_0M_1| + |M_1M_2| = \gamma_1|M_0M_1| + |M_1M_2|. \tag{B.5}$$

Conservation of energy dictates that the wave amplitude decreases in proportion to the square root of the separation between the rays and hence in inverse proportion to the square root of the distance from the virtual source:

$$B(M_2) = \sqrt{\frac{a}{\gamma_1|M_0M_1| + |M_1M_2|}}. \tag{B.6}$$

The beam spreading coefficient is continuous at the interfaces, as any physical discontinuity of the field is encapsulated in the transmission/reflection coefficient. Therefore

$$\lim_{M_2 \to M_1} B(M_2) = \lim_{|M_1 M_2| \to 0} \sqrt{\frac{a}{\gamma_1 |M_0 M_1| + |M_1 M_2|}} = \sqrt{\frac{a}{\gamma_1 |M_0 M_1|}}. \tag{B.7}$$

Also:

$$\lim_{M_2 \to M_1} B(M_2) = B(M_1) = \sqrt{\frac{1}{|M_0 M_1|}} \tag{B.8}$$

so $a = \gamma_1$. This finally gives the the beam spread coefficient after one transmission for the ray between the element $\boldsymbol{x}_i = M_0$ and the scatterer $\boldsymbol{y} = M_2$ is:

$$B_i(\boldsymbol{y}) = \sqrt{\frac{1}{|M_0 M_1| + |M_1 M_2|/\gamma_1}}. \tag{B.9}$$

By symmetry, the beam spread coefficient for the reverse path is:

$$B_i'(\boldsymbol{y}) = \sqrt{\frac{1}{|M_1 M_2| + |M_0 M_1|/\gamma_1'}} = \sqrt{\frac{1}{|M_1 M_2| + \gamma_1 |M_0 M_1|}} \tag{B.10}$$

where

$$\gamma_1' \coloneqq \frac{c_2 \cos^2 \alpha_1}{c_1 \cos^2 \beta_1} = \frac{1}{\gamma_1}. \tag{B.11}$$

B.3 Beam spread after multiple transmissions or reflections.

The general expression for multiple interfaces can be found recursively from eq. (B.9); the demonstration is left to the reader.

Extending the notations introduced above, α_k is the incident angle at the k-th interface, β_k is the corresponding refracted/reflected angle, $\nu_k \coloneqq c_k / c_{k+1}$ is the k-th refractive index and γ_k is defined as:

$$\gamma_k \coloneqq \nu_k \frac{\cos^2 \beta_k}{\cos^2 \alpha_k} = \frac{\nu_k \cos^2 \beta_k}{1 - \nu_k^2 \sin^2 \beta_k} = \frac{\nu_k^2 - \sin^2 \alpha_k}{\nu_k \cos^2 \alpha_k}.$$

For a n-legged ray ($n-1$ interfaces), the beam spread is:

$$B_i(\boldsymbol{y}) = \left(\sum_{k=0}^{n-1} \frac{|M_k M_{k+1}|}{\prod_{l=1}^{k} \gamma_l} \right)^{-1/2} \tag{B.12}$$

where $\boldsymbol{x}_i = M_0$ is the centre of the i-th array element and the scatterer is $\boldsymbol{y} = M_n$.

Appendix C

Plane wave imaging

The calculation of propagation times in an immersion inspection with plane wave imaging is detailed in this appendix.

C.1 Direct path

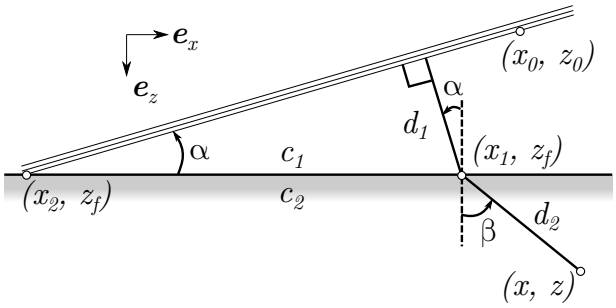

Figure C.1 – Direct path with a plane wave of incident angle α.

Figure C.1 shows the considered geometry. The time of flight of the plane wave between the reference point (x_0, z_0) and the image point (x, z) is

$$\tau = \frac{d_1}{c_1} + \frac{d_2}{c_2}. \tag{C.1}$$

The objective is to express this duration as a function of $x_0, z_0, z_f, \alpha, \beta, c_1$ and c_2. The leg lengths are

$$d_1 = (x_1 - x_2)\sin\alpha, \tag{C.2}$$

$$d_2 = \frac{x - x_1}{\sin\beta}, \tag{C.3}$$

with

$$x_1 = x - (z - z_f)\tan\beta, \tag{C.4}$$

$$x_2 = x_0 - \frac{z_f - z_0}{\tan\alpha}. \tag{C.5}$$

Using Snell's law

$$\frac{\sin\alpha}{c_1} = \frac{\sin\beta}{c_2}, \tag{C.6}$$

the propagation time is after simplification

$$\tau = \frac{(x - x_0)\sin\alpha + (z_f - z_0)\cos\alpha}{c_1} + \frac{(z - z_f)\cos\beta}{c_2}. \tag{C.7}$$

C.2 Skip path

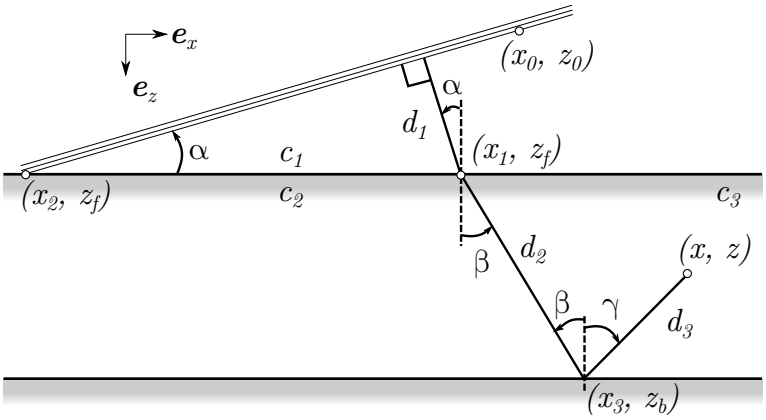

Figure C.2 – Skip path with a plane wave of incident angle α.

Figure C.2 shows the considered geometry. The time of flight of the plane wave between the reference point (x_0, z_0) and the image point (x, z) is

$$\tau = \frac{d_1}{c_1} + \frac{d_2}{c_2} + \frac{d_3}{c_3}. \tag{C.8}$$

Note that in the angle γ is negative in the figure, so by Snell's law

$$\frac{\sin\alpha}{c_1} = \frac{\sin\beta}{c_2} = -\frac{\sin\gamma}{c_3}. \tag{C.9}$$

The leg lengths are respectively

$$d_1 = (x_1 - x_2)\sin\alpha, \tag{C.10}$$

$$d_2 = \frac{z_b - z_f}{\cos\beta}, \tag{C.11}$$

$$d_3 = \frac{z_b - z}{\cos\gamma}, \tag{C.12}$$

with

$$x_3 = x + (z_b - z)\tan\gamma, \tag{C.13}$$

$$x_2 = x_0 - \frac{z_f - z_0}{\tan\alpha}, \tag{C.14}$$

$$x_1 = x_3 - (z_b - z_f)\tan\beta \tag{C.15}$$

$$= x + (z_b - z)\tan\gamma - (z_b - z_f)\tan\beta. \tag{C.16}$$

After simplification, the propagation time is

$$\tau = \frac{(x - x_0)\sin\alpha + (z_f - z_0)\cos\alpha}{c_1} + \frac{(z_b - z_f)\cos\beta}{c_2} + \frac{(z_b - z)\cos\gamma}{c_3} \tag{C.17}$$

C.3 Intersection point with probe plane

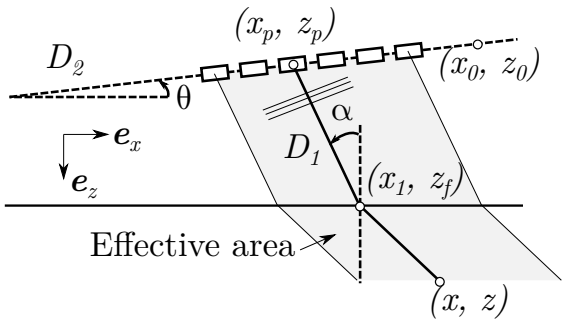

Figure C.3 – Effective area for a probe inclined with angle θ transmitted a plane wave with angle of incidence α.

The propagation times obtained previously implicitly assumed the plane wave is infinitely long. In reality, the plane wave transmitted by the probe is spatially limited by the probe aperture, as shown in fig. C.3. To determine whether an image point is in the effective area, the intersection, denoted (x_p, z_p), of the first leg, D_1, with the probe plane (or line, as the probe is 2D), D_2, is calculated. A parametrisation of the line D_1 with parameter u is

$$\begin{cases} x = x_1 - u\sin\alpha \\ z = z_f - u\cos\alpha \end{cases} \tag{C.18}$$

A parametrisation of the line D_2 with parameter v is

$$\begin{cases} x = x_0 + v\cos\theta \\ z = z_0 - v\sin\theta \end{cases} \tag{C.19}$$

Equating this two systems, eliminating u and solving for v leads to the intersection point

$$v_p = \frac{(x_1 - x_0)\cos\alpha + (z_0 - z_f)\sin\alpha}{\cos\theta\cos\alpha + \sin\theta\sin\alpha} \tag{C.20}$$

$$x_p = x_0 + v_p\cos\theta \tag{C.21}$$

$$z_p = z_0 - v_p\sin\theta \tag{C.22}$$

Appendix D

Probability

This appendix summarises elementary results of the probability theory used throughout this thesis, and sets the notation. The reader is referred to Grinstead and Snell [Gri12], Gut [Gut05], and other classic references for a more complete treatment.

D.1 Probability space

The probability sample space Ω is the set of all possible outcomes. A subset of Ω is called an event. The probability of an event $A \subseteq \Omega$ is denoted $P(A)$; this value is between 0 (impossible event) and 1 (certain event). The probability of the empty event $\emptyset$ is $P(\emptyset) = 0$; the probability of the whole sample space is $P(\Omega) = 1$. The probability of the complementary event of A is $1 - P(A)$.

D.2 Distribution functions of a real-valued random variable

Consider a real-valued random variable $X : \Omega \to \mathbb{R}$. For two reals a and b, it is usual to denote the event $\{\omega \in \Omega : a < X(\omega) \leq b\}$ as "$a < X \leq b$". X is characterised by its cumulative distribution function (CDF) defined as the probability that X is less or equal than a real x:

$$F_X(x) = P(X \leq x). \tag{D.1}$$

F_X is a non-decreasing function, that is for any $a < b$, $F_X(a) \leq F_X(b)$. F_X has the limits

$$\lim_{x \to -\infty} F_X(x) = 0 \tag{D.2}$$

$$\lim_{x \to +\infty} F_X(x) = 1. \tag{D.3}$$

The probability that X is strictly above x, named the survival function, is

$$P(X > x) = 1 - P(X \leq x) = 1 - F_X(x). \tag{D.4}$$

For any reals $a < b$,

$$P(a < X \leq b) = F_X(b) - F_X(a). \tag{D.5}$$

A q-quantile of X, for $q \in [0, 1]$, is a (possibly non-unique) value x so that $F(x) = q$. If F_X is strictly increasing and continuous, the q-quantile of X is unique and is defined as $F^{-1}(q)$, where F_X^{-1} is the inverse function of F_X.

In the general case, F_X is right-continuous, i.e. $\lim_{x \to a, x<a} F_X(x) = F_X(a)$ for any a. If F_X is also left-continuous, then

$$\lim_{x \to a, x<a} F_X(x) = \lim_{x \to a, x>a} F_X(x) = F_X(a). \tag{D.6}$$

In this case, $P(X \leq a) = P(X < a)$, and $P(X = a) = F_X(a) - F_X(a) = 0$.

If X is continuous, the derivative of F_X is termed the probability density function (PDF) and is denoted f_X, so

$$F_X(x) = \int_{-\infty}^{x} f_X(t)\, dt, \tag{D.7}$$

As F_X is non-decreasing, then for any x, $f_X(x) \geq 0$. Integrating f_X gives a probability:

$$P(a < X \leq b) = \int_a^b f_X(t)\, dt. \tag{D.8}$$

In particular,

$$\int_{-\infty}^{+\infty} f_X(t)\, dt = P(\Omega) = 1. \tag{D.9}$$

The expected value of a real-valued continuous distribution is defined as (if it exists)

$$\mathrm{E}(X) = \int_{-\infty}^{+\infty} t f_X(t)\, dt \tag{D.10}$$

For a continuous function $g(X)$,

$$\mathrm{E}(g(X)) = \int_{-\infty}^{+\infty} g(t) f_X(t)\, dt. \tag{D.11}$$

The variance of a distribution is defined as (if it exists) $\mathrm{Var}(X) = \mathrm{E}\{[X - \mathrm{E}(X)]^2\}$.

D.3 Scale and location parameters

Consider a continuous real-valued random variable X_0, which acts in this section as a reference (or standard) variable, for example $X_0 \sim \text{Norm}(0,1)$ (standard normal distribution) or $X_0 \sim \text{Unif}(0,1)$ (standard uniform distribution). One can define a family of random variables parametrised by any real μ and any strictly positive real $\sigma > 0$ as

$$X = \sigma X_0 + \mu. \tag{D.12}$$

μ is termed the location parameter of the distribution of X; σ is the scale parameter. The CDF of X and X_0 are related as follows

$$F_X(x) = P\left(X \leq x\right) = P\left(\sigma X_0 + \mu \leq x\right) = P\left(X_0 \leq \frac{x-\mu}{\sigma}\right) = F_{X_0}\left(\frac{x-\mu}{\sigma}\right). \tag{D.13}$$

By differentiation:

$$f_X(x) = \frac{1}{\sigma} f_{X_0}\left(\frac{x-\mu}{\sigma}\right). \tag{D.14}$$

It is easy to verify that $\text{E}(X) = \sigma\text{E}(X_0) + \mu$ and $\text{Var}(X) = \sigma^2\text{Var}(X_0)$.

The location and scale parameters are a convenient way to parametrise a family of distributions. Extra parameters may still be required, such as the shape parameter in the Student's t-distribution. For the normal distribution, with $X_0 \sim \text{Norm}(0,1)$, the location parameter coincides with the mean of X, and the scale parameter coincides with the standard deviation of X, that is $X \sim \text{Norm}(\mu, \sigma^2)$.

D.4 Joint distribution and conditional probability

Joint distribution Consider two real random variables X and Y of densities $f_X(x)$ and $f_Y(y)$. The *joint* distribution of X and Y is the distribution of the random vector (X, Y), whose CDF is

$$F_{X,Y}(x,y) = P(X \leq x, Y \leq y). \tag{D.15}$$

X and Y are called the *marginal* distributions of (X, Y). In particular,

$$P(X \leq x, Y \leq \infty) = \int_{-\infty}^{x} \int_{-\infty}^{\infty} f_{X,Y}(x', y)\, dx'\, dy. \tag{D.16}$$

Also, as the event "$Y \leq \infty$" is certain,

$$P(X \leq x, Y \leq \infty) = P(X \leq x) = \int_{-\infty}^{x} f_X(x')\, dx'. \tag{D.17}$$

Differentiating by x and equating these two last equations, it follows the marginal density of X is obtained by integrating out Y in the joint density:

$$f_X(x) = \int_{-\infty}^{\infty} f_{X,Y}(x, y)\, dy. \tag{D.18}$$

As any distribution, a joint distribution is uniquely characterised its cumulative function $F_{X,Y}$. However, the marginals of a joint distribution are not sufficient to uniquely characterise it: if $F_{X,Y} = F_{X',Y'}$ then $F_X = F_{X'}$ and $F_Y = F_{Y'}$, but the reciprocal is not true in general. In other words, the joint distribution contains all the information about X and Y, in particular about their dependence, whereas the marginals do not.

Conditional probability Suppose that a sample of (X, Y) is obtained, and that X equals x in this sample. As X and Y may relate, the expectation on the (unknown) sample of Y changes as the sampled value of X is known. The distribution of Y in this sample is called the *conditional* distribution of Y given that $X = x$, of density function

$$f_{Y|X=x}(y) = \frac{f_{X,Y}(x, y)}{f_X(x)}. \tag{D.19}$$

When the context is clear, the notation $f(y \mid x)$ is used for $f_{Y|X=x}(y)$. Figure D.1 illustrates the joint and the conditional distributions: the conditional distribution $f_{Y|X=x}(y)$ is a slice of the joint distribution at $X = x$, up to a multiplicative constant necessary to ensure this defines a proper density function of unit integral. Combining eqs. (D.18) and (D.19) gives the law of total probability for densities

$$f_Y(y) = \int_{-\infty}^{\infty} f_{Y|X=x}(y) f_X(x)\, dx. \tag{D.20}$$

Independence of two random variables X and Y are independent if by definition for all x and y

$$P(X \leq x, Y \leq y) = P(X \leq x)P(Y \leq y), \tag{D.21}$$

or equivalently

$$F_{X,Y}(x, y) = F_X(x)F_Y(y). \tag{D.22}$$

In such case, differentiating by x and y gives

$$f_{X,Y}(x, y) = f_X(x)f_Y(y), \tag{D.23}$$

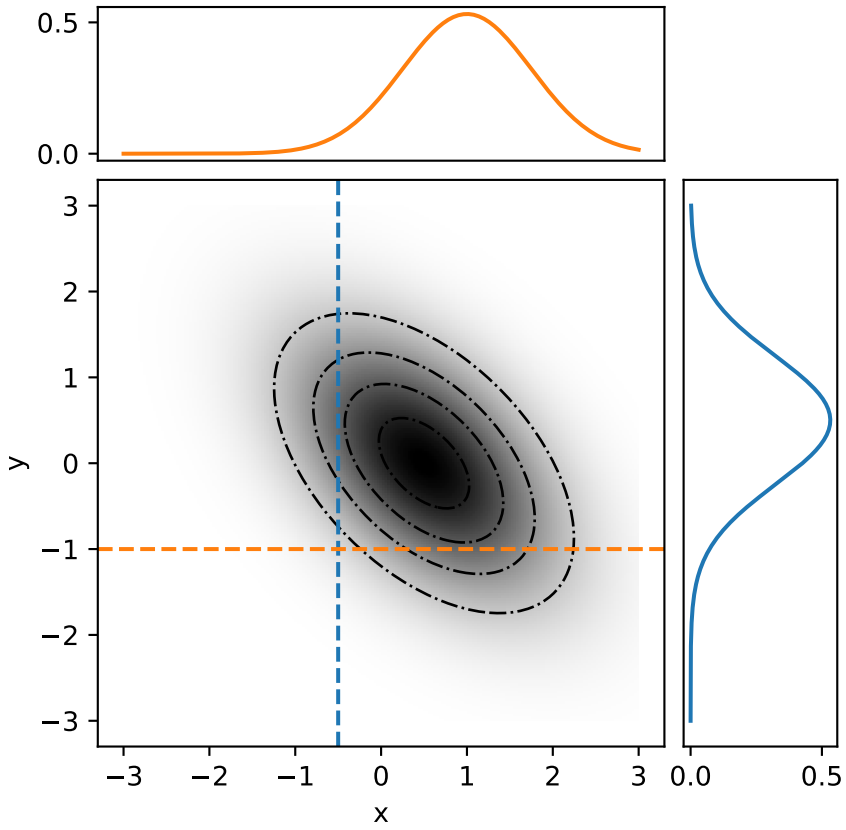

Figure D.1 – Illustration of the joint and conditional distribution of a bivariate normal distribution. Centre panel: joint density $f_{X,Y}$. Top panel: conditional density $f_{X|Y=-1}(x)$. Right panel: conditional density $f_{Y|X=-0.5}(y)$.

and by eq. (D.19)

$$f_{Y|X=x}(y) = \frac{f_{X,Y}(x,y)}{f_X(x)} = \frac{f_X(x)f_Y(y)}{f_X(x)} = f_Y(y). \tag{D.24}$$

So the conditional and unconditional distribution of Y are the same: the fact "$X = x$" does not add any information on Y.

Author's publications

[Bev18] R. L. T. Bevan, J. Zhang, N. Budyn, A. J. Croxford and P. D. Wilcox. 'Experimental Quantification of Noise in Linear Ultrasonic Imaging'. In: *IEEE Transactions on Ultrasonics, Ferroelectrics, and Frequency Control* 66.1 (2018), pp. 79–90. ISSN: 0885-3010. DOI: 10.1109/TUFFC.2018.2874720.

[Bev20] Rhodri L.T. Bevan, Nicolas Budyn, Jie Zhang, Anthony J. Croxford, So Kitazawa and Paul D. Wilcox. 'Data Fusion of Multi-View Ultrasonic Imaging for Characterisation of Large Defects'. In: *IEEE Transactions on Ultrasonics, Ferroelectrics, and Frequency Control* (2020). ISSN: 1525-8955. DOI: 10.1109/TUFFC.2020.3004982.

[Bud19] Nicolas Budyn, Rhodri L. T. Bevan, Jie Zhang, Anthony J. Croxford and Paul D. Wilcox. 'A Model for Multiview Ultrasonic Array Inspection of Small Two-Dimensional Defects'. In: *IEEE transactions on ultrasonics, ferroelectrics, and frequency control* 66.6 (2019), pp. 1129–1139. ISSN: 1525-8955. DOI: 10.1109/TUFFC.2019.2909988. pmid: 30990182.

[Bud20] Nicolas Budyn. 'On the Use of the Geometric Median in Delay-and-Sum Ultrasonic Array Imaging'. In: *IEEE Transactions on Ultrasonics, Ferroelectrics, and Frequency Control* (2020). ISSN: 1525-8955. DOI: 10.1109/TUFFC.2020.2993328.

Bibliography

[Ach73] J D Achenbach. *Wave Propagation in Elastic Solids*. North Holland, 1973. ISBN: 978-0-7204-0325-1.

[Amm13] Habib Ammari, Josselin Garnier, Wenjia Jing, Hyeonbae Kang, Mikyoung Lim, Knut Sølna and Han Wang. *Mathematical and Statistical Methods for Multistatic Imaging*. Vol. 2098. Lecture Notes in Mathematics. Cham: Springer International Publishing, 2013. ISBN: 978-3-319-02584-1.

[Anc00] Miguel A. Ancona-Navarrete and Jonathan A. Tawn. 'A Comparison of Methods for Estimating the Extremal Index'. In: *Extremes* 3.1 (1st Mar. 2000), pp. 5–38. ISSN: 1572-915X. DOI: 10.1023/A:1009993419559.

[ASM19] ASME. *BPCV-V Boiler and Pressure Vessel Code Section V-Nondestructive Examination*. American Society of Mechanical Engineers, 2019.

[AST13] ASTM. *Standard Guide for Planar Flaw Height Sizing by Ultrasonics*. ASTM E2191-13. ASTM International, 2013.

[AST14] ASTM. *E2700-14 Standard Practice for Contact Ultrasonic Testing of Welds Using Phased Arrays*. ASTM International, 2014.

[Aul79] B. A. Auld. 'General Electromechanical Reciprocity Relations Applied to the Calculation of Elastic Wave Scattering Coefficients'. In: *Wave Motion* 1.1 (1st Jan. 1979), pp. 3–10. ISSN: 0165-2125. DOI: 10.1016/0165-2125(79)90020-9.

[Aza00] L. Azar, Y. Shi and S. -C. Wooh. 'Beam Focusing Behavior of Linear Phased Arrays'. In: *NDT & E International* 33.3 (1st Apr. 2000), pp. 189–198. ISSN: 0963-8695. DOI: 10.1016/S0963-8695(99)00043-2.

[Bai15a] L. Bai, A. Velichko and B. W. Drinkwater. 'Characterization of Defects Using Ultrasonic Arrays: A Dynamic Classifier Approach'. In: *IEEE Transactions on Ultrasonics, Ferroelectrics, and Frequency Control* 62.12 (Dec. 2015), pp. 2146–2160. ISSN: 0885-3010. DOI: 10.1109/TUFFC.2015.007334.

[Bai15b] L. Bai, A. Velichko and B. W. Drinkwater. 'Ultrasonic Characterization of Crack-like Defects Using Scattering Matrix Similarity Metrics'. In: *IEEE Transactions on Ultrasonics, Ferroelectrics, and Frequency Control* 62.3 (Mar. 2015), pp. 545–559. ISSN: 0885-3010. DOI: 10.1109/TUFFC.2014.006848.

[Bai19] L. Bai, A. Velichko and B. W. Drinkwater. 'Grain Scattering Noise Modelling and Its Use in the Detection and Characterisation of Defects Using Ultrasonic Arrays'. In: *IEEE Transactions on Ultrasonics, Ferroelectrics, and Frequency Control* (2019), pp. 1–1. ISSN: 0885-3010. DOI: 10.1109/TUFFC.2019.2927439.

[Ban13] S Bannouf, S Robert, O Casula and C Prada. 'Data Set Reduction for Ultrasonic TFM Imaging Using the Effective Aperture Approach and Virtual Sources'. In: *Journal of Physics: Conference Series* 457 (1st Aug. 2013), p. 012007. ISSN: 1742-6596. DOI: 10.1088/1742-6596/457/1/012007.

[Ben81] Ari Ben-Menahem and Sarva Jit Singh. *Seismic Waves and Sources*. New York, NY: Springer New York, 1981. ISBN: 978-1-4612-5858-2.

[Bev18] R. L. T. Bevan, J. Zhang, N. Budyn, A. J. Croxford and P. D. Wilcox. 'Experimental Quantification of Noise in Linear Ultrasonic Imaging'. In: *IEEE Transactions on Ultrasonics, Ferroelectrics, and Frequency Control* 66.1 (2018), pp. 79–90. ISSN: 0885-3010. DOI: 10.1109/TUFFC.2018.2874720.

[Bis06] Christopher M. Bishop. *Pattern Recognition and Machine Learning (Information Science and Statistics)*. Berlin, Heidelberg: Springer-Verlag, 2006. ISBN: 0-387-31073-8.

[Ble00] Norman Bleistein, N. Bleistein and J. K. Cohen. *Mathematics of Multidimensional Seismic Imaging, Migration, and Inversion*. 2001 edition. New York: Springer, 15th Dec. 2000. 544 pp. ISBN: 978-0-387-95061-7.

[Bor02] Liliana Borcea, George Papanicolaou, Chrysoula Tsogka and James Berryman. 'Imaging and Time Reversal in Random Media'. In: *Inverse Problems* 18.5 (2002), p. 1247. ISSN: 0266-5611. DOI: 10.1088/0266-5611/18/5/303.

[Bra00] Ronald Bracewell. *The Fourier Transform and Its Applications*. 3rd ed. McGraw-Hill Series in Electrical and Computer Engineering. Circuits and Systems. McGraw Hill, 2000. ISBN: 978-0-07-303938-1.

[Bro98] Stephen P. Brooks and Andrew Gelman. 'General Methods for Monitoring Convergence of Iterative Simulations'. In: *Journal of Computational and Graphical Statistics* 7.4 (1st Dec. 1998), pp. 434–455. ISSN: 1061-8600. DOI: 10.1080/10618600.1998.10474787.

[Bud18] Nicolas Budyn, Rhodri Bevan, Anthony J. Croxford, Jie Zhang, Paul D. Wilcox, Artem Kashubin and Peter Cawley. 'Sensitivity Images for Multi-View Ultrasonic Array Inspection'. In: *AIP Conference Proceedings* 1949.1 (20th Apr. 2018), p. 080001. ISSN: 0094-243X. DOI: 10.1063/1.5031558.

[Bud19] Nicolas Budyn, Rhodri L. T. Bevan, Jie Zhang, Anthony J. Croxford and Paul D. Wilcox. 'A Model for Multiview Ultrasonic Array Inspection of Small Two-Dimensional Defects'. In: *IEEE transactions on ultrasonics, ferroelectrics, and frequency control* 66.6 (2019), pp. 1129–1139. ISSN: 1525-8955. DOI: 10.1109/TUFFC.2019.2909988. pmid: 30990182.

[Bud20] Nicolas Budyn. 'On the Use of the Geometric Median in Delay-and-Sum Ultrasonic Array Imaging'. In: *IEEE Transactions on Ultrasonics, Ferroelectrics, and Frequency Control* (2020). ISSN: 1525-8955. DOI: 10.1109/TUFFC.2020.2993328.

[Bur78] Christoph B. Burckhardt. 'Speckle in Ultrasound B-Mode Scans'. In: *IEEE Transactions on Sonics and Ultrasonics* 25.1 (Jan. 1978), pp. 1–6. ISSN: 0018-9537, 2162-1403. DOI: 10.1109/T-SU.1978.30978.

[Cap69] J. Capon. 'High-Resolution Frequency-Wavenumber Spectrum Analysis'. In: *Proceedings of the IEEE* 57.8 (Aug. 1969), pp. 1408–1418. ISSN: 1558-2256. DOI: 10.1109/PROC.1969.7278.

[Car17a] E. Carcreff, N. Laroche, D. Braconnier, A. Duclos and S. Bourguignon. 'Improvement of the Total Focusing Method Using an Inverse Problem Approach'. In: *2017 IEEE International Ultrasonics Symposium (IUS)*. 2017 IEEE International Ultrasonics Symposium (IUS). Sept. 2017, pp. 1–4. DOI: 10.1109/ULTSYM.2017.8092258.

[Car17b] Bob Carpenter, Andrew Gelman, Matthew D. Hoffman, Daniel Lee, Ben Goodrich, Michael Betancourt, Marcus Brubaker, Jiqiang Guo, Peter Li and Allen Riddell. 'Stan: A Probabilistic Programming Language'. In: *Journal of Statistical Software* 76.1 (1st Jan. 2017). ISSN: 1548-7660. DOI: 10.18637/jss.v076.i01.

[Cha15] Sylvain Chatillon, Sébastien Robert, Philippe Brédif, Pierre Calmon, Guillaume Daniel and François Cartier. 'Results of the 2014 UT Modeling Benchmark Obtained with Models Implemented in CIVA: Solution of the FMC-TFM Ultrasonic Benchmark Problem Using CIVA'. In: *AIP Conference Proceedings* 1650.1 (31st Mar. 2015), pp. 1847–1855. ISSN: 0094-243X. DOI: 10.1063/1.4914810.

[Che01] Margaret Cheney. 'The Linear Sampling Method and the MUSIC Algorithm'. In: *Inverse Problems* 17.4 (2001), p. 591. ISSN: 0266-5611. DOI: 10.1088/0266-5611/17/4/301.

[Che09] Margaret Cheney and Brett Borden. *Fundamentals of Radar Imaging*. Vol. 79. Siam, 2009.

[Che98] Chi-Tsong Chen. *Linear System Theory and Design*. Oxford University Press, Inc., 1998.

[Che99] Ming-Hui Chen and Qi-Man Shao. 'Monte Carlo Estimation of Bayesian Credible and HPD Intervals'. In: *Journal of Computational and Graphical Statistics* 8.1 (1999), pp. 69–92. ISSN: 1061-8600. DOI: 10.2307/1390921. JSTOR: 1390921.

[Col01] Stuart Coles, Joanna Bawa, Lesley Trenner and Pat Dorazio. *An Introduction to Statistical Modeling of Extreme Values*. Vol. 208. Springer, 2001.

[Cru17] J. F. Cruza, J. Camacho and C. Fritsch. 'Plane-Wave Phase-Coherence Imaging for NDE'. In: *NDT & E International* 87 (1st Apr. 2017), pp. 31–37. ISSN: 0963-8695. DOI: 10.1016/j.ndteint.2017.01.005.

[Dav03] Herbert Aron David and Haikady Navada Nagaraja. *Order Statistics*. Wiley Online Library, 2003.

[De 07] Laurens De Haan and Ana Ferreira. *Extreme Value Theory: An Introduction*. Springer Science & Business Media, 2007.

[Dev00] A. J. Devaney. 'Super-Resolution Processing of Multi-Static Data Using Time Reversal and MUSIC'. 2000.

[Dev05] A. J. Devaney. 'Time Reversal Imaging of Obscured Targets from Multistatic Data'. In: *IEEE Transactions on Antennas and Propagation* 53.5 (May 2005), pp. 1600–1610. ISSN: 0018-926X. DOI: 10.1109/TAP.2005.846723.

[Doc86] S. R. Doctor, T. E. Hall and L. D. Reid. 'SAFT — the Evolution of a Signal Processing Technology for Ultrasonic Testing'. In: *NDT International* 19.3 (1st June 1986), pp. 163–167. ISSN: 0308-9126. DOI: 10.1016/0308-9126(86)90105-7.

[Dri06] Bruce W. Drinkwater and Paul D. Wilcox. 'Ultrasonic Arrays for Non-Destructive Evaluation: A Review'. In: *NDT & E International* 39.7 (Oct. 2006), pp. 525–541. ISSN: 0963-8695. DOI: 10.1016/j.ndteint.2006.03.006.

[Dru07] Pierre Druilhet and Jean-Michel Marin. 'Invariant HPD Credible Sets and MAP Estimators'. In: *Bayesian Analysis* 2.4 (Dec. 2007), pp. 681–691. ISSN: 1936-0975, 1931-6690. DOI: 10.1214/07-BA227.

[Du09] Lin Du, Tarik Yardibi, Jian Li and Petre Stoica. 'Review of User Parameter-Free Robust Adaptive Beamforming Algorithms'. In: *Digital Signal Processing* 19.4 (1st July 2009), pp. 567–582. ISSN: 1051-2004. DOI: 10.1016/j.dsp.2009.02.001.

[Duc79] Claude E. Duchon. 'Lanczos Filtering in One and Two Dimensions'. In: *Journal of Applied Meteorology* 18.8 (1st Aug. 1979), pp. 1016–1022. ISSN: 0021-8952. DOI: 10.1175/1520-0450(1979)018<1016:LFIOAT>2.0.CO;2.

[Eng11] Marcus Engholm, Tadeusz Stepinski and Tomas Olofsson. 'Imaging and Suppression of Lamb Modes Using Adaptive Beamforming'. In: *Smart Materials and Structures* 20.8 (July 2011), p. 085024. ISSN: 0964-1726. DOI: 10.1088/0964-1726/20/8/085024.

[Fan14] Chengguang Fan, Mihai Caleap, Mengchun Pan and Bruce W. Drinkwater. 'A Comparison between Ultrasonic Array Beamforming and Super Resolution Imaging Algorithms for Non-Destructive Evaluation'. In: *Ultrasonics* 54.7 (Sept. 2014), pp. 1842–1850. ISSN: 0041-624X. DOI: 10.1016/j.ultras.2013.12.012.

[Fel14] Maria V. Felice, Alexander Velichko and Paul D. Wilcox. 'Accurate Depth Measurement of Small Surface-Breaking Cracks Using an Ultrasonic Array Post-Processing Technique'. In: *NDT & E International* 68 (Supplement C 1st Dec. 2014), pp. 105–112. ISSN: 0963-8695. DOI: 10.1016/j.ndteint.2014.08.004.

[Fel18] Maria V. Felice and Zheng Fan. 'Sizing of Flaws Using Ultrasonic Bulk Wave Testing: A Review'. In: *Ultrasonics* 88 (1st Aug. 2018), pp. 26–42. ISSN: 0041-624X. DOI: 10.1016/j.ultras.2018.03.003.

[Fel95] P. Fellinger, R. Marklein, K. J. Langenberg and S. Klaholz. 'Numerical Modeling of Elastic Wave Propagation and Scattering with EFIT — Elastodynamic Finite Integration Technique'. In: *Wave Motion*. Honor and Memory of Julius Miklowitz 21.1 (1st Feb. 1995), pp. 47–66. ISSN: 0165-2125. DOI: 10.1016/0165-2125(94)00040-C.

[Fid10] A. Fidahoussen, P. Calmon, M. Lambert, S. Paillard and S. Chatillon. 'Imaging of Defects in Several Complex Configurations by Simulation-helped Processing of Ultrasonic Array Data'. In: *AIP Conference Proceedings*. Review of Progress in Quantitative Nondestructive Evaluation. Vol. 1211. AIP Publishing, 22nd Feb. 2010, pp. 847–854. DOI: 10.1063/1.3362502.

[Fid12] Alex Fidahoussen. 'Développement d'une Méthode de Reconstruction Ultrasonore Pour La Localisation et La Caractérisation de Défauts'. Paris 11, 21st Sept. 2012.

[Fin92] M. Fink. 'Time Reversal of Ultrasonic Fields. I. Basic Principles'. In: *IEEE Transactions on Ultrasonics, Ferroelectrics, and Frequency Control* 39.5 (Sept. 1992), pp. 555–566. ISSN: 1525-8955. DOI: 10.1109/58.156174.

[For11] Catherine Forbes, Merran Evans, Nicholas Hastings and Brian Peacock. *Statistical Distributions*. John Wiley & Sons, 2011.

[For12] F. Foroozan and S. ShahbazPanahi. 'MUSIC-Based Array Imaging in Multi-Modal Ultrasonic Non-Destructive Testing'. In: *2012 IEEE 7th Sensor Array and Multichannel Signal Processing Workshop (SAM)*. 2012 IEEE 7th Sensor Array and Multichannel Signal Processing Workshop (SAM). June 2012, pp. 529–532. DOI: 10.1109/SAM.2012.6250557.

[Fos83] D. R. Foster, M. Arditi, F. S. Foster, M. S. Patterson and J. W. Hunt. 'Computer Simulations of Speckle in B-Scan Images'. In: *Ultrasonic Imaging* 5.4 (1st Oct. 1983), pp. 308–330. ISSN: 0161-7346.

[Fri10] Heinrich Fritz, Peter Filzmoser and Christophe Croux. 'A Comparison of Algorithms for the Multivariate L1-Median'. In: *Computational Statistics* 27 (11th Oct. 2010), pp. 1–18. DOI: 10.1007/s00180-011-0262-4.

[Gar13] D. Garcia, L. L. Tarnec, S. Muth, E. Montagnon, J. Porée and G. Cloutier. 'Stolt's f-k Migration for Plane Wave Ultrasound Imaging'. In: *IEEE Transactions on Ultrasonics, Ferroelectrics, and Frequency Control* 60.9 (Sept. 2013), pp. 1853–1867. ISSN: 0885-3010. DOI: 10.1109/TUFFC.2013.2771.

[Gel13] Andrew Gelman, John B. Carlin, Hal S. Stern, David B. Dunson, Aki Vehtari and Donald B. Rubin. *Bayesian Data Analysis*. Third. CRC Press, 1st Nov. 2013. 677 pp. ISBN: 978-1-4398-4095-5. Google Books: ZXL6AQAAQBAJ.

[Gel92] Andrew Gelman and Donald B. Rubin. 'Inference from Iterative Simulation Using Multiple Sequences'. In: *Statistical Science* 7.4 (Nov. 1992), pp. 457–472. ISSN: 0883-4237, 2168-8745. DOI: 10.1214/ss/1177011136.

[Gil06] C. Gilmore, I. Jeffrey and J. LoVetri. 'Derivation and Comparison of SAR and Frequency-Wavenumber Migration within a Common Inverse Scalar Wave Problem Formulation'. In: *IEEE Transactions on Geoscience and Remote Sensing* 44.6 (June 2006), pp. 1454–1461. DOI: 10.1109/TGRS.2006.870402.

[Glu06] Evgeny Glushkov, Natalia Glushkova, Alexander Ekhlakov and Elena Shapar. 'An Analytically Based Computer Model for Surface Measurements in Ultrasonic Crack Detection'. In: *Wave Motion* 43.6 (1st June 2006), pp. 458–473. ISSN: 0165-2125. DOI: 10.1016/j.wavemoti.2006.03.002.

[Goo75] Joseph W Goodman. 'Statistical Properties of Laser Speckle Patterns'. In: *Laser Speckle and Related Phenomena*. Springer, 1975, pp. 9–75.

[Gre15] Peter J. Green, Krzysztof Łatuszyński, Marcelo Pereyra and Christian P. Robert. 'Bayesian Computation: A Summary of the Current State, and Samples Backwards and Forwards'. In: *Statistics and Computing* 25.4 (1st July 2015), pp. 835–862. ISSN: 0960-3174, 1573-1375. DOI: 10.1007/s11222-015-9574-5.

[Gri12] Charles Miller Grinstead and James Laurie Snell. *Introduction to Probability*. American Mathematical Soc., 2012.

[Gut05] Allan Gut. *Probability: A Graduate Course*. Springer Texts in Statistics. Springer, 2005. ISBN: 978-0-387-22833-4.

[Hay09] Michael P. Hayes and Peter T. Gough. 'Synthetic Aperture Sonar: A Review of Current Status'. In: *IEEE Journal of Oceanic Engineering* 34.3 (July 2009), pp. 207–224. ISSN: 2373-7786. DOI: 10.1109/JOE.2009.2020853.

[Hel14] Leonhard Held and Daniel Sabanés Bové. *Applied Statistical Inference: Likelihood and Bayes*. Berlin Heidelberg: Springer-Verlag, 2014. ISBN: 978-3-642-37886-7.

[Het10] Thomas P Hettmansperger and Joseph W McKean. *Robust Nonparametric Statistical Methods*. CRC Press, 2010.

[Hof14] Matthew D. Hoffman and Andrew Gelman. 'The No-U-Turn Sampler: Adaptively Setting Path Lengths in Hamiltonian Monte Carlo'. In: *Journal of Machine Learning Research* 15 (2014), pp. 1593–1623.

[Hol05] Caroline Holmes, Bruce W. Drinkwater and Paul D. Wilcox. 'Post-Processing of the Full Matrix of Ultrasonic Transmit–Receive Array Data for Non-Destructive Evaluation'. In: *NDT & E International* 38.8 (Dec. 2005), pp. 701–711. ISSN: 0963-8695. DOI: 10.1016/j.ndteint.2005.04.002.

[Hub64] Peter J. Huber. 'Robust Estimation of a Location Parameter'. In: *The Annals of Mathematical Statistics* 35.1 (Mar. 1964), pp. 73–101. ISSN: 0003-4851, 2168-8990. DOI: 10.1214/aoms/1177703732.

[Hun08] A. J. Hunter, B. W. Drinkwater and P. D. Wilcox. 'The Wavenumber Algorithm for Full-Matrix Imaging Using an Ultrasonic Array'. In: *IEEE Transactions on Ultrasonics, Ferroelectrics, and Frequency Control* 55.11 (Nov. 2008), pp. 2450–2462. ISSN: 0885-3010. DOI: 10.1109/TUFFC.952.

[Hut14] Peter Huthwaite. 'Accelerated Finite Element Elastodynamic Simulations Using the GPU'. In: *Journal of Computational Physics* 257 (15th Jan. 2014), pp. 687–707. ISSN: 0021-9991. DOI: 10.1016/j.jcp.2013.10.017.

[Hyn96] Rob J. Hyndman. 'Computing and Graphing Highest Density Regions'. In: *The American Statistician* 50.2 (1st May 1996), pp. 120–126. ISSN: 0003-1305. DOI: 10.1080/00031305.1996.10474359.

[Iak14] Ekaterina Iakovleva, Sylvain Chatillon, Philippe Bredif and Steve Mahaut. 'Multi-Mode TFM Imaging with Artifacts Filtering Using CIVA UT Forwards Models'. In: American Institute of Physics Conference Series. Vol. 1581. 1st Feb. 2014, pp. 72–79. DOI: 10.1063/1.4864804.

[ISO19] ISO. *Non-Destructive Testing of Welds — Ultrasonic Testing — Use of Automated Phased Array Technology*. ISO 13588:2019. Geneva, CH: International Organization for Standardization, 2019.

[ISO20a] ISO. *Non-Destructive Testing — Ultrasonic Testing — General Use of Full Matrix Capture / Total Focusing Technique (FMC/TFM)*. ISO/DIS 23865. Geneva, CH: International Organization for Standardization, 2020.

[ISO20b] ISO. *Non-destructive Testing of Welds — Ultrasonic Testing — Use of (Semi-) Automated Full Matrix Capture / Total Focusing Technique (FMC/TFM)*. ISO/DIS 23864. Geneva, CH: International Organization for Standardization, 2020.

[Jak76] E. Jakeman and P. Pusey. 'A Model for Non-Rayleigh Sea Echo'. In: *IEEE Transactions on Antennas and Propagation* 24.6 (Nov. 1976), pp. 806–814. ISSN: 0018-926X, 1558-2221. DOI: 10.1109/TAP.1976.1141451.

[Jef92] William H. Jefferys and James O. Berger. 'Ockham's Razor and Bayesian Analysis'. In: *American Scientist* 80.1 (1992), pp. 64–72. ISSN: 0003-0996. JSTOR: 29774559.

[Jen06] Jørgen Arendt Jensen, Svetoslav Ivanov Nikolov, Kim Løkke Gammelmark and Morten Høgholm Pedersen. 'Synthetic Aperture Ultrasound Imaging'. In: *Ultrasonics*. Proceedings of Ultrasonics International (UI'05) and World Congress on Ultrasonics (WCU) 44 (22nd Dec. 2006), e5–e15. ISSN: 0041-624X. DOI: 10.1016/j.ultras.2006.07.017.

[Jen07] Jørgen Arendt Jensen. 'Medical Ultrasound Imaging'. In: *Progress in Biophysics and Molecular Biology*. Effects of Ultrasound and Infrasound Relevant to Human Health 93.1 (1st Jan. 2007), pp. 153–165. ISSN: 0079-6107. DOI: 10.1016/j.pbiomolbio.2006.07.025.

[Kar95] M. Karaman, Pai-Chi Li and M. O'Donnell. 'Synthetic Aperture Imaging for Small Scale Systems'. In: *IEEE Transactions on Ultrasonics, Ferroelectrics, and Frequency Control* 42.3 (May 1995), pp. 429–442. ISSN: 0885-3010. DOI: 10.1109/58.384453.

[Kas20] Artem Kashubin and Peter Cawley. *Simulation of Full Matrix Capture Ultrasonic Array Data for Immersion Coupled Inspection (Unpublished Report)*. Imperial College London, 2020.

[Kas95] Robert E. Kass and Adrian E. Raftery. 'Bayes Factors'. In: *Journal of the American Statistical Association* 90.430 (1995), pp. 773–795. ISSN: 0162-1459. DOI: 10.2307/2291091. JSTOR: 2291091.

[Ker03] E. Kerbrat, C. Prada, D. Cassereau and M. Fink. 'Imaging in the Presence of Grain Noise Using the Decomposition of the Time Reversal Operator'. In: *The Journal of the Acoustical Society of America* 113.3 (28th Feb. 2003), pp. 1230–1240. ISSN: 0001-4966. DOI: 10.1121/1.1548156.

[Kra90] Joseph Krautkrämer and Herbert Krautkrämer. *Ultrasonic Testing of Materials*. 4th, 1990. Springer-Verlag Berlin Heidelberg, 1990. ISBN: 978-3-662-10682-2.

[Kru11] John K. Kruschke. *Doing Bayesian Data Analysis : A Tutorial with R and BUGS*. Amsterdam ; Academic Press, 2011. ISBN: 978-0-12-381485-2.

[Kup02] William A Kuperman, Jean-Paul Montagner and Arnaud Tourin. *Imaging of Complex Media with Acoustic and Seismic Waves*. Springer Science & Business Media, 2002.

[Kwa19] Chi-Hang Kwan, Guillaume Painchaud-April and Benoit Lepage. 'TFM Acoustic Influence Map'. In: ASNT Research Symposium 2019. 2019. DOI: 10.32548/RS.2019.012.

[Lan14] Shiwei Lan, Jeffrey Streets and Babak Shahbaba. 'Wormhole Hamiltonian Monte Carlo'. In: (3rd Mar. 2014). arXiv: 1306.0063 [stat].

[Lan86] K. J. Langenberg, M. Berger, Th. Kreutter, K. Mayer and V. Schmitz. 'Synthetic Aperture Focusing Technique Signal Processing'. In: *NDT International* 19.3 (1st June 1986), pp. 177–189. ISSN: 0308-9126. DOI: 10.1016/0308-9126(86)90107-0.

[Le 16] Léonard Le Jeune, Sébastien Robert, Eduardo Lopez Villaverde and Claire Prada. 'Plane Wave Imaging for Ultrasonic Non-Destructive Testing: Generalization to Multimodal Imaging'. In: *Ultrasonics* 64 (Jan. 2016), pp. 128–138. ISSN: 0041-624X. DOI: 10.1016/j.ultras.2015.08.008.

[Lea83] Malcolm R Leadbetter, Georg Lindgren and Holger Rootzén. *Extremes and Related Properties of Random Sequences and Processes*. Springer, 1983. ISBN: 0-387-90731-9.

[Li12] Minghui Li and Gordon Hayward. 'Ultrasound Nondestructive Evaluation (NDE) Imaging with Transducer Arrays and Adaptive Processing'. In: *Sensors* 12.1 (1 Jan. 2012), pp. 42–54. DOI: 10.3390/s120100042.

[Li13] Chuan Li, Damien Pain, Paul D. Wilcox and Bruce W. Drinkwater. 'Imaging Composite Material Using Ultrasonic Arrays'. In: *NDT & E International* 53 (Jan. 2013), pp. 8–17. ISSN: 0963-8695. DOI: 10.1016/j.ndteint.2012.07.006.

[Lon12] R Long, J Russell and P Cawley. 'Ultrasonic Phased Array Inspection Using Full Matrix Capture'. In: *Insight - Non-Destructive Testing and Condition Monitoring* 54.7 (1st July 2012), pp. 380–385. DOI: 10.1784/insi.2012.54.7.380.

[Lop05] Ana L. Lopez-Sanchez, Hak-Joon Kim, Lester W. Schmerr and Alexander Sedov. 'Measurement Models and Scattering Models for Predicting the Ultrasonic Pulse-Echo Response From Side-Drilled Holes'. In: *Journal of Nondestructive Evaluation* 24.3 (1st Sept. 2005), pp. 83–96. ISSN: 0195-9298, 1573-4862. DOI: 10.1007/s10921-005-7658-4.

[Lop16] Eduardo Lopez Villaverde, Sébastien Robert and Claire Prada. 'Ultrasonic Imaging of Defects in Coarse-Grained Steels with the Decomposition of the Time Reversal Operator'. In: *The Journal of the Acoustical Society of America* 140.1 (1st July 2016), pp. 541–550. ISSN: 0001-4966. DOI: 10.1121/1.4958683.

[Lor93] Maarten Lorenz. 'Ultrasonic Imaging for the Characterization of Defects in Steel Components'. Delft University of Technology, 1993.

[Low70] Serge Lowenthal and Henri Arsenault. 'Image Formation for Coherent Diffuse Objects: Statistical Properties'. In: *JOSA* 60.11 (1st Nov. 1970), pp. 1478–1483. DOI: 10.1364/JOSA.60.001478.

[Mar06] R.A. Maronna, D.R. Martin and V.J. Yohai. *Robust Statistics: Theory and Methods*. Wiley Series in Probability and Statistics. Wiley, 2006. ISBN: 978-0-470-01092-1.

[Mar07] Jean-Michel Marin and Christian Robert. *Bayesian Core: A Practical Approach to Computational Bayesian Statistics*. Springer Science & Business Media, 6th Feb. 2007. 265 pp. ISBN: 978-0-387-38979-0. Google Books: Lx74oEz5pmsC.

[Mar96] F. J. Margetan, Isaac Yalda and R. B. Thompson. 'Predicting Gated-Peak Grain Noise Distributions for Ultrasonic Inspections of Metals'. In: *Review of Progress in Quantitative Nondestructive Evaluation: Volume 15A*. Ed. by Donald O. Thompson and Dale E. Chimenti. Boston, MA: Springer US, 1996, pp. 1509–1516. ISBN: 978-1-4613-0383-1. DOI: 10.1007/978-1-4613-0383-1_197.

[Mas03] Jean-Claude Massé and Jean-François Plante. 'A Monte Carlo Study of the Accuracy and Robustness of Ten Bivariate Location Estimators'. In: *Computational Statistics & Data Analysis* 42.1 (28th Feb. 2003), pp. 1–26. ISSN: 0167-9473. DOI: 10.1016/S0167-9473(02)00103-2.

[Mer20] L. Merabet, S. Robert and C. Prada. 'The Multi-Mode Plane Wave Imaging in the Fourier Domain: Theory and Applications to Fast Ultrasound Imaging of Cracks'. In: *NDT & E International* 110 (1st Mar. 2020), p. 102171. ISSN: 0963-8695. DOI: 10.1016/j.ndteint.2019.102171.

[Min06] Jean-Gabriel Minonzio. 'Décomposition de l'Opérateur de Retournement Temporel appliquée à l'imagerie et à la caractérisation ultrasonore'. PhD thesis. Université Paris-Diderot - Paris VII, 11th Dec. 2006.

[Mon09] Gabriel Montaldo, Mickaël Tanter, Jérémy Bercoff, Nicolas Benech and Mathias Fink. 'Coherent Plane-Wave Compounding for Very High Frame Rate Ultrasonography and Transient Elastography'. In: *IEEE Transactions on Ultrasonics, Ferroelectrics, and Frequency Control* 56.3 (Mar. 2009), pp. 489–506. ISSN: 1525-8955. DOI: 10.1109/TUFFC.2009.1067.

[Mor14] L. Moreau, A. J. Hunter, A. Velichko and P. D. Wilcox. '3-D Reconstruction of Sub-Wavelength Scatterers from the Measurement of Scattered Fields in Elastic Waveguides'. In: *IEEE Transactions on Ultrasonics, Ferroelectrics, and Frequency Control* 61.11 (Nov. 2014), pp. 1864–1879. DOI: 10.1109/TUFFC.2014.006619.

[Mor68] Philip Morse and Uno Ingard. *Theoretical Acoustics*. Princeton University Press, 1st Jan. 1968. ISBN: 978-0-691-02401-1.

[Mow71] C. C. Mow and Y. H. Pao. *The Diffraction of Elastic Waves and Dynamic Stress Concentrations*. 1971.

[Noc06] Jorge Nocedal and Stephen J. Wright. *Numerical Optimization*. 2nd ed. Springer Series in Operations Research and Financial Engineering. New York: Springer-Verlag, 2006. ISBN: 978-0-387-30303-1.

[Ogi93] J. A. Ogilvy. 'Model for Predicting Ultrasonic Pulse-Echo Probability of Detection'. In: *NDT & E International* 26.1 (1st Feb. 1993), pp. 19–29. ISSN: 0963-8695. DOI: 10.1016/0963-8695(93)90160-V.

[OHa04] Anthony O'Hagan and Jon Forster. *Kendall's Advanced Theory of Statistics. Vol.2B: Bayesian Inference*. 2004.

[Oha19] Yoshikazu Ohara, Jack Potter, Hiromichi Nakajima, Toshihiro Tsuji and Tsuyoshi Mihara. 'Multi-Mode Nonlinear Ultrasonic Phased Array for Imaging Closed Cracks'. In: *Japanese Journal of Applied Physics* 58 (SG June 2019), SGGB06. ISSN: 1347-4065. DOI: 10.7567/1347-4065/ab0adc.

[Oli96] Bryan D. Olin and William Q. Meeker. 'Applications of Statistical Methods to Nondestructive Evaluation'. In: *Technometrics* 38.2 (1996), pp. 95–112. ISSN: 0040-1706. DOI: 10.2307/1270399. JSTOR: 1270399.

[Oly17] Olympus. *Introduction to Phased Array Ultrasonic Technology Applications: Olympus Guidelines*. Ed. by Olympus. 4th ed. Advanced Practical NDT Series. Waltham, Mass, 2017. 356 pp. ISBN: 978-0-9735933-0-3.

[Plu03] Martyn Plummer et al. 'JAGS: A Program for Analysis of Bayesian Graphical Models Using Gibbs Sampling'. In: *Proceedings of the 3rd International Workshop on Distributed Statistical Computing*. Vol. 124. Vienna, Austria, 2003.

[Por08] Niels Portzgen, Dries Gisolf and Dirk J. Verschuur. 'Wave Equation-Based Imaging of Mode Converted Waves in Ultrasonic NDI, with Suppressed Leakage from Nonmode Converted Waves'. In: *IEEE Transactions on Ultrasonics, Ferroelectrics, and Frequency Control* 55.8 (Aug. 2008), pp. 1768–1780. ISSN: 0885-3010. DOI: 10.1109/TUFFC.2008.861.

[Pot14] J. N. Potter, A. J. Croxford and P. D. Wilcox. 'Nonlinear Ultrasonic Phased Array Imaging'. In: *Physical Review Letters* 113.14 (3rd Oct. 2014), p. 144301. DOI: 10.1103/PhysRevLett.113.144301.

[Pra94] Claire Prada and Mathias Fink. 'Eigenmodes of the Time Reversal Operator: A Solution to Selective Focusing in Multiple-Target Media'. In: *Wave Motion* 20.2 (1st Sept. 1994), pp. 151–163. ISSN: 0165-2125. DOI: 10.1016/0165-2125(94)90039-6.

[Rob07] Christian Robert. *The Bayesian Choice*. Springer Science & Business Media, 27th Aug. 2007. 620 pp. ISBN: 978-0-387-71598-8. Google Books: 6oQ4s8Pq9pYC.

[Rob10] Christian P. Robert. 'Bayesian Computational Methods'. In: (13th Feb. 2010). arXiv: 1002.2702 [stat].

[Rob11] Christian Robert and George Casella. 'A Short History of Markov Chain Monte Carlo: Subjective Recollections from Incomplete Data'. In: *Statistical Science* 26.1 (Feb. 2011), pp. 102–115. ISSN: 0883-4237. DOI: 10.1214/10-STS351. arXiv: 0808.2902.

[Rou14] Gilles Rougeron, Jason Lambert, Ekaterina Iakovleva, Lionel Lacassagne and Nicolas Dominguez. 'Implementation of a GPU Accelerated Total Focusing Reconstruction Method within CIVA Software'. In: 2014, pp. 1983–1990. DOI: 10.1063/1.4865067.

[Sal16] John Salvatier, Thomas V. Wiecki and Christopher Fonnesbeck. 'Probabilistic Programming in Python Using PyMC3'. In: *PeerJ Computer Science* 2 (6th Apr. 2016), e55. ISSN: 2376-5992. DOI: 10.7717/peerj-cs.55.

[Sch07] Lester W. Schmerr and Sung-Jin Song. *Ultrasonic Nondestructive Evaluation Systems*. Boston, MA: Springer US, 2007. ISBN: 978-0-387-49061-8.

[Sch15] Lester W. Schmerr. *Fundamentals of Ultrasonic Phased Arrays*. Vol. 215. Solid Mechanics and Its Applications. Cham: Springer International Publishing, 2015. ISBN: 978-3-319-07271-5.

[Sch16] Lester W. Schmerr. *Fundamentals of Ultrasonic Nondestructive Evaluation: A Modeling Approach*. 2nd ed. 2016 edition. New York, NY: Springer, 18th May 2016. 778 pp. ISBN: 978-3-319-30461-8.

[Sco15] David W Scott. *Multivariate Density Estimation: Theory, Practice, and Visualization*. John Wiley & Sons, 2015.

[Sid63] M. M. Siddiqui. 'Optimum Estimators of the Parameters of Negative Exponential Distributions from One or Two Order Statistics'. In: *The Annals of Mathematical Statistics* 34.1 (Mar. 1963), pp. 117–121. ISSN: 0003-4851. DOI: 10.1214/aoms/1177704247.

[Sid64] M. M. Siddiqui. *Statistical Inference for Rayleigh Distributions*. National Bureau of Standards, 1964.

[Sim08] F Simonetti and L Huang. 'From Beamforming to Diffraction Tomography'. In: *Journal of Applied Physics* 103.10 (2008), p. 103110.

[Skj11] Martin H. Skjelvareid, Tomas Olofsson, Yngve Birkelund and Yngvar Larsen. 'Synthetic Aperture Focusing of Ultrasonic Data from Multilayered Media Using an Omega-K Algorithm'. In: *IEEE Transactions on Ultrasonics, Ferroelectrics, and Frequency Control* 58.5 (May 2011), pp. 1037–1048. ISSN: 1525-8955. DOI: 10.1109/TUFFC.2011.1904.

[Sma90] Christopher G. Small. 'A Survey of Multidimensional Medians'. In: *International Statistical Review / Revue Internationale de Statistique* 58.3 (1990), pp. 263–277. ISSN: 0306-7734. DOI: 10.2307/1403809. JSTOR: 1403809.

[Smi83] S. W. Smith, R. F. Wagner, J. M. Sandrik and H. Lopez. 'Low Contrast Detectability and Contrast/Detail Analysis in Medical Ultrasound'. In: *IEEE Transactions on Sonics and Ultrasonics* 30.3 (May 1983), pp. 164–173. DOI: 10.1109/T-SU.1983.31405.

[Smi84] S. W. Smith and R. F. Wagner. 'Ultrasond Speckle Size and Lesion Signal to Noise Ratio: Verification of Theory'. In: *Ultrasonic Imaging* 6.2 (1st Apr. 1984), pp. 174–180. ISSN: 0161-7346. DOI: 10.1016/0161-7346(84)90024-5.

[Sol01] Igor Yu. Solodov and Boris A. Korshak. 'Instability, Chaos, and "Memory" in Acoustic-Wave–Crack Interaction'. In: *Physical Review Letters* 88.1 (19th Dec. 2001), p. 014303. DOI: 10.1103/PhysRevLett.88.014303.

[Som68] J. C. Somer. 'Electronic Sector Scanning for Ultrasonic Diagnosis'. In: *Ultrasonics* 6.3 (1st July 1968), pp. 153–159. ISSN: 0041-624X. DOI: 10.1016/0041-624X(68)90277-1.

[Ste07] Tadeusz Stepinski. 'An Implementation of Synthetic Aperture Focusing Technique in Frequency Domain'. In: *IEEE Transactions on Ultrasonics, Ferroelectrics, and Frequency Control* 54.7 (July 2007), pp. 1399–1408. ISSN: 1525-8955. DOI: 10.1109/TUFFC.2007.400.

[Str16] Theodosia Stratoudaki, Matt Clark and Paul D. Wilcox. 'Laser Induced Ultrasonic Phased Array Using Full Matrix Capture Data Acquisition and Total Focusing Method'. In: *Optics Express* 24.19 (19th Sept. 2016), pp. 21921–21938. ISSN: 1094-4087. DOI: 10.1364/OE.24.021921.

[Sut12] Mark Sutcliffe, Miles Weston, Peter Charlton, Ben Dutton and K Donne. 'Virtual Source Aperture Imaging for Non-Destructive Testing'. In: *Insight-Non-Destructive Testing and Condition Monitoring* 54.7 (2012), pp. 371–379.

[Sy18a] K. Sy, P. Bredif, E. Iakovleva, O. Roy and D. Lesselier. 'Development of Methods for the Analysis of Multi-Mode TFM Images'. In: *Journal of Physics: Conference Series* 1017 (May 2018), p. 012005. ISSN: 1742-6596. DOI: 10.1088/1742-6596/1017/1/012005.

[Sy18b] Kombossé Sy. 'Étude et Développement de Méthodes de Caractérisation de Défauts Basées Sur Les Reconstructions Ultrasonores TFM'. thesis. Paris Saclay, 15th Feb. 2018.

[Sy18c] Kombossé Sy, Philippe Brédif, Ekaterina Iakovleva, Olivier Roy and Dominique Lesselier. 'Development of the Specular Echoes Estimator to Predict Relevant Modes for Total Focusing Method Imaging'. In: *NDT & E International* 99 (1st Oct. 2018), pp. 134–140. ISSN: 0963-8695. DOI: 10.1016/j.ndteint.2018.07.005.

[Syn07] J. F. Synnevag, A. Austeng and S. Holm. 'Adaptive Beamforming Applied to Medical Ultrasound Imaging'. In: *IEEE Transactions on Ultrasonics, Ferroelectrics, and Frequency Control* 54.8 (Aug. 2007), pp. 1606–1613. ISSN: 0885-3010. DOI: 10.1109/TUFFC.2007.431.

[Syn09] Johan-Fredrik Synnevåg. 'Adaptive Beamforming for Medical Ultrasound Imaging'. University of Oslo, 2009.

[Tan15] K. M. M. Tant, A. J. Mulholland and A. Gachagan. 'A Model-Based Approach to Crack Sizing with Ultrasonic Arrays'. In: *IEEE Transactions on Ultrasonics, Ferroelectrics, and Frequency Control* 62.5 (May 2015), pp. 915–926. ISSN: 0885-3010. DOI: 10.1109/TUFFC.2014.006809.

[Tho06] Lonny L. Thompson. 'A Review of Finite-Element Methods for Time-Harmonic Acoustics'. In: *The Journal of the Acoustical Society of America* 119.3 (28th Feb. 2006), pp. 1315–1330. ISSN: 0001-4966. DOI: 10.1121/1.2164987.

[Tho83] R. B. Thompson and T. A. Gray. 'A Model Relating Ultrasonic Scattering Measurements through Liquid–Solid Interfaces to Unbounded Medium Scattering Amplitudes'. In: *The Journal of the Acoustical Society of America* 74.4 (1st Oct. 1983), pp. 1279–1290. ISSN: 0001-4966. DOI: 10.1121/1.390045.

[Tia19] Zhenhua Tian, Lingyu Yu, Xiaoyi Sun and Bin Lin. 'Damage Localization with Fiber Bragg Grating Lamb Wave Sensing through Adaptive Phased Array Imaging'. In: *Structural Health Monitoring* 18.1 (1st Jan. 2019), pp. 334–344. ISSN: 1475-9217. DOI: 10.1177/1475921718755572.

[Tuk60] John W. Tukey. 'A Survey of Sampling from Contaminated Distributions'. In: *Contributions to Probability and Statistics: Essays in Honor of Harold Hotelling*. Ed. by I. Olkin, S. G. Ghurye, W. Hoeffding, W. G. Madow and H. B. Mann. Stanford, CA, USA: Stanford University Press, 1960, pp. 448–485.

[Tur90] Ken Turkowski. 'Filters for Common Resampling Tasks'. In: *Graphics Gems*. Academic Press Professional, Inc., 1990, pp. 147–165.

[Vel09] A. Velichko and P. D. Wilcox. 'Reversible Back-Propagation Imaging Algorithm for Postprocessing of Ultrasonic Array Data'. In: *IEEE Transactions on Ultrasonics, Ferroelectrics, and Frequency Control* 56.11 (Nov. 2009), pp. 2492–2503. ISSN: 0885-3010. DOI: 10.1109/TUFFC.2009.1336.

[Vel10a] Alexander Velichko and Paul D. Wilcox. 'A Generalized Approach for Efficient Finite Element Modeling of Elastodynamic Scattering in Two and Three Dimensions'. In: *The Journal of the Acoustical Society of America* 128.3 (1st Sept. 2010), pp. 1004–1014. ISSN: 0001-4966. DOI: 10.1121/1.3467775.

[Vel10b] Alexander Velichko and Paul D. Wilcox. 'An Analytical Comparison of Ultrasonic Array Imaging Algorithms'. In: *The Journal of the Acoustical Society of America* 127.4 (Apr. 2010), pp. 2377–2384. ISSN: 1520-8524. DOI: 10.1121/1.3308470. pmid: 20370020.

[Vel17] A. Velichko, L. Bai and B. W. Drinkwater. 'Ultrasonic Defect Characterization Using Parametric-Manifold Mapping'. In: *Proc. R. Soc. A* 473.2202 (1st June 2017), p. 20170056. ISSN: 1364-5021, 1471-2946. DOI: 10.1098/rspa.2017.0056.

[Von36] Richard Von Mises. 'La Distribution de La plus Grande de n Valeurs'. In: *Rev. math. Union interbalcanique* 1 (1936), pp. 141–160.

[Wag83] R. F. Wagner, S. W. Smith, J. M. Sandrik and H. Lopez. 'Statistics of Speckle in Ultrasound B-Scans'. In: *IEEE Transactions on Sonics and Ultrasonics* 30.3 (May 1983), pp. 156–163. ISSN: 0018-9537. DOI: 10.1109/T-SU.1983.31404.

[Wag87] Robert F. Wagner, Michael F. Insana and David G. Brown. 'Statistical Properties of Radio-Frequency and Envelope-Detected Signals with Applications to Medical Ultrasound'. In: *JOSA A* 4.5 (1st May 1987), pp. 910–922. ISSN: 1520-8532. DOI: 10.1364/JOSAA.4.000910.

[Wei] Eric W. Weisstein. *"Multichoose". From MathWorld—A Wolfram Web Resource.* URL: Multichoose.

[Wei09] E. Weiszfeld and Frank Plastria. 'On the Point for Which the Sum of the Distances to n given Points Is Minimum'. In: *Annals of Operations Research* 167.1 (1st Mar. 2009), pp. 7–41. ISSN: 1572-9338. DOI: 10.1007/s10479-008-0352-z.

[Wil11] P. D. Wilcox. 'Array Imaging of Noisy Materials'. In: *AIP Conference Proceedings. Review of Progress in Quantitative Nondestructive Evaluation.* Vol. 1335. 23rd June 2011, pp. 890–897. DOI: 10.1063/1.3591941.

[Wil13] Paul D. Wilcox. 'Ultrasonic Arrays in NDE: Beyond the B-Scan'. In: *AIP Conference Proceedings. Review of Progress in Quantitative Nondestructive Evaluation.* Vol. 1511. 25th Jan. 2013, pp. 33–50. DOI: 10.1063/1.4789029.

[Yal96] Isaac Yalda, Frank J. Margetan and R. Bruce Thompson. 'Predicting Ultrasonic Grain Noise in Polycrystals: A Monte Carlo Model'. In: *The Journal of the Acoustical Society of America* 99.6 (1st June 1996), pp. 3445–3455. ISSN: 0001-4966. DOI: 10.1121/1.414991.

[Zha08] Jie Zhang, B.W. Drinkwater and P.D. Wilcox. 'Defect Characterization Using an Ultrasonic Array to Measure the Scattering Coefficient Matrix'. In: *IEEE Transactions on Ultrasonics, Ferroelectrics, and Frequency Control* 55.10 (Oct. 2008), pp. 2254–2265. ISSN: 0885-3010. DOI: 10.1109/TUFFC.924.

[Zha10a] Jie Zhang, Bruce W. Drinkwater and Paul D. Wilcox. 'The Use of Ultrasonic Arrays to Characterize Crack-Like Defects'. In: *Journal of Nondestructive Evaluation* 29.4 (1st Dec. 2010), pp. 222–232. ISSN: 1573-4862. DOI: 10.1007/s10921-010-0080-6.

[Zha10b] Jie Zhang, Bruce W. Drinkwater, Paul D. Wilcox and Alan J. Hunter. 'Defect Detection Using Ultrasonic Arrays: The Multi-Mode Total Focusing Method'. In: *NDT & E International* 43.2 (Mar. 2010), pp. 123–133. ISSN: 0963-8695. DOI: 10.1016/j.ndteint.2009.10.001.

[Zha12] Yimin D. Zhang, Xizhong Shen, Ramazan Demirli and Moeness G. Amin. 'Ultrasonic Flaw Imaging via Multipath Exploitation'. In: *Advances in Acoustics and Vibration* 2012 (1st Jan. 2012). ISSN: 1687-6261, 1687-627X.

[Zha17] Jie Zhang, Tom Barber, Andrew Nixon and Paul Wilcox. 'Investigation into Distinguishing between Small Volumetric and Crack-like Defects Using Multi-View Total Focusing Method Images'. In: *AIP Conference Proceedings* 1806.1 (16th Feb. 2017), p. 040003. ISSN: 0094-243X. DOI: 10.1063/1.4974590.